The Development of an In-Vivo Dosimeter for the Application of Radiotherapy

Rajiv Bose

A thesis submitted for the degree of

Doctor of Philosophy

Centre for Sensors and Instrumentation

School of Engineering and Design

Brunel University, Uxbridge

Tuesday 4th December, 2012

Abstract

The expectation for continual improvements in the treatment of cancer has brought quality assurance in radiotherapy under scrutiny in recent years. After a cancer diagnosis a custom treatment plan is devised to meet the particular needs of the patient's condition based on their prognosis. A cancer treatment plan will typically comprise of several cancer treatment technologies combining to form a comprehensive programme to fight the malignant growth. Inherent in each cancer treatment technology is a percentage error in treatment accuracy. Quality assurance is the medical practice to minimise the percentage error in treatment accuracy. Radiotherapy is one of the several cancer treatment technologies a patient might receive as part of their treatment plan, and in-vivo dosimetry is a quality assurance technology specifically designed to minimise the percentage error in the treatment accuracy of radiotherapy.

This thesis outlines the work completed in the design of a next generation dosimeter for in-vivo dosimetry. The proposed dosimeter is intended to modernise the process of measuring the absorbed dose of ionising radiation received by the target volume during a radiotherapy session. To accomplish this goal the new dosimeter will amalgamate specialist technologies from the field of particle physics and reapply them to the field of medical physics. This thesis describes the design of a new implantable in-vivo dosimeter, a dosimeter comprising of several individual stages of electronics working together to modernise quality assurance in radiotherapy. Presented within this thesis are the results demonstrating the performance of two critical stages for this new dosimeter, including: the floating gate metal oxide field effective transistor, a radiation sensitive electronic component measuring an absorbed dose of radiation; and the micro antenna, a highly specialist wireless communications device working to transmit a high frequency radio signal.

This was a collaborative project between Rutherford Appleton Laboratory and Brunel University. The presented work in this thesis was completed between March 2007 and January 2011.

Declaration

I hereby declare that no part of this thesis has been previously submitted to this or any other university as part of the requirement for a higher degree. The work described herein was conducted solely by the undersigned except for those colleagues and other workers acknowledged in the text.

Rajiv Bose
Tuesday 4th December, 2012

Dedication

For Mum and Dad

Acknowledgements

Thanks go to ...

Prof. Akram Khan, my supervisor, for his continued support throughout my research. Akram's enthusiasm for science and vision of the bigger picture always lifted me at times when I felt lost.

Dr. David Smith, this thesis would not have be possible without his meticulous, patient, and supportive nature.

All the staff at Brunel University, an institution that has been my home for the last 8 years. In particular: Dr. Ian Dear, Dr. Peter Turner, Dr. Iran Adil-Smith, and Dr. Matthew Barrett.

All the staff at the Rutherford Appleton Laboratory. In particular, Dr. Giulio Villani, Dr. John Matheson, and Dr. Rob Edgecock, for their technical assistance in and out of the lab, and for their general support and friendship that made my 13 months at RAL so enjoyable.

I would like to gratefully acknowledge the financial support received from the Science and Technology Facilities Council during my research studentship.

Family and friends who have been there for me every step of the way. In particular I would like to acknowledge the support of Tom and Ellen Nabarro, Gary Thornton, Adriana Mattos, Emily McClave, and Johnny Fill.

Contents

List of Figures

List of Tables

Chapter 1

Introduction

1.1 In-Vivo Dosimetry

Dosimetry refers to a device used to calculate the absorbed dose of ionising radiation in matter or tissue resulting from its direct or indirect exposure to a radiation source. The measurement of absorbed dose of ionising radiation has many applications from space science, to health and safety, to particle physics, to medicine. *In-vivo* is a latin phrase meaning, of processes taking place in a living organism. Despite the literal interpretation of the term seldom does in-vivo dosimetry (IVD) refer to the measurement of the absorbed dose of ionising radiation from within a living thing. Instead the nomenclature for the term comes from its medical application within radiotherapy and is commonly used to describe the measurement of absorbed dose of ionising radiation taken while a patient is receiving treatment.

If dosimetry is the measurement of the absorbed dose of ionising radiation then the practical value of dosimetry to the field of radiotherapy has long been recognised. The merits of a dosimeter in the calibration of a radiation source has led to the development of a plethora of different types of commercially available dosimeters, each with their own distinct attributes. However, dosimeters developed to provide measurement of the absorbed dose of ionising radiation while the patient is undergoing treatment has not been met with the same ubiquitous support as dosimeters for linac (linear accelerator)

calibration.

Historically the arguments against the routine use of IVD have to do with the cost compared to perceived improvements to the patient's quality of care. Dosimetry alone is not a technology capable of directly changing the probability of a patient overcoming cancer, it can only provide assurances towards the accuracy of the treatment. The number of competing dosimetry technologies available on the market today only add to the confusion facing a physician's incentive in favouring routine IVD.

Although the operational requirements of a dosimeter are unique to their field of application the implementing technology behind each dosimeter can sometimes be transferable. The substantial advance of scientific research in the field of particle physics over the last couple of decades has culminated in the launch of the LHC experiment at CERN, and it is in addressing the challenges of radiation measurement faced by the engineers and physicists of CERN that has, in a small way, contributed to the science of IVD in medicine.

1.2 Research Goals

It is the objective of this project to develop an implantable submillimetre in-vivo dosimeter based on floating-gate transistor technology. The attributes that make the floating-gate transistor suitable in the design of an implantable in-vivo dosimeter are presented in Section 3.4.4.

Such a complex technology can only be achieved by breaking down the problem into sections and implementing solutions to each section in stages. Only once each of the individual sections to the new dosimeter are designed and proven to work can all stages be brought together to realise the intended solution.

The work carried out for this thesis is comprised of two separate studies. These two studies make two of the four sections deemed necessary before a completely new and novel dosimeter for IVD can be realised. The aim of the first study was to assess the potential of the floating-gate transistor as an electronic component capable of measuring the absorbed dose of ionising

radiation it has been exposed to. Other alternative transistor types can and have been used to measure an absorbed dose of radiation however there are particular attributes to the floating-gate transistor that enhance its suitability as a radiation measuring component. The aim of the first study was to investigate these potentially advantageous characteristics of the floating-gate transistor.

The aim of the second study was to address the necessary wireless communication requirement of an implantable in-vivo dosimeter by evaluating the performance difference between three alternative micro antenna designs. The operational requirements of a micro antenna for an implantable medical device are unique by comparison to the extensive list of designed antennas for alternative applications. It was the lack of completed research available on the performance of a micro antenna for an implantable medical device that led the second study to assess the performance of three alternative designs to determine which antenna design would offer the greatest efficiency when used to communicate the dosimeter's measured absorbed dose of ionising radiation.

The work carried out for this thesis was funded by a Co-operative Award in Science and Engineering (CASE) studentship from the Science and Technology Facilities Council (STFC) in collaboration with Rutherford Appleton Laboratory (RAL) of the Harwell Science Park, Didcot, England.

1.3 Thesis Organisation

This is the first thesis on the design and performance of an implantable dosimeter for radiotherapy from the Centre for Sensors and Instrumentation (CSI) at Brunel University. The group has traditionally been involved in the design of silicon based detectors for space science (Chandrayaan-1) and particle physics (CMS and MICE) while supporting the computing infrastructure to the LHC experiment through the GridPP framework. However, with the increasing affordability of the cyclotron accelerator technology, it has been recognised within the group that it is only a matter of time before the development of particle based radiation is used as commonly in the

treatment of cancer as the more widespread γ based radiation treatments seen today. It is with this thinking in mind that there is value to be had by extending the group's working knowledge of dosimeter design for medical application. The higher energies used in particle based radiation treatment will only further galvanise the call for routine IVD to improve quality assurance (QA) in radiotherapy. With the use of higher energy radiation beams the dangers of mistreatment are potentially more harmful if they occur. As such with the introduction of improved QA, including routine use of IVD, will mean the attractive properties of a particle based radiation beam can be exploited whist minimising the risk. A particle based radiation beam is superior to the conventional radiation beam γ by the nature of how energy is deposited within the patient. This idea is explored further in Section 6.2.

The thesis is organised into seven chapters including:

- Chapter 1 - briefly outlining subject, research goals, and structure of this thesis, as well as listing all accomplished peer reviewed publications and conference presentations.

- Chapter 2 - a background chapter summarising all relevant aspects of the field of radiotherapy, from cancer incidence rates in the UK to the effects of ionising radiation on human cells, building an argument justifying the need for routine IVD as a QA technology.

- Chapter 3 - a theory chapter exploring why the floating gate metal oxide field effective transistor (FGMOSFET) is potentially a suitable electronic component to measure the absorbed dose of ionising radiation. Starting with the fundamental structure of doped silicon the presented material works all the way through to the expected response of the FGMOSFET when exposed to a radiation source.

- Chapter 4 - a theory chapter included as a brief review of electromagnetic theory as defined by Maxwell's equations before delineating the relevant theoretical and practical considerations of micro antenna design.

- Chapter 5 - a presentation of the results from an experiment where the precise evaluation of the FGMOSFET as an electronic component capable of measuring the absorbed dose of ionising radiation was completed. The radiation source used for this experiment is comparable to a source used during radiotherapy.

- Chapter 6 - a results chapter presenting the findings of an experiment that determined which of three custom designed micro antennas would best perform in the field of IVD as part of an electronic circuit to be used as a medical implant. The micro antenna was designed to communicate its measured absorbed dose of radiation via a strict wireless specification.

- Chapter 7 - a brief conclusion that evaluates the accomplishments highlighted in this thesis and also offers a summary of the shortcomings of the completed work. This chapter closes by identifying the next steps that could follow from this thesis offering a platform from which future work could begin in the pursuit of the next generation of dosimeters for radiotherapy.

1.4 Publications and Presentations

The data presented in both results chapters included within this thesis were presented at the below list of either international conferences and peer reviewed journals:

Peer Reviewed Publications

- R. Edgecock, J. Matheson, M. Weber, Giulio E. Villani, R. Bose, A. Khan, D. R. Smith, I. Adil-Smith, and A. Gabrielli.
  Evaluation of commercial programmable floating gate devices as radiation dosimeters.
  Journal of Instrumentation, 4(2):1-10, February 2009.
  http://iopscience.iop.org/1748-0221/4/02/P02002

- Giulio E. Villani, R. Bose, and A. Gabrielli.
  Evaluation of on-chip micro antennas for in vivo dosimetry application.
  Radiation Measurements, 46(12):1963-1966, 2011.
  http://www.sciencedirect.com/science/article/pii/S1350448711002757

Peer Reviewed Presentations

- N54-7: Evaluation of on-chip Micro Antennas for In-Vivo Dosimetry Applications
  IEEE Nuclear Science Symposium and Medical Imaging Conference
  30th October to 6th November, 2010
  Knoxville, Tennessee
  http://www.nss-mic.org/2010/

- Evaluation of On Chip Micro Antennas for In-Vivo Dosimetry Applications
  16th Solid State Dosimetry Conference
  19th September to 24th September, 2010
  Sydney, Australia
  http://www.uow.edu.au/conferences/SSD16/

- Evaluation of a Commercial Programmable Floating-Gate MOSFET as a Radiation Dosimeter for In-Vivo Dosimetry
  2nd Annual Student Research Conference
  22nd June to 24th June, 2009
  London, United Kingdom
  http://www.brunel.ac.uk/sed/annual-conferences/1st-annual-student-research-conference-2009

Chapter 2

Background

2.1 Introduction

This is a background chapter setting the context for the thesis by building an argument justifying the need for routine IVD as a QA technology. In the medical context the use of dosimetry forms part of the QA practices used to minimise errors within radiotherapy.

The chapter begins with a section presenting the latest statistics on the prevalence of cancer in the UK. Following this brief review will be a discussion of the biology of cancer and how it develops from a cellular level. That section leads into an overview of radiotherapy as a treatment, the types of radiotherapy treatment available, and how a typical treatment is conducted. The following section reviews safety procedures in radiotherapy leading into a discussion on the need for improved QA. This is an important discussion as it explains how and why the demand for IVD in radiotherapy came about. Section 2.6 is a more lengthy discussion about how ionising radiation kills cells, the mechanism by which ionising radiation is used to treat cancer. The discussion approaches the subject by looking at the physical, chemical, and biological effects of ionising radiation on cells. The remaining three sections describe the proposed dosimeter, its expected performance, and give an idea of how it might operate.

2.2 UK Cancer Incidence Rates

Cancer is a heterogeneous classification of more than 200 different diseases characterised by the abnormal growth of a mutated cell. The symptoms of cancer vary due to the variety of its forms. Naturally, the symptoms of breast cancer differ to the symptoms of lung cancer but both are characterised by the abnormal growth of human cells.

Each year more than 300,000 new cancer diagnoses are made in the UK alone. With such high incidence rates, cancer is a disease that touches most peoples lives, directly or indirectly, and is therefore a subject of global interest. Organisations like the Cancer Research UK charity work hard to educate the public on the facts about cancer. Cancer Research UK perform a regular review of all published data from the Office for National Statistics regarding both incidence rates and mortality rates caused by cancer. The results are presented in an accessible form for the public.

The statistics of cancer in the UK are well documented. Unfortunately there is some latency between the latest statistics on cancer and the date when they are published. At the time of writing the following statistics are widely accepted as accurate based on data no later than 2008 [1]:

- 1 in 3 people will be diagnosed with cancer in their lifetime.
- 1 in 4 deaths in the UK are cancer related deaths.
- In woman, breast cancer has the highest incidence rate. Just over 1 in 3 newly diagnosed cancer cases in women are breast cancer.
- In men, prostate cancer has the highest incidence rate. Just under 1 in 4 newly diagnosed cancer cases in men are prostate cancer.
- The four most common types of cancer account for more than half of all cancer incidences in the UK. They include: breast, prostate, colorectal, and lung.

A popular illustration to capture the above statistics is shown in Figure 2.1. This graphic from Cancer Research UK provides a clear snapshot

of which cancers are most common by gender. This easy to read plot is a helpful tool used to educate the British public on the facts about cancer.

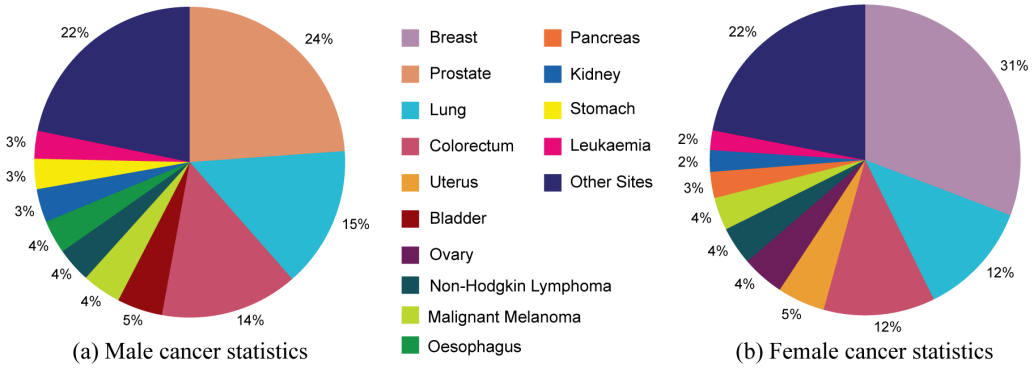

(a) Male cancer statistics

(b) Female cancer statistics

Figure 2.1: Distribution of most common cancers by gender [1].

The likelihood of developing cancer is dependent on many factors including age, lifestyle and genetic make-up. It has been estimated that almost half of all cancers in the UK could be avoided with attention to diet, exercise, bodyweight and sunlight exposure [2].

Tackling the growing concerns about the ever increasing unhealthy state of the British population is a high priority for every new government. The 2010 UK coalition government published Healthy Lives, Healthy People: Our strategy for public health in England [3]. This document outlines the importance of healthy living to help reduce the number of cancer incidence rates.

2.3 The Biology of Cancer

The growth of all healthy human cells in the body is conducted by a natural process called the cell cycle. This cycle is broken into two distinct phases, the interphase and the mitosis phase, as illustrated in Figure 2.2. During the interphase the cells gathers sufficient nutrients to complete the mitosis phase. Mitosis is the process whereby a mother cell splits and divides, making an exact copy of itself, forming two daughter cells. The daughter cells contain roughly half the cellular components of the mother cell.

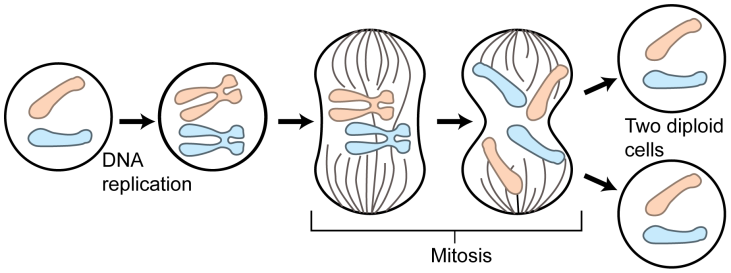

Figure 2.2: Illustration of the major stages to cell mitosis [4].

An important stage in the mitosis phase is the separation of the cell's chromosomes into two identical sets when the mother cell divides into two daughter cells and one set of chromosomes is for either daughter cell. Within a cell the deoxyribonucleic acid (DNA) is organised into long structures called chromosomes. A cell's DNA contains the instructions necessary for an organism to develop. The genetic information of the DNA is necessary for the cell to build and maintain itself. Communication between neighbouring cells is what regulates the rate at which cells undergo the cell cycle, this characterises the expected behaviour of healthy human cells. Cancer cells, however, are the result of an error in part of this communication process.

Cancer is defined as the unregulated growth of cells. A cancer cell is one that has stopped communicating with its neighbouring cells and is reproducing at an uncontrolled rate. A cancerous daughter cell is physiologically different to its mother cell in the composition of its DNA. All cancer cells are cells carrying DNA that has undergone a mutation.

Within nature the background rate is a low rate of randomly occurring DNA mutation. Mutation of a cell's DNA can have one of several effects. Only one of these effects is for the cell to become cancerous.

When a mutation occurs in a cell's DNA there is no guarantee the mutation will be persistent. That is, the mutation may not be persistent through the process of mitosis. When DNA becomes damaged proteins within the cell can sometimes correct the damage and repair the DNA. Failing that the DNA mutation may instigate the process of programmed cell death (PCD) and the cell will terminate. Should either of these two mechanisms occur then the cell, although carrying mutated DNA, will not cause cancer.

Should the DNA mutation be persistent through mitosis then there is one of two possible outcomes. Paradoxically, DNA mutation can serve as an advantage to an organism and this phenomenon is the first of two possible outcomes for cells carrying persistent mutated DNA. As Charles Darwin famously postulated, an adaptive evolution caused by natural selection is only possible with heritable genetic variation [5]. Persistent mutated DNA gives an organism genetic variation, and should that genetic variation provide the organism with an advantage in its natural habitat then that genetic variation facilitates adaptive evolution [6]. Unfortunately, persistent mutated DNA that supports adaptive evolution is a seldom occurrence, thus making evolution a slow process. The second possible outcome for cells carrying persistent mutated DNA occurs if the mutation is not repaired by cell proteins, or if the cell is not killed off by PCD, or if the persistent genetic variance is not a facility to adaptive evolution, and if the cell stops communicating with its neighbouring cells, then it will most likely be a cancerous cell. Over time, from this single cell, under the natural process of the cell cycle, a tumorous growth will develop. Only when symptoms resulting from this abnormality develop can a diagnosis be made.

Having described the advantage of naturally occurring DNA mutation there is one additional factor to be discussed, mutagens. A mutagen is an agent that causes a change in the frequency of DNA mutation in a cell. That is, separate to the cell's own physiology, a mutagen is an external agent that can raise the mutation rate in a cell's DNA above the naturally occurring background rate. It goes without saying that should the mutation rate of a cell's DNA increase then the probability of a mutation being a persistent cancer causing mutation also increases.

Just as DNA mutation at the natural background rate can have a positive implication to serve adaptive evolution, under certain circumstances, so too can the controlled introduction of a known mutagen have positive ramifications. This seemingly contradictory suggestion is explained in Section 2.6.1.

There are many different mutagens that can cause irreversible damage to DNA. Broadly speaking, mutagens are broken into two categories, physical agents and chemical agents. Should the mutagenic agent cause damage to

DNA that leads to cancer then that mutagen is referred to as a carcinogen. It should be noted that not all mutagens are carcinogens as not all mutations to DNA cause cancer. Carcinogens are mutagenic agents that damage DNA in such a way it leads to the uncontrolled divisions of malignant cells that ultimately causes the formation of tumours.

The original discovery of the effects of a mutagen was made by Hermann Muller. Muller published the results of his research in 1928 and showed that X-rays caused mutations in fruit flies [7]. In Muller's experiment the X-ray radiation was the mutagen being investigated, and only one parent fruit fly was subjected to X-ray exposure. The mutations observed were in the offspring from irradiated and non-irradiated fruit flies breeding together. The mutations observed manifested in both visible and lethal forms. Muller's work found the mutations caused by X-rays to a parent fruit fly were hereditary. This meant the mutagen must be causing mutation in the genetic material of the fruit fly.

2.4 Radiotherapy

External beam radiation therapy (EBRT) is a medical procedure routinely used in the treatment of cancer typically forming part of a patient's holistic treatment programme. An oncologist is a doctor who specialises in the treatment of cancer and is responsible for choosing the treatment programme a cancer patient will undergo. Radiotherapy is a procedure that is capable of treating cancer of any part of the body. It does so by aiming a high-energy beam of ionising radiation at a predetermined target volume where the cancerous growth is within that volume. Prior to radiotherapy treatment computed tomography (CT) [8] imaging is used to locate the patient's cancerous growth. Radiotherapy treats cancer by attacking cancer on a cellular level.

Once radiotherapy is prescribed as part of a patient's cancer treatment programme a timetable for treatment delivery is devised. Typically a patient's radiotherapy treatment is broken into several delivery sessions, or fractions as they are known. Between 10 and 15 fractions is common. Break-

ing up the treatment in this way has two major advantages. First, the dose per fraction is reduced which reduces the chance of harmful effects of the ionising radiation on the patient. Second, breaking up the treatment into several sessions allows healthy cells to recover from the ionising radiation.

After CT imaging two small dots are tattooed on the patient. The tattoo markers are permanent and are placed at the vertical and horizontal axis that traverse the centre point of the target volume. The tattooed markers are used to align the patient into the correct position for each treatment fraction. A treatment fraction will be booked into a 20 minute session and the treatment itself is brief. The majority of time during the session is spent ensuring the patient is positioned correctly. Correctly positioning the patient is critical to ensure the target volume is what the dose of ionising radiation is pointing at. The medical physicist is responsible for delivering the patient's treatment and will take great care to ensure the patient's setup is correct before proceeding with the treatment.

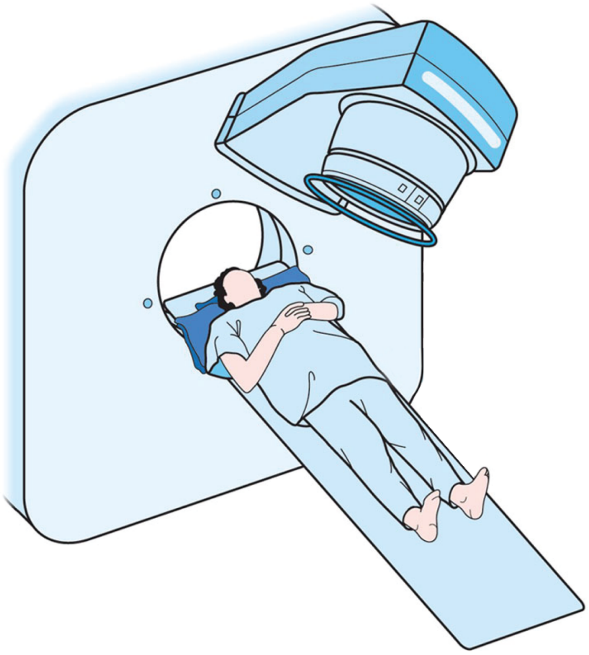

Figure 2.3: A patient receiving radiotherapy treatment from a linac with the gantry rotating around the patient for precision dose delivery [9].

Figure 2.3 shows a patient in position on a bed under the gantry of the linac [9]. The linac produces the beam of ionising radiation and the gantry shapes the high-energy beam before firing the beam at the patient's target volume. Typical of this type of delivery an X-ray source is used. The gantry is not fixed and, under computer controlled automation, the gantry will rotate around the patient whilst the treatment is underway. Thus, at the target volume, the sum of the absorbed dose of radiation energy from the beam is far greater than the absorbed dose of radiation energy by surrounding healthy tissue.

Alternative technologies in the field of radiotherapy deliver their treatment in different ways. Some of the competing systems of treatment include: conventional external beam radiation therapy (2DXRT), 3-dimensional conformal radiation therapy (3DCRT) [10], intensity modulated radiation therapy (IMRT) [11], and image-guided radiation therapy (IGRT) [12]. The source of ionising radiation used in the treatment of cancer is not limited to photon based (X-ray/γ-ray) linacs. Alternative radiation sources include; electrons [13], protons [14], and carbon ions [15]. However, in the UK the vast majority of oncology clinics only have access to photon based linacs. The only exception to this being the Clatterbridge Centre for Oncology, a cyclotron radiation source using a 62 MeV proton beam to treat choroidal melanoma [14]. Despite the variety of treatment systems and types of radiation beam available the one factor that is common between all form of radiotherapy is the need for QA.

With more than half of all cancer patients undergoing a course of radiotherapy at some point in their treatment programme [16, 17, 18, 19], and with more than 40 % of all cancer patients who survive cancer being treated with radiotherapy [20], radiotherapy has been an essential part in the treatment of cancer for many years. In the UK around 200 linear accelerators deliver 100,000 courses of radiotherapy in 1.5 million fractions annually [21], that is 4.25 million doses of radiation for cancer treatment each year.

2.5 Safety in Radiotherapy

As a treatment radiotherapy is a complex multi-stage procedure. Exposing the target volume to ionising radiation forms only part of the entire process. Before a single dose can be delivered a custom treatment plan must be devised based on the individual patient's diagnosis.

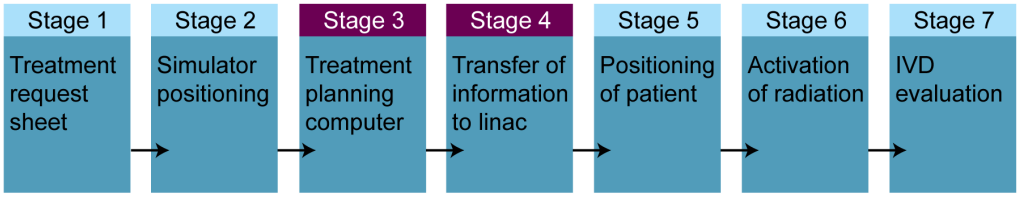

Figure 2.4: Stages of radiotherapy treatment in which high-profile errors repeatedly occurred [22, 23].

Figure 2.4 is a high-level generalisation of the stages to radiotherapy [22, 23]. Conceptualising treatment like this helps recognise the inherent errors within each stage of the treatment programme. The overall error of the treatment is the product of the error in each stage.

QA in radiotherapy is to include protocol within the treatment procedure that recognises the potential cause of errors within each stage. The need for QA in radiotherapy has long been established [24, 25, 26]. QA should safeguard the patient from the harmful effects of ionising radiation once an error has been recognised and instil confidence in the accuracy of treatment, that the intended dose of ionising radiation has successfully been delivered to the target volume.

Precision is a fundamental requirement in the delivery of ionising radiation as ionising radiation is harmful to human tissue. When a high degree of accuracy is adopted in radiotherapy patient duress and recovery time is minimised whilst maintaining quality of treatment. As such, when delivering a dose of ionising radiation, the consideration of the dose energy is as important as the consideration of dose location. The recommended accuracy requirements of ~ 3.5 % in the absorbed dose at the target volume and

< 5 mm in geometric accuracy from the position of the target volume have been stipulated [27].

Meeting the increasing demand for greater accuracy in radiotherapy has only been achievable with innovation within medical science. As the sophistication of radiotherapy technology has matured so too have the guidelines advising the performance requirements of radiotherapy. It is the scope of this project to design and build a technology to provide QA in only one of the stages in the radiotherapy procedure: the treatment delivery stage. The proposed QA technology is IVD and is capable of confirming the absorbed dose and geometric accuracy of the delivered dose.

Despite the long standing need for improved QA within radiotherapy [28, 29], including the recommended use of IVD to achieve that goal [30, 31], UK hospitals still maintain poor adoption rates for the routine use of IVD in the treatment of cancer [32], and there is little evidence to support that trend improving [33]. The Robert Appleyard survey found that over half (54 %) of the participating hospitals did not include routine IVD as part of their treatment, and none of those hospitals had plans to introduce routine IVD within the near future.

It was only after a number of high-profile accidents in radiotherapy [34, 35, 36] before a written mandate from Sir Liam Donaldson, the then acting Chief Medical Officer (CMO), instructed the integration of routine IVD in radiotherapy in UK hospitals [22]. Figure 2.4 highlights exactly where accidents can occur in radiotherapy [22]. The recommendation by the CMO for routine IVD as part of the radiotherapy treatment programme is to identify errors at these stages of treatment. Identifying errors early in treatment will safeguard patients against the harmful effects of ionising radiation and potentially save lives.

This proposal by the CMO is not without controversy and triggered a national debate regarding the motives of IVD in radiotherapy safety. Williams and McKenzie [37] justified the benefit to IVD with a cost related argument, suggesting the cost related to treating overdosed and under-dosed cancer patients is greater than the cost to implementing IVD (where IVD is used only in the initial fraction of a patient's treatment). However MacKay

and Williams [38] challenged the proposed financial argument suggesting the call for IVD is instead an effort to improve public confidence in radiotherapy, a move necessary only because of high-profile errors. In either case, neither paper discredited the merit of IVD to improve safety in radiotherapy, or the potential of IVD to save lives.

As state in the the Chief Medical Officer's 2006 Annual report the use of in-vivo dosimetry radiation checks should be made routine in accordance with a culture of incident reporting [22], small or serious, with computer reporting that is easy to understand by all staff.

If used correctly, IVD not only identifies when an unintended overdose or under-dose is being administered, but, if used through every fraction, IVD can give the medical physicist the opportunity to correct the potential error so as to prevent it from being a persistent error throughout the entire course of treatment.

2.6 Ionising Radiation: The Effect on Cells

The relationship between the energy of a photon (E) and the frequency (f) of its associated electromagnetic (EM) wave is given by the Planck-relation, described by Equation 2.1 [39], where h is Planck's constant. By describing radiation in terms of its energy it then becomes more straightforward to predict the expected behaviour of the radiation when it interacts with the cells of human tissue.

$$E = hf \tag{2.1}$$

In the practical context of a radiation source the distinction between the two classifications of energies is made by referring to how the radiation is produced. γ-ray radiation is, in the practical context of working with a radiation source, referring to a naturally occurring energy source where the EM waves are ejected from the nucleus of a radioisotope as the nucleus decays from an unstable state to a stable state. This process is measured as the radioisotope's half-life. A typical example of a γ-ray source is Cobalt-

60 (^{60}Co). A ^{60}Co source is a popular choice when replicating the medical conditions of radiotherapy for laboratory experiments. This avoids the costly overhead of an artificial radiation source at the trade off for accuracy. X-ray radiation is, in the practical context of working with a radiation source, referring to an artificially produced energy source where the EM waves are ejected from the collision events of high velocity electrons with a tungsten target.

Modern radiotherapy facilities in a hospital will use a powerful linac to produce and deliver a concentrated beam of photons at a patient's target volume. The energy of the photons can be of the X-ray or γ-ray range depending on the type and location of the cancer being treated. The shape and intensity of the beam is controlled using collimators near where the beam exits the linac. A collimator is a device that narrows a beam of particles and this artificial process gives the medical physicist a greater accuracy when delivering a radiation dose to the patient.

The principle by which radiotherapy is an effective treatment of cancer is to exploit the effect of ionising radiation on human cells. Damage from ionising radiation can range from superficial skin burns to internal organ damage, however the most devastating effect of ionising radiation is caused by the mutagenic effect of ionising radiation on human cells, causing mutation within cell DNA. Indeed if a patient is mistreated the effect of radiotherapy could be, more than failure to treat the illness, the potential risk of causing a new incidence of cancer. It is for this reason there is such a widely accepted need for systematic error checking and QA throughout the entire treatment programme of radiotherapy.

2.6.1 Apoptosis - PCD for Multicellular Organisms

This section outlines the effect of ionising radiation on the cells of human tissue. It is by this mechanism that radiotherapy is used to treat cancer.

Cell apoptosis triggers cell death as a response to a variety of different signals. This variety of triggers for cell apoptosis is best illustrated by Figure 2.5 [40], and includes; triggering a cell's death receptors, exposure to certain viral

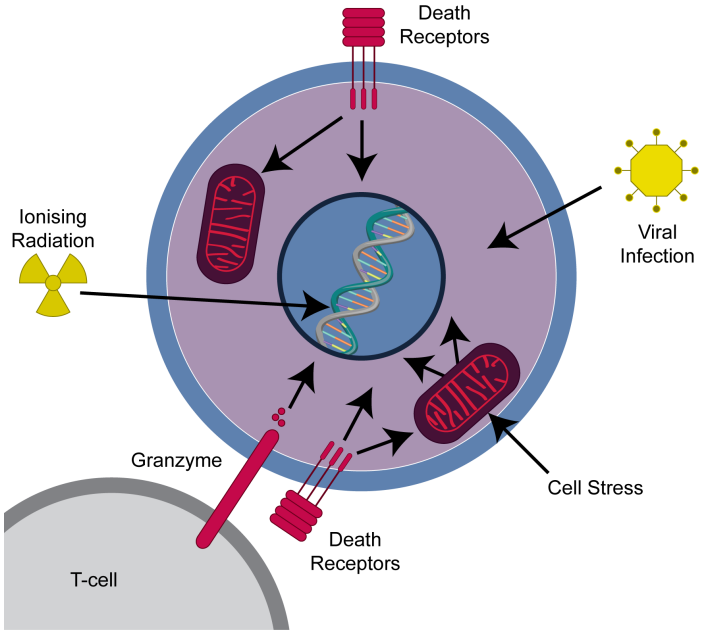

Figure 2.5: Common signals that instigate apoptosis in a cell [40].

infections, cell stress like nutrient deprivation, T-cells recognising damage to the cell, and ionising radiation damaging cell DNA. Apoptosis, otherwise known as Type I PCD, is a normal process available to multicellular organisms. The apoptotic process enables a cell to instigate its own death in a controlled and regulated fashion [41]. The sensitivity of a cell to apoptotic causing stimuli can vary depending on a number of factors, a characteristic exploited by the medical physicist designing a patient's treatment.

Ionising radiation can trigger PCD by acting as a mutagen and the exposure of a cell to ionising radiation will result in the frequency of mutation in the cell's genetic material to become elevated above the natural background rate. The damaging effects of radiation induced mutation in a cell's DNA can instigate the process of apoptosis in a cell.

The apoptotic effect of ionising radiation on living cells is characterised by three distinct phases: the physical, the chemical, and the biological. Figure 2.6 illustrates this point [42]. For an individual cell these three phases do not overlap, rather they are consecutive, where each subsequent phase is instigated as a result of the previous phase. The importance of each phase

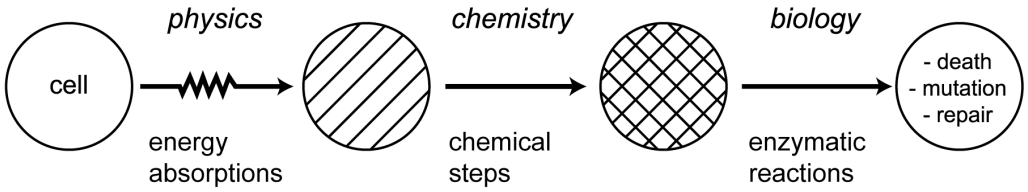

Figure 2.6: The 3-stage effect of ionising radiation on cells [42].

occurring exclusive to the others is a contributing reason to why the treatment of cancer with radiotherapy is broken into fractions. Apoptosis in a cell only occurs once the biological phase is reached and not before. However apoptosis is only one of three possible outcomes caused by cell exposure to ionising radiation. To trigger the death of cancer cells enough time is needed for the ionising radiation to have caused the eventual resulting biological effect.

Apoptosis: The Physical Phase

In 1923 Arthur Holly Compton described the behaviour of high energy photons as they interact with matter [43]. Compton scattering is the name given to a phenomenon exhibited when high energy photons ($\sim$ 25 KeV to 25 MeV) interact with atoms. Compton scattering describes the inelastic collision between a photon and an electron. Inelastic scattering is a fundamental scattering process in which the kinetic energy of an incident particle is not conserved. Compton observed that when an incoming photon is absorbed by an orbital electron there is an exchange of energy. Part of the energy of the incoming photon is transferred into the orbital electron giving it sufficient energy to break from its orbit. The remaining energy is released as an incident photon of a higher wavelength. Should the incident photon have sufficient energy the process will reoccur on its next interaction with an orbital electron.

Should the number of electrons orbiting an atom not equal the number of protons in the nucleus of that atom then that atom will have an electric charge. The magnitude and polarity of the charge on an atom is determined

by the ratio of electrons orbiting the nucleus of the atom to the number of protons within its nucleus of the atom. An atom with an electrical charge is called an ion. Thus, radiation with sufficient energy interacting with orbital electrons is referred to as ionising radiation when the energy of the radiation is sufficient to make ions of the atoms it interacts with.

Compton scattering is the most probable effect expected from photons produced by a clinical linac for radiotherapy as the energy of photons used in this medical context range from 50 KeV to 25 MeV. To understand the consequence of Compton scattering in radiotherapy a closer look at the effects of Compton scattering amongst atoms within molecules is required.

Apoptosis: The Chemical Phase

A molecule is a group of atoms that share a strong chemical bond. A covalent bond describes a type of strong chemical bond that forms when a pair of outer-shell orbital electrons is shared between two atoms. When Compton scattering occurs amongst the orbital electrons of the atoms forming a molecule then the result is the production of a free radical. A free radical is a molecule with an atom that has an unpaired outer-shell electron and, therefore, a highly reactive molecule due to its chemical imbalance. If an ion is made of an atom that was originally part of a covalent bond then the bond those atoms once shared becomes broken.

The chemical effect of ionising radiation is broken into two. First, the direct effect where the molecules of DNA are damaged directly. Second, the indirect effect where ionising radiation causes an increase in the number of highly reactive free radicals within the molecules of the cell. The production of free radicals is by no means an area of research unexplored [44, 45, 46]. If these free radicals interact with the molecules in the cell's DNA this can cause irreversible damage to the cell's DNA.

Apoptosis: The Biological Phase

The structure of the DNA double helix is shown in Figure 2.7 and highlights the grouping of molecules in the DNA structure. The illustration of Figure 2.7

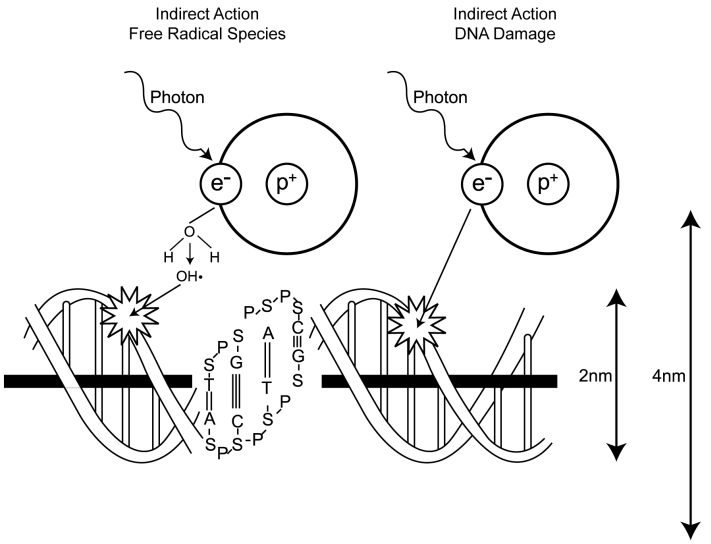

Figure 2.7: Compton scattering in or around DNA molecules will cause double strand breaks and eventual apoptosis [47].

also highlights ionising radiation as having both a direct and indirect effect on a cell's DNA [47].

The effect of free radicals on cell biology is an extensively researched area of interest for the study of inflammatory diseases and the progression of cancer [48]. Free radicals, known as reactive oxygen species (ROS) and reactive nitrogen species (RNS), are known to occur naturally in the human body. However, unnaturally high quantities of ROS and RNS free radicals in the body can be a cause of cancer. Despite this fact in radiotherapy the exploited biological effect of cell exposure to ionising radiation is the eventual trigger of apoptosis.

The production of free radicals within the cell causes lesions to the molecules within the cell, and the production of molecular lesions within the cell triggers an enzymatic response within the cell. The vast majority of the damage to the integrity of a cell's molecules (including a cell's DNA molecules), caused by ionising radiation, is successfully repaired by the enzymatic response of the cell. It is only when the molecular lesions of the cell are beyond the repair of the cell's enzymes that apoptosis is triggered within

the cell. The biological phase is characterised by apoptosis being triggered within the cell. Cell death is not an immediate response once apoptosis is triggered. In fact a cell will undergo several more mitotic division before PCD is achieved.

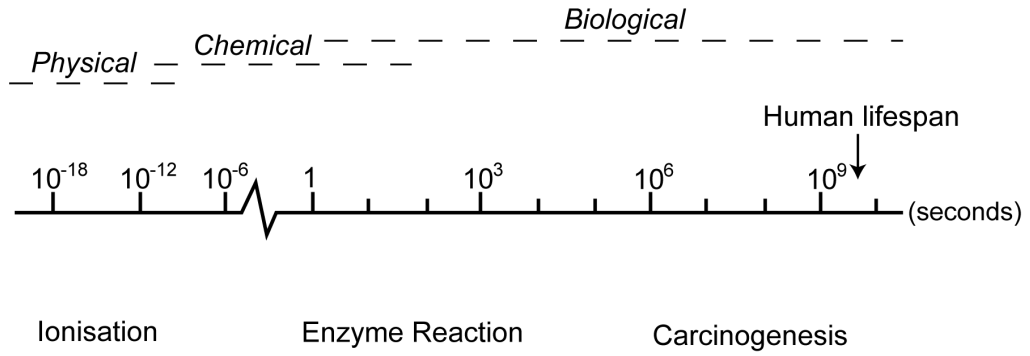

Figure 2.8: Timescale of apoptosis caused by ionising radiation [49].

For a 1 Gy of absorbed dose of ionising radiation there are in excess of 105 ions causing direct or indirect events that occur within the volume of every cell of diameter 10 μm, and despite this rate of events occurring when a cell is exposed to ionising radiation Figure 2.8 highlights just how long it takes those ions to trigger PCD within a cell [49]. This timescale plot in Figure 2.8 helps to further explain the need for a recovery time between radiotherapy fractions. Without a break between radiotherapy fractions the cells would not have enough time to achieve the full intended biological effect of ionising radiation exposure.

The time it takes for apoptotic cells to disappear in tissue varies depending on the type of cell being irradiated. The duration of apoptosis is around three to twelve hours in the cease of the epithelial lining of the small intestine [50]. It is therefore suggested that the duration of apoptosis is of the same order of magnitude as the average time it takes to the cell's DNA to replicate [50]. By that measure the scale of time for a radiation induced apoptotic response for stomach cancer is around 10^3 to 10^4 seconds, as measured on the plot in Figure 2.8.

2.6.2 Dose Response Curve

Knowing that apoptosis in cancer cells is the intended effect of exposing a cancer patient to a source of ionising radiation, and that apoptosis in cancer cells is a delayed response when cancer cells are exposed to a source of ionising radiation, there still remains the calculation of the optimum radiation dose in the treatment of a patient's cancer.

The probability of ionising radiation triggering apoptosis in an individual cell is reasonably unpredictable, however, when ionising radiation is targeting a cancerous growth/tumour/tissue, where there are several thousands of malignant cells grouped together, then the outcome is more predictable.

When irradiating a patient's cancer the response of the target volume can be characterised by its dose threshold. Should the target volume be irradiated below the dose threshold then the outcome of the treatment will be no observable clinical effect. Conversely, treat the patient with a dose of ionising radiation above the dose threshold and a measurable reduction in tumour size will occur within the target volume. The dose threshold is therefore the minimum dose of ionising radiation the medical physicist will want to expose the patient's cancer to in order to achieve tumour reduction. The maximum dose of ionising radiation the medical physicist will want to expose the patient's cancer to can be determined by considering the radiosensitivity of the cancer cells. The radiosensitivity of a cell is a measure of the relative absorbed dose of ionising radiation necessary to trigger PCD within that cell. Thus the radiosensitivity is a measure of how sensitive the cells of the target volume are to ionising radiation, where a greater radiosensitivity of tumour tissue compared to surrounding healthy tissue is favourable. A greater radiosensitivity of tumour cells will determine the maximum dose of ionising radiation the medical physicist will want to expose the patient's cancer to.

Refer to Figure 2.9 and consider again the point that the radiosensitivity of a cell quantifies the apoptotic response of the cell. The most effective tumour control achievable is when the dose response curve of the tumour is at a lower level than the dose response curve of the healthy surrounding tissue. In this way, a minimum chance of complications due to radiation in healthy

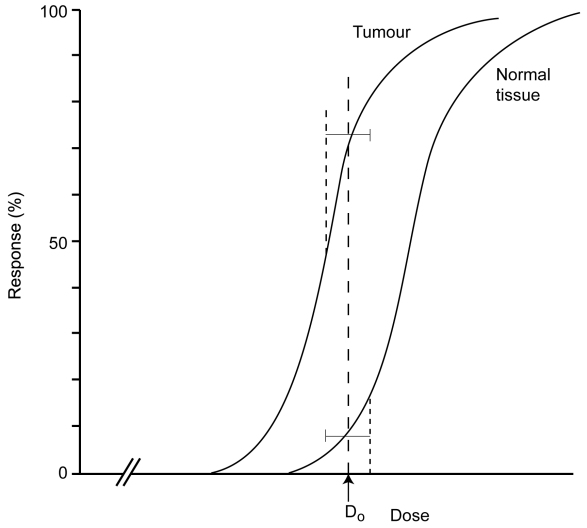

Figure 2.9: The dose response curve plotting the relative radiosensitivity for both the tumour cells and the surrounding healthy tissue. D_0 is the intended treatment dose [9].

tissue is observed. The greater the refinement in dose delivery technology for radiotherapy the smaller the needed separation between the tumour dose response curve and the healthy tissue response curve. Depending on the accuracy of the beam of ionising radiation from the linac the greater the need for separation of the two radiosensitivity plots in Figure 2.9 [51, 52]. Radiotherapeutic success is most probable when the two curves in Figure 2.9 are widely separated [9], in which case a higher dose of radiation can be delivered to the target volume without damaging neighbouring healthy cells.

Due to the radiocurability of a particular cancer being related to radiosensitivity of cancer by comparison to the radiosensitivity of its surrounding healthy tissue, understanding the reason why cancerous cells are more prone to the harmful effects of ionising radiation is critical to the treatment technology. Counting mitotic figures by light microscopy is a commonly practiced low cost method for estimating tumour proliferation [53], and, as a characteristic of cancer is the accelerated rate of mitosis, counting the rate of mitosis is a helpful tool when making a diagnosis. Cancer cells are more sensitive to the harmful effects of radiation exposure because they are are dividing rapidly,

and so cells with a lower rate of mitosis tend to have a lower radiosensitivity threshold [54].

2.7 Dosimeter Technologies

An extensive review of the most popular options for dosimetry in radiotherapy has been compiled elsewhere [55]. However, for completeness, this section outlines what alternative types of commercial dosimeters for radiotherapy are available today. By the end of this section a comparison between all dosimeters introduced in this section will be included, as will a summary highlighting where improvements can be made in presently available dosimetry technologies.

Broadly speaking dosimeters for radiotherapy can be broken into two categories; linac calibration, and treatment dosimeters.

Linac calibration and x-y cross sectional profile of the beam are critical routine system diagnostics made by the medical physicist before any patient is treated. Typically the linac at an oncology clinic will have a diagnostics' schedule that will make up part of the routine maintenance of the linac machine. Like all industrialised precision equipment periodic calibration of the linac and its beam provide confidence that the equipment will operate correctly during patient treatment. Commercially available technologies that are used for calibration of a linac include: the WP34 [56], Figure 2.10(a), a 1-D water based phantom from IBA Dosimetry that is designed for dose measurements of a radiation beam with horizontal beam incidence. The water component of a water phantom will replicate a likeness of a patient's composition. Knowing the dimensions of the phantom, the position of the dosimeter inside the phantom, and the distance the phantom is from the linac, calibration of the absorbed dose is completed by comparing the measured dose with the intended dose. The ArcCHECK [57], Figure 2.10(b), from Sun Nuclear is another pre-treatment dosimeter used by a medical physicist to calibrate the linac. The profile of the absorbed dose of radiation provided by a cylindrical calibration unit will more accurately characterise the cross sectional beam profile for the radiation source. Although the use of these

(a) Water phantom.

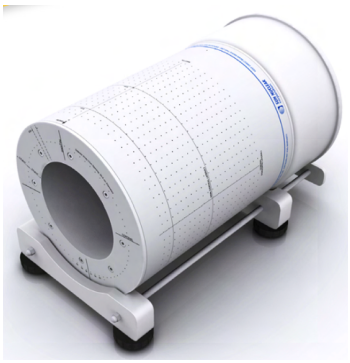

(b) Cylindrical detector.

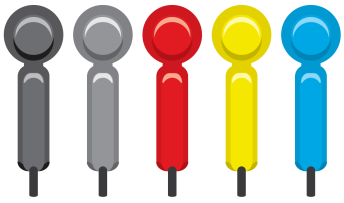

(c) Diode detectors.

(d) MOSFET detectors.

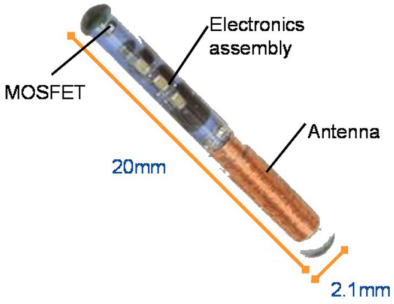

(e) Implantable dosimeter.

Figure 2.10: The above listed dosimeters are commercially available solutions suitable for radiation measurement in radiotherapy, including; linac calibration (Figure 2.10(a) and Figure 2.10(b)), and treatment measurements (Figure 2.10(c), Figure 2.10(d), and Figure 2.10(e).

calibration and cross sectional beam profiling dosimeters is necessary for the upkeep and routine maintenance on a linac they have one major limitation. This type of dosimeter is not designed to be present during patient treatment and cannot be used when it comes to the verification of the dose delivered to the patient under treatment.

The treatment dosimeter is a critical routine verification device used by the medical physicist during patient treatment to approximate the absorbed dose of radiation at the target volume. The treatment dosimeter refers to the commercially available dosimeter used to measure the received dose at the surface of the patient where the beam of ionising radiation will pass through. The treatment dosimeter is therefore placed directly above the location of the target volume and accurately measures the absorbed dose of radiation directly above the location of the target volume. The result from this measurement is then used to mathematically approximate the absorbed dose of radiation at the target volume. Knowing that the linac gantry is purposefully designed to rotate around the patient to evenly distribute the collateral dose of ionising radiation to the surrounding healthy tissue, and because the treatment dosimeter is positioned directly above the location of the target volume, this type of dosimeter can only accurately measure the absorbed dose of radiation when the linac beam passes through an axis including the dosimeter. Commercially available treatment dosimeters used during patient treatment to measure the absorbed dose of radiation directly above the location of the target volume include: the QED diodes [58], Figure 2.10(c), developed by from Sun Nuclear. This is an example of a diode based dosimeter that is taped to the surface of the patient and connected by a cable to a readout box measuring the absorbed dose of radiation as the radiation beam passes through it. Another example of a treatment dosimeter is the mobileMOSFET solution [59], Figure 2.10(d), from Best Medical Ltd., a Canadian company that makes this dose verification system. This solution provides wireless communication between the FGMOSFET device that is positioned on the body of the patient and the receiver module outside the treatment room. The medical physicist delivering the treatment can monitor the receiver module and ensure no unintended overdose occurs during

the patient's treatment. Although the use of these treatment dosimeters is practiced in the verification of the dose delivered to the patient under treatment they have one major limitation. This type of dosimeter is designed to provide an approximation of the absorbed dose of ionising radiation at the target volume. This type of dosimeter cannot be used to determine the precise absorbed dose of ionising radiation at the target volume. The approximated absorbed dose of ionising radiation at the target volume is calculated using a mathematical model.

There is one final commercially available dosimeter that is worth mentioning as it embraces the literal meaning of IVD, it is the implantable dosimeter [60] from Sicel Technologies, Inc. as seen in Figure 2.10(e). The device is surgically implanted near the tumour, activated before treatment, and irradiated along with the rest of the target volume during treatment. After treatment, communication is reestablished with the device and the measured dose at the target volume is reported back. This type of dosimeter provides a measurement of the absorbed dose of ionising radiation at the target volume. What's more, because this dosimeter is implantable, it provides a measurement of the absorbed dose of ionising radiation at the target volume for all axis the linac gantry will rotate through whilst completing the treatment. What's more, if CT imaging is used in conjunction with this technology and the location of the implanted dosimeter is known with respect to the tumour, it will verify if the intended dose of ionising radiation has been delivered to the intended location. This type of implantable wireless technology provides improved QA in radiotherapy while accommodating the natural movement of the body's internal organs.

To provide additional clarity on the relative merits of commercially available dosimeters for radiotherapy Table 2.1 is included. Table 2.1 is a comparison of the different features to each of the established technologies. The labels across the top of Table 2.1 refer to the different types of commercially available dosimeters for radiotherapy, and the labels down the left hand side of Table 2.1 refer to their features. A more complete summary of the list of features includes:

	Phantom	Cylinder	Diode	MOSFET	Sicel
Linac Calibration	✓	✓			
Real-Time			✓	✓	
In Treatment			✓	✓	✓
Wireless				✓	✓
No Approx. Dose					✓
Local Measurement					✓

Table 2.1: A comparison of the features between commercially available dosimeters for radiotherapy.

- Linac Calibration - The dosimeter is used during routine calibration of the linac.
- Read-Time - The dosimeter can provide measurement of absorbed does as it is delivered.
- In Treatment - The dosimeter is used whilst the patient is undergoing treatment and receiving a dose of ionising radiation.
- No Approx. Dose - The dosimeter measures the absorbed dose of ionising radiation at the target volume, and therefore the measured absorbed dose is not an estimate based on a proximity measurement.
- Target Volume - The dosimeter can occupy a space next to the tumours growth being treated.

Considering the work carried out for this thesis is towards building a next generation dosimeter for IVD understanding the merits and short comings of the established order of dosimeters for radiotherapy is a suitable starting point when attempting to conceive a better future for QA in radiotherapy.

2.8 Dosimeter Requirements

IVD is a QA technology intended to improve safety in radiotherapy by measuring the absorbed dose of ionising radiation the target volume is exposed to during a treatment fraction. IVD provides independent verification of dose

received by the target volume by comparing the intended dose and the measured absorbed dose. This comparison will confirm if the correct dose was delivered to the correct location during treatment. Confirmation of intended dose at the target volume is a QA measure for radiotherapy bringing confidence to both patient and medical physicist that the treatment was successful without unnecessary risk to the patient's health.

The work carried out for this thesis is towards building a completely new and novel dosimeter for IVD that improves on the present standard of QA in radiotherapy. One of the critical problems with IVD today is that the majority of dosimeter technologies available on the market do not accurately measure the absorbed dose at the target volume. Instead an approximation of the absorbed dose is calculated based on external dosimeters measurement. To rectify this issue the proposed dosimeter for IVD should be implanted within the patient's target volume. In this way IVD will verify; the absorbed dose of ionising radiation at the target volume, beam accuracy at the target volume, and treatment accuracy for all fractions. The most popular argument opposing routine implantable dosimeters for IVD is cost. Thus any new implantable dosimeter should be cost effective. That means something small enough that it does not require expensive surgery to be implanted.

A list of requirements for a dosimeter that improves the standards of QA in radiotherapy includes:

- Extremely small size, ~ 1 mm^3.
- Implantable.
- Target volume proximity, act as seed marker.
- Wireless communication.
- Real-time dose measurement.
- Self powered.
- X-ray and Hadron sensitive.
- Multiple detectors for optimum measurement resolution.

- Low cost.

A composite particle, like protons and neutrons, are classed as hadron particles as they are held together by the strong force, whereas atoms and molecules are held together by the electromagnetic force. As a relative measure of the difference between the strong force and the electromagnetic force, at the atomic scale, the strong force is about 100 times greater than the electromagnetic force.

2.9 Dosimeter Design

This thesis presents the work carried out in two separate studies where each presented study is investigating one of the four technology areas necessary to prototype a dosimeter for IVD. The work completed to produce this thesis is building towards a new type of implantable micro dosimeter for routine use during radiotherapy treatment and is intended to transform the standards of QA in radiotherapy by providing a cost effective solution for accurate measurement of absorbed dose of ionising radiation at the target volume for each treatment fraction. This section will outline a proposed prototype design to be used.

To better understand the possible structure of a new and novel implantable dosimeter for IVD a high-level block diagram, illustrated in Figure 2.11, is used to highlight the four key technology areas necessary to prototype such a device. Presented in Figure 2.11 are four expected components to the proposed dosimeter: a power unit, an electronic unit, a sensing unit, and an RF unit. The results presented in this thesis are an investigation into potential technologies that could be used in the sensing unit and the RF unit from the block diagram of Figure 2.11.

The power unit needs to be a self contained power supply capable of providing sufficient current to drive the entire circuit for the duration of the dosimeter's operation. Some limited work has been completed to date to address this requirement, namely collaboration with the Cleaner Electronics Research Group at Brunel University, to include Lithographic Printed Vol-

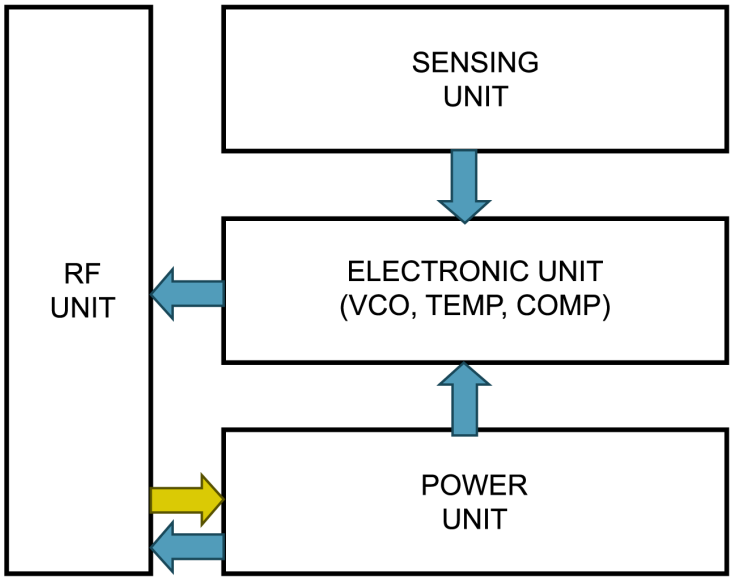

Figure 2.11: A high-level block diagram showing the technology areas necessary for a new and novel implantable dosimeter.

taic Cells [61, 62]. An alternative technology of interest includes the thin film micro-batteries [63, 64]. Given that the actual volume in which the battery must reside is > 1 mm^3 in volume (see Figure 2.12), the calculations published by Dudney [63] are interesting. A limiting factor in this work seems to be the thickness of the cathode film, approximately 5 μm presently. A thicker cathode film could guarantee 30 μWmm^2, a value close to the power requirements of the micro antenna.

For the electronic unit some work has been completed to date, mainly exploring VCO technology. Unfortunately work in this area only extends as far as the characterisation of the commercially available voltage-controlled oscillator (VCO) from Crystek Microwave [65], the CVCO33CL-0390-0410. This VCO will produce an oscillating output signal shifting between 310 MHz and 410 MHz based on the DC bias applied to the tuning voltage pin.

The two remaining units form the basis of the work completed to produce the results presented in this thesis. The inspiration for the sensing unit tech-

nology, characterised as part of the work completed and presented within this thesis, is provided by the accomplishments of the Particle Physics Department at RAL in their role to support the detector design for the Compact Muon Solenoid (CMS) experiment at Large Hadron Collider (LHC), CERN, and that was to exploit the sensitivity of silicon based detectors under exposure to ionising radiation. For the sensing unit the evaluation of the FGMOSFET as a suitable electronic component to measure the absorbed dose of ionising radiation it has been exposed has been characterised.

The RF unit is the other technology area that has been investigated and the result from that work are presented later in this thesis. Extensive work was completed to evaluate and characterise a custom design micro antenna optimised for the application of implantable medical electronic devices. For medical electronic devices providing biotelemetry a unique type of wireless communication is required, a custom designed micro antenna for implantable medical electronics which operates with low power consumption, low data transfer speeds, and over a short range. To complete the necessary work to evaluate and characterise the optimum antenna for this unique application the single-loop and multi-loop antenna design was investigated and characterised.

Before considering how the proposed dosimeter for IVD will be integrated into radiotherapy as a tool to modernise the standards of QA in radiotherapy a quick look at how the block diagram of Figure 2.11 can be abstracted into an integrated system on a single silicon based circuit is presented in Figure 2.12. It is clearly shown how the overall design requirement of a 1 mm^3 size for the entire implantable dosimeter is broken into its four technology components necessary to prototype the new dosimeter. The integrated solution, in the top right of the image in Figure 2.12, is expanded into a much larger digram illustrating how each of the four technology components for a new dosimeter would occupy the proposed volume of no more than 1 mm^3. The design includes two important regions, the radiation sensitive region and the wireless communication region. This thesis is the presentation of work completed in both of these areas, the evaluation of the FGMOSFET as a radiation detector, and the performance of the micro antenna as a communications

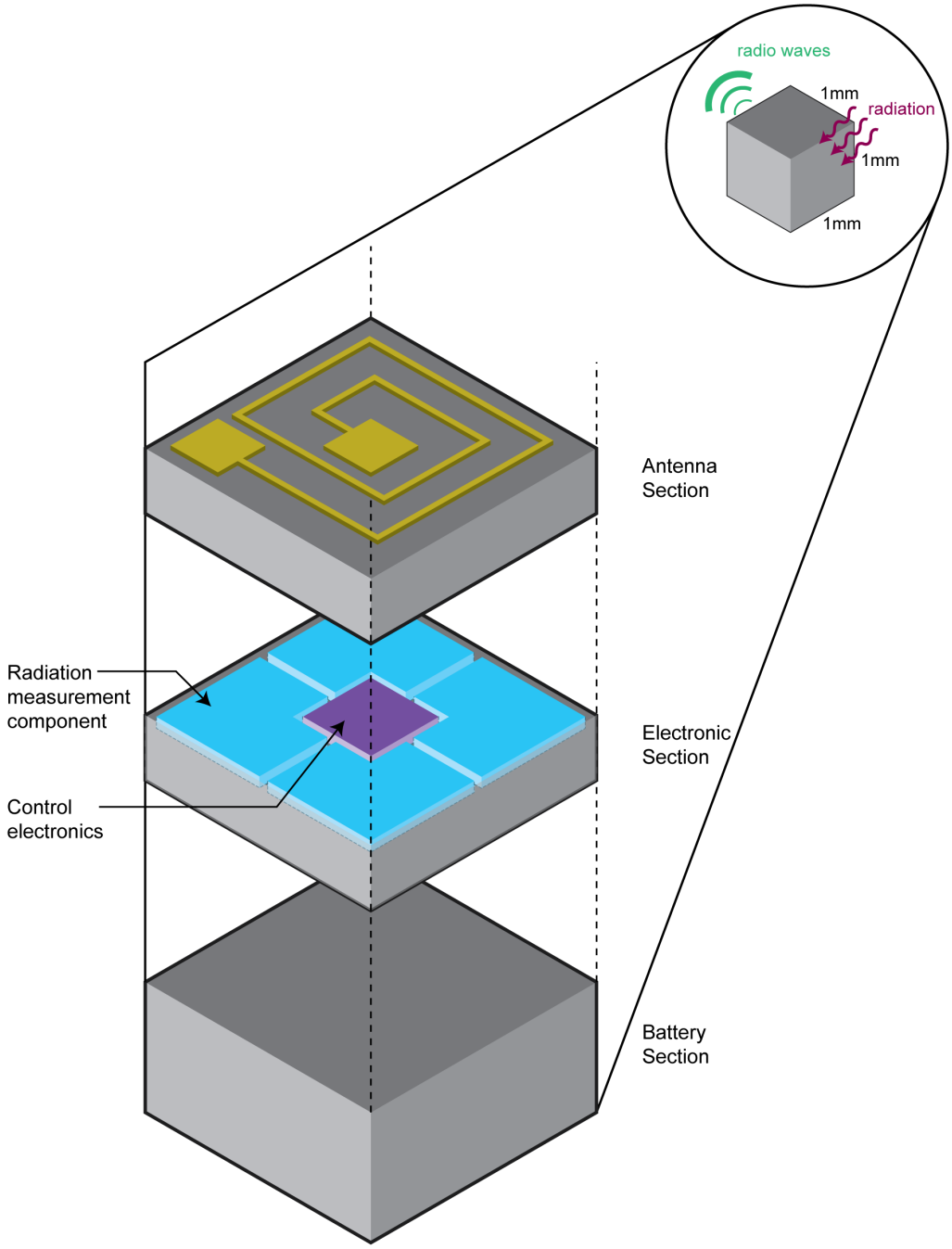

Figure 2.12: An integrated silicon solution for a new implantable dosimeter including all four technology areas of a functional prototype.

medium.

For the dosimeter design presented above the antenna is illustrated as a multi-loop design with a conductive wire trace in the top part first quarter slice from the device. This graphic is only a guideline about how the device may be constructed. In practice there may be fabrication issues that dictate the antenna's design and the electronics may all share the same layer on an integrated circuit.

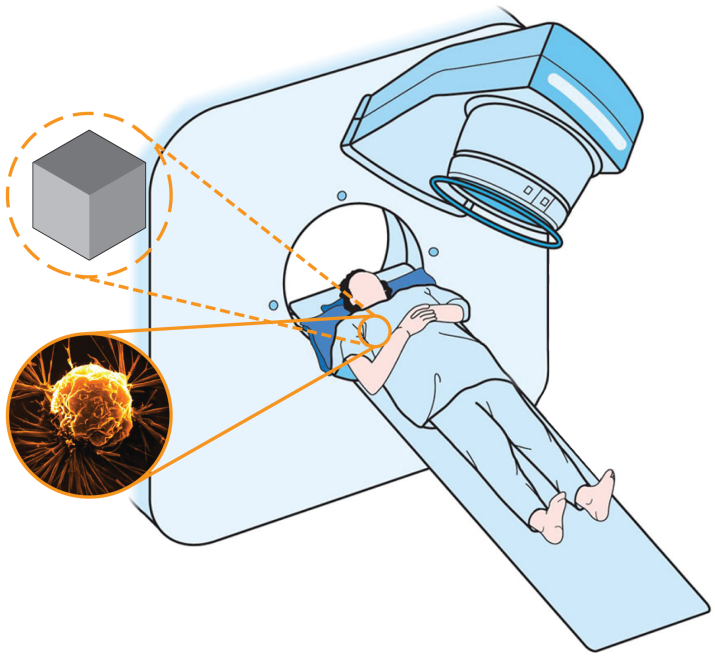

Figure 2.13: A rendering of the new dosimeter as it would be used to improve QA in radiotherapy.

Figure 2.13 illustrates how this proposed dosimeter for IVD will operate as part of the QA programme to improve confidence in radiotherapy treatment. Returning back to the original image in Figrue 2.3 to help contextualise the application of the proposed dosimeter, Figure 2.13 is a helpful illustration to better understand the intended use of the implantable dosimeter. From this image it is possible to understand the role of the dosimeter as a technology inside the patient within the target volume and with close proximity of the cancerous growth. The implanted dosimeter will measure the absorbed dose of ionising radiation the patient is exposed to during treatment and provide

that information in real-time to the medical physicist. This proposed dosimeter is about improving QA in radiotherapy by building an implantable dosimeter that exceeds the performance of the presently available commercial technologies.

A reasonable consideration at this stage is to ask how any proposed dosimeter might be implanted within the patient before treatment. To date there are a multitude of implantable technologies that are used as routine part of patient treatment [66]. The mechanism by which they are implanted may vary widely, from an innocuous injection [67], right through to surgery [68]. Indeed, in some instances, the implanted device can serve multiple purposes. In the case of the implanted dosimeter the device can act as the radiation measuring QA technology it is primarily designed for, but also act as a radiographic fiducial marker to identify the location of soft tissue anatomy on radiographic images used during both the planning and delivery of IGRT treatment [60]. The precedence and range of implanted medical technology gives confidence that a proposed dosimeter can be used as described, however the details regarding how the implantation of the propose dosimeter would be accomplished is a discussion best suited for when a fully tested prototype has been demonstrated to work.

2.10 Summary

This chapter has summarised the debate for routine in-vivo dosimetry in radiotherapy and found in favour of its use. From statistics on incidence rates in the UK to the potential errors in the treatment procedure of radiotherapy the merits of in-vivo dosimetry to improve quality assurance in radiotherapy have been presented. Also presented is a comparison of dosimeter technologies presently available for radiotherapy and highlighted the potential benefits from a new enhanced dosimeter, a dosimeter that could incorporate the best features from each of the established dosimeter technologies whilst integrating the very latest in detector design to optimise its performance.

Chapter 3

Transistor Theory

3.1 Introduction

The work completed for this thesis is towards building a new dosimeter for IVD, an instrument that needs to be capable of measuring a typical dose of ionising radiation a cancer patient is exposed to while undergoing a course of radiotherapy. To do this the new dosimeter will need to be sensitive to ionising radiation, respond reliably when exposed to ionising radiation, and be capable of electronically communicating the amount of ionising radiation it has been exposed to. This chapter presents a detailed explanation of what type of electronic component can be used as a radiation sensitive component and how that component is capable of measuring the absorbed dose of ionising radiation it is exposed to. However, before this practical application for an electronic dosimeter can be understood an overview of the supporting theory is necessary.

This chapter will begin with an overview of the chemistry of silicon and its structure. Following this is an explanation on the manipulation of pure silicon to favourably alter its chemical properties and fabricate doped silicon. Depending on the arrangement of this altered silicon it will form a variety of different electronic components all with their own unique applications and varying levels of complexity in behaviour. This theory forms the necessary fundamental working knowledge required to understand how a silicon based

electronic component can be used to predictably measure its exposure to ionising radiation.

The theory content of this chapter is well established and extensively documented elsewhere [69, 70].

3.2 Silicon

Silicon is the 14th element on the periodic table. It is a semiconductor with an atomic number of 14, an atomic weight of 28.09, and the symbol Si. Figure 3.1 provides an expression for this information. Silicon is the second most abundant element in the Earth's crust and in the form of silica it is used in glasses, cements, and ceramics.

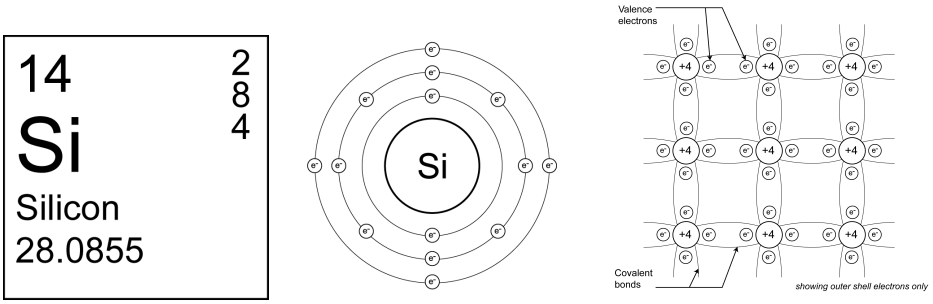

(a) Element. (b) Bohr diagram. (c) Lattice structure.

Figure 3.1: Silicon, the scientific description. Figure 3.1(a) as it appears on the periodic table. Figure 3.1(b) the Bohr diagram of the element. Figure 3.1(c) the lattice structure for intrinsic silicon.

Niels Bohr was a Nobel prize winning Danish physicist who history recognises for his contributions to, amongst other things, the understanding of atomic structure. In 1913 Bohr introduced an improved model for the structure of an atom that better describes the composition of the atom including the relationship between the nucleus and orbital electrons of an atom [71, 72, 73]. This model has become known as the Bohr model and will be used throughout this chapter. From Figure 3.1(b) the Bohr diagram illustrates the arrangement of orbital electrons around the nucleus of the silicon atom. From this illustration it becomes clear how the silicon element

is an electrically neutral atom with 14 negatively charged orbital electrons equalling the 14 positively charged protons within its nucleus. However in this configuration the silicon atom still requires a further four additional orbital electrons to make the atom a chemically neutral atom.

The element silicon, being without a full compliment of outer shell orbital electrons, is a reactive element on its own. But, in nature, silicon is commonly found bound to other silicon atoms and not bound with other elements through strong chemical bonds. To understand how silicon atoms bind with other silicon atoms so readily in nature a closer look is needed at the predicted behaviour of a single silicon atom as it neighbours other silicon atoms. The arrangement is illustrated in detail in Figure 3.1(c).

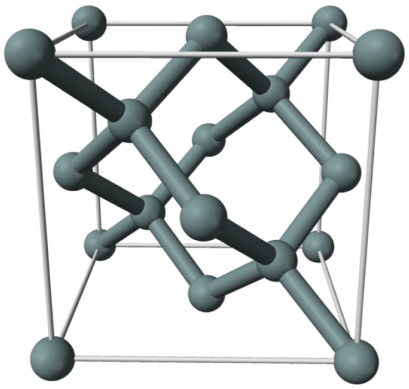

Figure 3.2: A 3-D illustration of the silicon lattice and is described to have a diamond cubic crystal structure [74].

Consider again the Bohr diagram from Figure 3.1(b) [74]. For the silicon atom to become chemically neutral it requires a full compliment of electrons to occupy its outer shell, a total of eight orbital electrons in all. A covalent bond is a bond between two atoms by sharing an outer orbital electron between the atoms. A covalent double bond is a bond between two atoms where each atom shares an outer orbital electron and, as a result, each atom gains an additional orbital electron for its outer shell while forming a strong chemical bond between each another.

The valency of the silicon atom is four and as such a single silicon atom requires an additional four orbital electrons to become chemically neutral.

If a single silicon atom has four neighbouring silicon atoms that each share one of their outer electrons in a covalent bond then the original silicon atom will have a full compliment of outer shell electrons. If this arrangement is maintained throughout the lattice all atoms form a diamond cubic crystal structure through strong chemical bonds. Depicted in Figure 3.2 this regular tetrahedral structure is both chemically and electrically neutral.

The electrical neutrality of a silicon lattice with four covalent double bonds is a point that should be explained fully. The overall number of orbital electrons in the outer shell of any single silicon atom has changed from four to eight. However for each of the additional orbital electrons a single silicon atom gains so too does it gain a strong chemical bond with a neighbouring silicon atom. That neighbouring silicon atom has its own protons in its own nucleus. As such the total number of electrons and protons within the intrinsic silicon lattice has remained equal. Thus the potential difference charge across the silicon lattice is 0. So the four covalent double bonds bring a single silicon atom four additional shared orbital electrons for its outer shell granting the silicon atom chemical neutrality whilst also leaving the electrical potential of the atom unchanged.

When silicon forms a pure lattice, i.e. without any impurities, it is referred to as intrinsic silicon. Since all the orbital electrons of intrinsic silicon are firmly held in strong chemical bonds there are no electrons free to conduct electricity at temperatures close to absolute zero. Thus intrinsic silicon at absolute zero acts as a perfect insulator.

3.2.1 Holes and Free-Electrons

The energy band gap is the minimum energy an electron needs to move from the valence band to the conduction band. The valence band refers to the highest energy electrons still bound to an atom at temperatures approaching absolute zero. The conduction band is the level required for an electron to escape its binding with its parent atom. An electron in the conduction band is free to conduct electricity.

The energy band gap is given by the symbol E_g. Should an outer shell

electron of an atom acquire this energy it will move from its orbit about the nucleus and become a mobile charge carrier able to move freely within the material. The magnitude of energy to cross the band gap is therefore a factor that determines the electrical conductivity of a material. Insulators typically have a large energy band gap. Conduction of charge carriers in a conductive material depends on partly filled bonds [74]. For silicon $E_g = 1.12$ eV at 302 K.

If an outer shell orbital electron of a silicon atom is able to move from the valence band to the conduction band it will become free to move within the lattice. The direction of movement of this electron is unpredictable unless it is under the influence of an electric field. An electron free to move in this way is called a free-electron. For the parent atom the free-electron has migrated away resulting in a vacancy to re-complete the outer shell valency. This absence in the parent atom's outer shell is known as a hole. The process where an outer shell orbital electron migrates away from its parent atom after acquiring the necessary energy to cross the band gap threshold is known as electron-hole pair generation. Electrons can fall spontaneously from the conduction band into the valence band, and should this happen it is referred to as recombination. The period during which both holes and free-electrons can conduct electricity independently is limited by the rate of recombination.

Electron density is the measure of the probability of an electron being present at a specific location. Free-electron density is the number of free-electrons per unit volume and given the symbol n. Hole density is the number of holes per unit volume and is given the symbol p. Within intrinsic silicon the process of electron-hole pair generation and recombination occur continuously such that there is an equilibrium between the number of holes and the number of free-electrons within the lattice. A semiconductor is therefore under equilibrium conditions when the rate of electron-hole pair generation is equal to the rate of recombination. The free-electron density under equilibrium conditions is denoted by n_0, and hole density under equilibrium conditions is denoted by p_0.

$$n_0 = p_0 \tag{3.1}$$

If the condition for Equation 3.1 is met it is referred to as the intrinsic carrier density of a material and is given the symbol n_i. Equation 3.2 is a mathematical description of the intrinsic carrier density.

$$n_0 p_0 = n_i^2 = N_c N_v e^{\frac{-E_g}{kT}} \tag{3.2}$$

The terms of Equation 3.2 include; k for Boltzmann's constant, T is the absolute temperature in Kelvin, and N_c and N_v are the effective density of states for the conduction and valency band respectively. From Equation 3.2 it can be seen the expression $e^{\frac{-E_g}{kT}}$ describes the electron-hole generation rate (R_{gen}), ignoring the necessary material dependent constant:

$$R_{gen} \propto e^{\frac{-E_g}{kT}} \tag{3.3}$$

The intrinsic carrier density is the product of hole density and free-electron density because the probability of recombination, where a free-electron falls into a hole, depends on the density of holes available and the density of the free-electrons available. The net average recombination rate is defined by:

$$R_{rec} \propto p_0 n_0 \tag{3.4}$$

The assumption of intrinsic silicon is that the electron-hole generation rate is equal to the recombination rate (R_{rec}), and is the product of thermal agitation, i.e. $R_{rec} = R_{gen}$. Thus the intrinsic carrier density can be characterised as:

$$n_i^2 \propto e^{\frac{-E_g}{kT}} \tag{3.5}$$

3.2.2 Diffusion and Drift

With intrinsic silicon there are two mechanisms by which hole and free-electrons can move through silicon.

Diffusion is the name given to the movement of either holes or free-electrons within a silicon crystal. There are two possible reasons for diffusion

within a silicon lattice. Thermal diffusion, as the name suggests, is an effect that does not occur when the silicon lattice is at temperatures close to absolute zero, only at temperatures above 0 K. As the temperature of a silicon lattice increases so too does the probability of an orbital electron escaping its parent silicon atom. The vacancy left behind by the migrating free-electron is a hole. Within intrinsic silicon the electron-hole formation due to thermal diffusion results in no net flow of charge. This is because electron-hole pairs formed by thermal energy do not change the potential difference across the silicon lattice despite it changing the local charge of a particular silicon atom.

However consider the situation where the concentration of free-electrons within a silicon lattice is particularly high compared to the surrounding region. If there are no other forces influencing the charge on the silicon lattice as a whole then the region of highly concentrated free-electrons will naturally diffuse into the regions of lower free-electron concentration. The result will be for the concentration of free-electrons to become as uniform as possible throughout the silicon lattice. The same is true for a concentration of holes within the silicon structure. The movement of charge in this manner is know as diffusion current.

$$J_p = -qD_p\frac{dp}{dx} \tag{3.6}$$

$$J_n = qD_n\frac{dn}{dx} \tag{3.7}$$

Equation 3.6 and Equation 3.7 describe the diffusion current within a silicon crystal where: J is the current density, q is the charge of an electron, D is the diffusion constant, and x is the direction of the diffusion current. p and n denote holes and free-electrons concentrations respectively. The sign in each equation shows the direction of movement of the charge.

Drift is the other mechanism by which charge moves within a silicon lattice. Carrier drift refers to the movement of charge under the influence of an electric field. The drift velocity of free-electrons and holes in a silicon crystal is a function of the electric field strength and given by Equation 3.8 and Equation 3.9.

$$v_{drift} = \mu_p E \tag{3.8}$$

$$v_{drift} = -\mu_n E \tag{3.9}$$

E is the electric field strength and μ_p is the mobility of holes. For the drift velocity of free-electrons Equation 3.9 has μ_n in place of μ_p, and the direction of travel is opposite to that for Equation 3.8 . The mobility of free-electrons in the conduction band is greater than the mobility of holes in the valence band by a factor of 10. The velocity of these charge carriers is determined by the electric field strength. Mobility is the constant of proportionality between the velocity of the charge carrier and the electric field strength, and is given the symbol μ.

If there is a higher concentration of either holes or free-electrons within a silicon lattice the region of high concentration will naturally drift to the region of low concentration to form an even concentration of charge throughout the silicon lattice.

An electron requires less energy to fill the hole of a neighbouring atom compared to the energy band gap an orbital electron needs to move from the valance band to the conduction band. As such, although free-electrons are free to conduct electricity in the space between atoms, the holes are free to conduct electricity quite independently within the lattice.

Holes carry a positive charge equal in magnitude to the negative charge of an electron. The electric current flow of free-electrons is within the conduction band and the electric current flow of holes is within the valence band. Effectively within a semiconductor there are two clouds of charge, one through the conduction band and the other through the valence band.

The mobility of free-electrons in silicon is considerably greater than the mobility of free-electrons in a good metallic conductor. The mobility of free-electrons in copper is 0.0035 $m^2V^{-1}s^{-1}$, and the mobility of free-electrons in silicon is 0.15 $m^2V^{-1}s^{-1}$, making free-electrons in silicon more than 40 times more mobile than free-electrons in copper. It would be easy to assume, therefore, that silicon would be a far more effective conductor of electricity. How-

ever, at room temperature, the number of free-electrons in copper is many times more than that of silicon, making copper a far better conductor. At room temperature the number of charge carriers within a metallic conductor like copper is at least equal to the number of atoms within that material. The number of atoms per unit volume between silicon and copper is about the same. For intrinsic silicon fewer than one free charge carrier per million atoms is expected.

3.2.3 Doping Silicon with Impurities

Intrinsic silicon, as discussed in Section 3.2, is a chemically and electrically neutral compound. Doping is the process of intentionally introducing impurity atoms to extremely pure silicon. The introduction of these impurities is intended to alter the chemical behaviour of intrinsic silicon and change it from a semiconductor to a doped semicondcutor.

The impurity elements are deliberately chosen as elements that will fit the lattice structure the silicon without changing the chemical structure of the lattice. Therefore the silicon lattice retains its diamond cubic crystal structure and, more importantly, it remains a stable compound.

The level of doping is also deliberate. The quantity of impurity atoms will be chosen depending on the required number of additional majority carriers. Heavily doped and lightly doped silicon are necessary depending on their intended application. Light and moderately doped silicon are referred to as extrinsic. Silicon doped to such high levels that it acts more like a conductor than a semiconductor is referred to as degenerate.

Silicon is doped always to alter the density of charge carriers within the silicon. The charge carriers are either holes or free-electrons. Doping silicon to introduce an increased density of holes is to create a p-type material, and doping silicon to introduce an increased density of free-electrons is to create a n-type material. p-type for positively charged doped silicon and n-type for negatively charged doped silicon.

Where intrinsic silicon has an equal number of charge carriers doped silicon has majority carriers and minority carriers. For a p-type material

the addition of a higher concentration of holes makes the holes the majority carriers and the free-electrons minority carriers. The opposite is true for n-type material, with the free-electrons of the n-type material being the majority carriers and the holes being the minority carriers.

p-type silicon

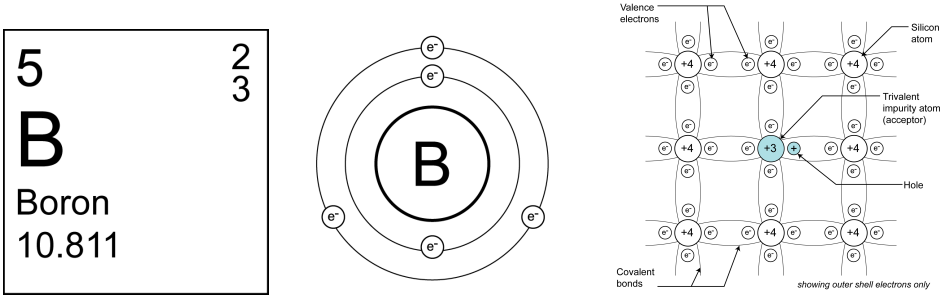

(a) Element. (b) Bohr diagram. (c) Lattice structure.

Figure 3.3: Boron, the scientific description. Figure 3.3(a) as it appears on the periodic table. Figure 3.3(b) the Bohr diagram of the element. Figure 3.3(b) the lattice structure for p-type doped silicon.

Every trivalent impurity atom added to a silicon lattice introduces a hole to the crystalline structure. To create p-type material a uniform distribution of trivalent impurity atoms are added throughout intrinsic silicon. The level of doping achieved is determined by the concentration of trivalent impurity atoms added to the intrinsic silicon. A trivalent atom is one that has three orbital electrons in its outer shell.

Boron is a typical trivalent impurity atom used for the p-type doping of intrinsic silicon. Figure 3.3(c) depicts how the trivalent impurity atom fits into the silicon lattice without dramatically altering the structure of the lattice. The greater the concentration of trivalent atoms throughout the intrinsic silicon the more additional holes become available within the p-type material. This addition of holes is independent of the holes created by thermal agitation. The trivalent impurity atom is called an acceptor atom and is given the symbol N_A.

n-type silicon

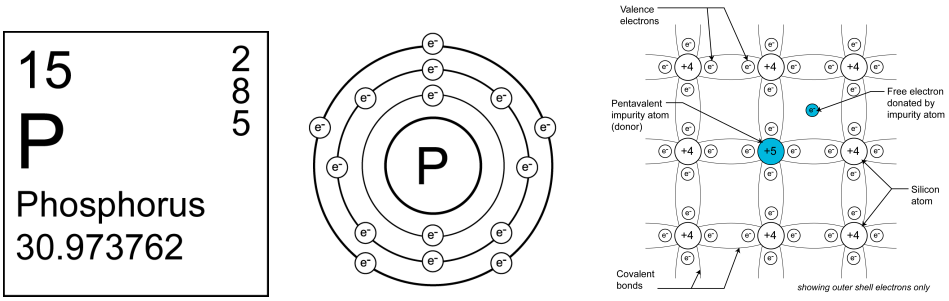

(a) Element. (b) Bohr diagram. (c) Lattice structure.

Figure 3.4: Phosphorus, the scientific description. Figure 3.4(a) as it appears on the periodic table. Figure 3.4(b) the Bohr diagram of the element. Figure 3.4(c) the lattice structure for n-type doped silicon.

Every pentavalent impurity atom added to a silicon lattice introduces a free-electron to the crystalline structure. To create n-type material a uniform distribution of pentavalent impurity atoms are added throughout intrinsic silicon. The level of doping achieved is determined by the concentration of pentavalent impurity atoms added to the intrinsic silicon. A pentavalent atom is one that has five orbital electrons in its outer shell.

Phosphorus is a typical pentavalent impurity atom used for the n-type doping of intrinsic silicon. Figure 3.4(c) depicts how the pentavalent impurity atom fits into the silicon lattice without dramatically altering the structure of the lattice. The greater the concentration of pentavalent atoms throughout the intrinsic silicon the more additional holes become available within the n-type material. This addition of free-electrons is independent of the free-electrons created by thermal agitation. The pentavalent impurity atom is called donor atom and is given the symbol N_D.

Properties of doped silicon

An alteration to the charge carrier mobility within the silicon lattice will only occur in heavily doped silicon, transforming intrinsic silicon into a p-type or an n-type material. The heavier the doping of the silicon the greater the

reduction of mobility to the charge carriers of the lattice. However just as copper is known as a good conductor of electricity by virtue of its available charge carriers so too does the semiconductor become an improved conductor of electricity by the introduction of charge carriers in greater densities. The greater the doping the closer to a pure conductor the semiconductor becomes.

For the doping of intrinsic silicon to transform the silicon into a useful semiconductor the number of introduced majority carriers should roughly make up all the majority carriers at thermal equilibrium such that, $n_0 \approx N_D$ or $p_0 \approx N_A$.

A point worth noting at this stage is the electrical neutrality of the doped silicon remains unchanged.

Boron, acting as a trivalent impurity atom, is used to create excess holes within the p-type material. A majority of holes within the doped silicon makes holes the majority carriers of that doped silicon. The boron atom, in isolation, has 5 protons in its nucleus and 5 orbital electrons around its nucleus. With the introduction of a boron atom as an impurity atom into a silicon lattice the boron atom will form a covalent double bond between each of its outermost orbital electrons, three in total, and the outermost orbital electrons of neighbouring silicon atoms. As the introduced impurity atom, boron, forms a covalent double bond with only 3 of its orbital electrons a neighbouring silicon atom is short of an orbital electron to form a covalent double bond with. This deficit of 1 orbital electron within the lattice is referred to as the 'hole' within the p-type material.

Phosphors, acting as a pentavalent impurity atom, is used to create excess free-electrons within the n-type material. A majority of free-electrons within the doped silicon makes free-electrons the majority carriers of that doped silicon. The phosphors atom, in isolation, has 15 protons in its nucleus, and 15 orbital electrons around its nucleus. With the introduction of a phosphors atom as an impurity atom into a silicon lattice the phosphors atom will from a covalent double bond between four of its outermost orbital electrons and the outermost orbital electrons of neighbouring silicon atoms. As the introduced impurity atom, phosphors, forms a covalent double bond with only 4 of its 5 outermost orbital electrons there is an excess of one orbital electron without

a neighbouring silicon lattice to form a covalent double bond. This addition of 1 extra electron within the lattice is referred to as the 'free-electron' within the n-type material.

The total number of protons and electrons across the doped silicon remains equal. The potential difference across the doped lattice remains at 0. This electrical neutrality of the doped silicon lattice shall prove to be a critical point when it comes to understanding the behaviour of the p-n junction, where the p-type and the n-type material are arranged side by side.

3.3 Diode

When p-type and n-type doped silicon are brought together it makes for a passive electronic component called a diode. A schematic showing the electrical symbol of the diode is illustrated in Figure 3.5(a) and the p-n junction is given in Figure 3.5(b). To better understand the electrical characteristics of the diode it helps to consider the behaviour of the junction between the p-type and n-type material when forming a p-n junction.

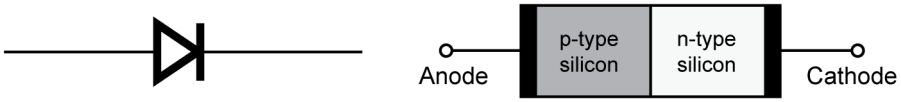

(a) Electrical symbol. (b) p-n junction.

Figure 3.5: The diode. Figure 3.5(a) is the symbol for the diode as it appears in a circuit diagram. Figure 3.5(b) shows the p-n junction of the component.

3.3.1 Electrostatic p-n Junction

Remember for both the p-type and n-type doped silicon the electrical neutrality characteristic of the intrinsic silicon lattice is preserved. Although the p-type material has been doped to have a higher concentration of holes to act as majority carriers, the overall ratio of electrons to protons is the same. Just as it is with the n-type material, despite the free-electron doping, the ratio of electrons to protons is approximately equal. The consequence is electrical

neutrality across doped silicon. Additionally, assuming no electric field and the uniform distribution of thermal energy, the distribution of any holes or free-electrons is uniform. It is important to keep both these ideas in mind when inspecting the boundary between the p-type and the n-type material in a p-n junction as depicted in Figure 3.6.

When the p-type and the n-type doped silicon are brought together there is suddenly an uneven concentration of majority carriers along the boundary of the two materials. The high concentration of holes from the p-type material defuse across into the n-type material, and the high concentration of free-electrons from the n-type material defuse across into the p-type matieral.

As such the free electrons of the n-type doped silicon diffuse across the junction border into the p-type region. Once there the free-electrons will be absorbed into the trivalent atom's outer shell and recombination will occur. The movement of the majority carriers from the n-type material is through the conduction band.

Equally the holes from the p-type region diffuse across the junction border into the n-type region. Once there the holes will be absorbed into the pentavalent atom's outer shell and recombination will occur. The movement of the majority carriers from the p-type material is through the valence band.

The consequence of this electrostatic movement is two fold. Firstly, the region of the doped silicon nearest the junction border will suddenly become depleted of its majority carriers. Secondly, the movement of holes away from the trivalent acceptor atoms of the p-type material will leave the acceptor atoms electrically unbalanced. Suddenly the acceptor atoms have had their holes filled in their valence band and thus become negatively charged. Just as the movement of free-electrons away from the pentavalent donor atoms of the n-type material will leave the donor atoms electorally unbalanced. Suddenly the donor atoms have had their free-electrons removed in their conduction band and thus become positively charged. The region surrounding the junction border that has consequently become charged is referred to as the depletion region.

This process of majority carrier diffusion will continue until the depletion region of uncovered charge becomes a potential barrier too great for the

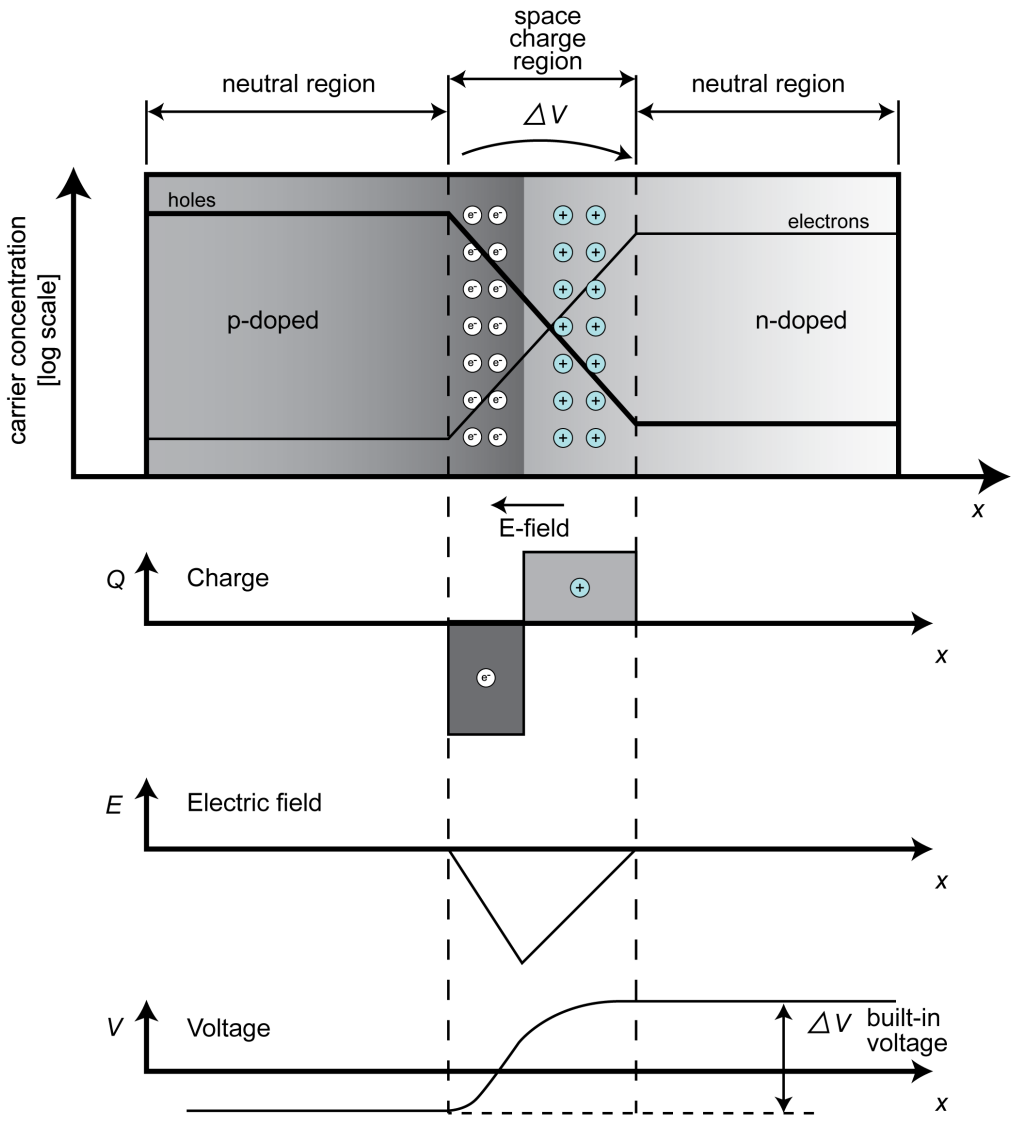

Figure 3.6: The diode's p-n junction under electrostatic conditions. The top image is an illustration of the electrostatic charge distribution for the p-n junction of the diode. The three lower plots describe across the space charge region: the charge, electric field, and potential difference.

migration of the majority carriers. The mobility of free-electrons is greater than the mobility of holes. As such more free-electrons diffuse from the n-type into the p-type than holes diffuse from the p-type into the n-type. This is illustrated in Figure 3.6 by the size of either region of uncovered charge.

The formation of the depletion region is a lending insight when the characteristics of the diode are studied with an applied electric field.

3.3.2 p-n Junction Capacitance

When a p-n junction is reverse biased the depletion region acts as a dielectric. The conducting p-type and n-type outside the depletion region act as the electrodes of a capacitor. In this way a reverse biased p-n junction has a capacitance.

The capacitance of the p-n junction is maximum when the applied reverse voltage is zero because this is when the width of depletion region is minimum. As the reverse bias voltage is increased the depletion region increases and the capacitance decreases.

$$C_j = \frac{\varepsilon_s A}{x_d} \tag{3.10}$$

The junction capacitance is modelled using the expression for the parallel plate capacitor. ε_s is the permittivity of silicon for the junction, A is the surface area of either side to the boundary of the depletion region, and x_d is the depletion layer width. The last term in the equation indicates that the expression of a parallel plate capacitor still applies. Any variation of the charge within a p-n junction of the diode that has an applied voltage across it causes a capacitance which should be included in any circuit model of a p-n junction.

The diode itself is a useful electronic component in its own right. However the use of the p-n junction only begins with diodes. The electrostatic analysis of a p-n junction helps to obtain the capacitance-voltage characteristic of the diode and this understanding builds the foundation of information necessary to understand the floating-gate metal oxide field effective transistor. By this comment, consider the structure of a more complex complement, the n-p-n

junction transistor. In this formation an outer n-type and the middle p-type form p-n junction, and the opposite outer n-type and the same shared middle p-type form a second p-n junction. The entire structure forms an active component, the transistor, and the FGMOSFET is a n-p-n junction transistor. Within the n-p-n transistor there are p-n junction capacitances that must always be considered when designing circuits with these silicon devices.

3.4 Floating-Gate MOSFET

The presented theory thus far in this chapter has explained how doped silicon can be used to form a two terminal electronic component, the diode. The next stage is to explore how doped silicon can be used to form a three terminal device, the transistor.

The FGMOSFET is a type of three terminal transistor device, and is ultimately the recommended electronic component that should be used when working towards an implantable electronic dosimeter for IVD. The attributes that make the floating-gate transistor suitable in the design of an implantable in-vivo dosimeter are presented in Section 3.4.4. However, before the FGMOSFET can be understood as an electronic component, it is best to begin by studying the MOSFET device.

3.4.1 MOSFET

This section will start with an overview of the physical structure to the MOSFET device, and continue by explaining just how the different voltages applied to the MOSFET can manipulate the behaviour of the MOSFET. To understand how the MOSFET works consider the MOSFET as a three terminal device where the current through the device is regulated by a voltage across the device.

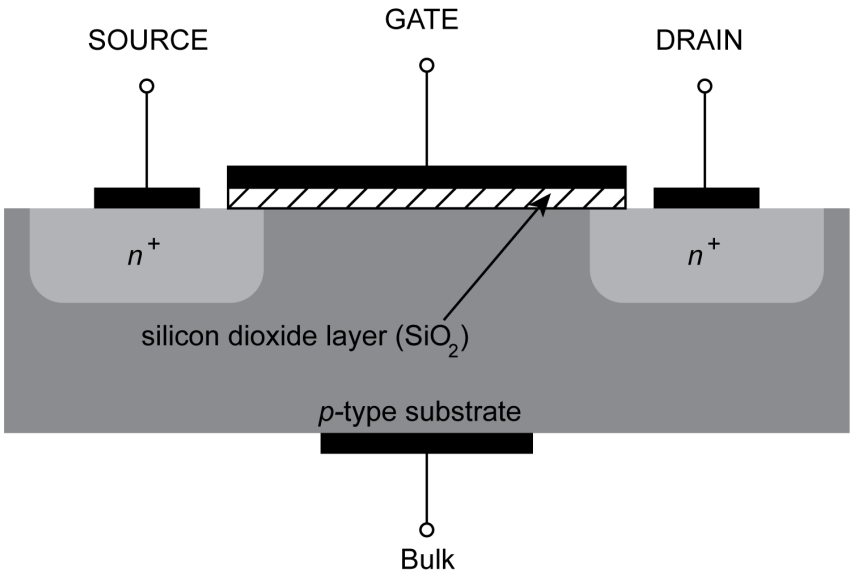

Figure 3.7: The silicon structure of the MOSFET device.

MOSFET Structure

The MOSFET is an electronic component made from doped silicon. Two regions of n-type heavily doped silicon are embedded at either end of a substrate of p-type doped silicon. This configuration makes the MOSFET a three terminal device but it does not describe the entire structure of the component. Having two regions of n-type heavily doped silicon between a region of p-type doped silicon makes the three terminal MOSFET two back-to-back diodes. As much is illustrated in Figure 3.7 where the '+' of the n^+ symbol denotes a heavily doped material.

Under electrostatic conditions the border of the p-n junction will have a depletion region devoid of majority carriers and, as with any electrostatic p-n junction, each depletion region will act as a dielectric of its own adding unwanted, but unavoidable, capacitances between the junctions of the device.

Regarding the remaining structure of the MOSFET a layer of silicon dioxide (SiO_2) is grown atop of the transistor covering part of either n^+ region and all of the p-type region between. Silicon dioxide is an insulator. Four electrodes are added to the device to interact with the transistor. The

source and drain electrodes are metallic nodes at either n^+, and, for now, which side is which does not matter. However the source should always be at lower electrical potential than the drain for the device to operate correctly. A third electrode is placed above the silicon dioxide region with a conductive plate covering the region. This metallic electrode is known as the gate. The remaining electrode is the bulk and it is located beneath the p-type substrate.

MOSFET Gate Voltage

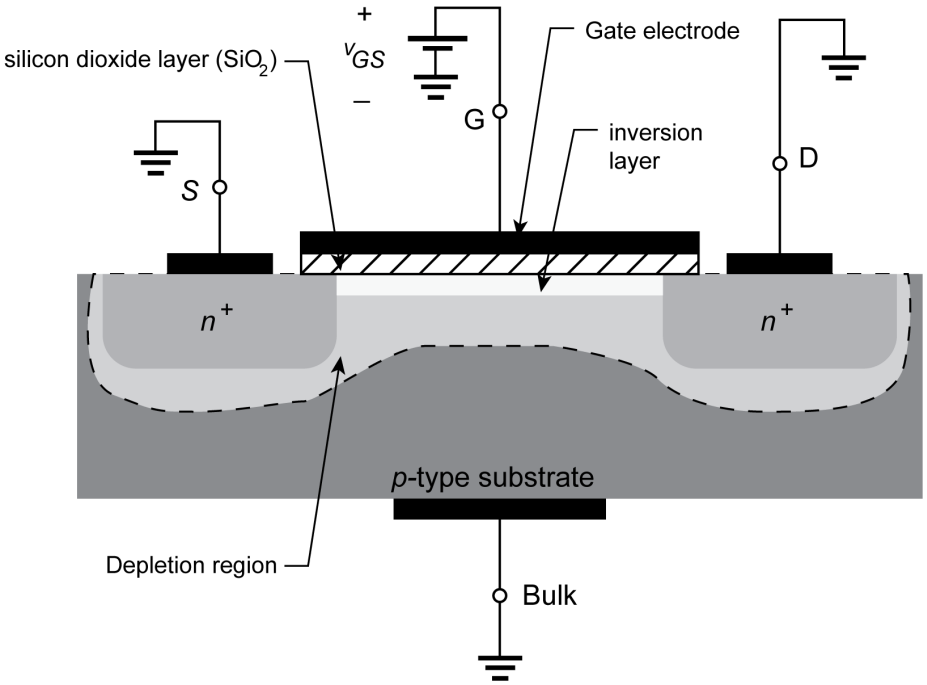

Figure 3.8: How a potential applied to V_{GS} effects the MOSFET.

The DC bias voltage at the gate is abbreviated to V_{GS} as it is the potential between the gate and the source junction. To understand what effect V_{GS} has on a MOSFET Figure 3.8 illustrates a circuit that has little use outside of this theoretical context. The source, drain, and bulk electrode are at ground, and V_{GS} has an electric potential applied to it. Applying a positive potential to the gate electrode in this way will cause a build-up of positive charge on the gate's conductive plate above the silicon dioxide region. This build-up of

positive charge will repel any majority carriers that may have been directly beneath the silicon dioxide region of the gate. The region directly below the silicon dioxide layer is known as the channel. As the majority carriers of the channel region migrate away into the substrate their impurity atoms become negatively charged. This uncovered negative charge in the channel region is directly proportional to the quantity of repelled majority carriers. In addition to the uncovered negative charge the majority carriers from the two heavily doped neighbouring n-type regions will migrate into the channel adding to the overall negative charge of the channel.

Having a layer of free-electrons flood the channel is why the channel is sometimes referred to as the inversion layer. Now that the gate electrode is positively charged and the inversion layer has become negatively charged by the introduced free-electrons, the result is a type of parallel plate capacitor where the silicon dioxide acts as the dielectric. Invisible electric field lines pass from the gate electrode, through the silicon dioxide layer, to the inversion layer. This electric field works to create a uniform distribution of the free-electrons through the depletion region.

Until a sufficient density of free-electrons accumulate throughout the channel there will not be a conductive link between the drain and the source electrodes. Should the channel have the required density of free-electrons throughout the entire channel region then a positive potential applied to the drain electrode would cause a flow of current from the drain to the source. When the MOSFET is conducting from the drain to source in this way it is said to be on, and the potential on V_{GS} to turn-on the MOSFET is referred to as the threshold voltage, abbreviated to V_{Th}.

MOSFET Drain Voltage

Figure 3.9 shows there are two types of V_{DS} voltage to consider to best understand the effect of V_{DS} on the behaviour of the MOSFET, V_{DS} at low voltages and V_{DS} at high voltages. In both examples the bulk and source are at ground, and $V_{GS} = V_{Th}$ (i.e. the transistor is on).

With V_{DS} at low voltages the effects are depicted in Figure 3.9(a). The

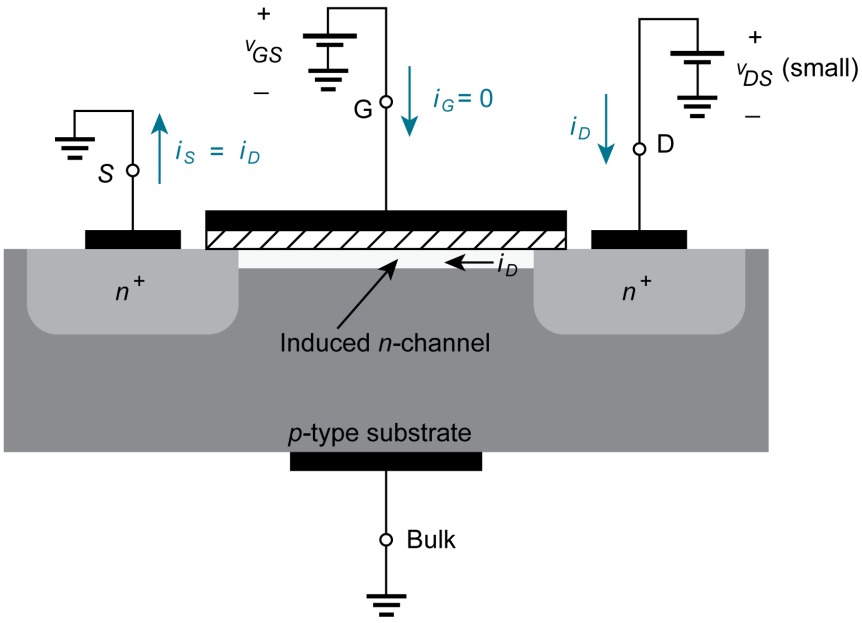

(a) V_{DS} at low voltages.

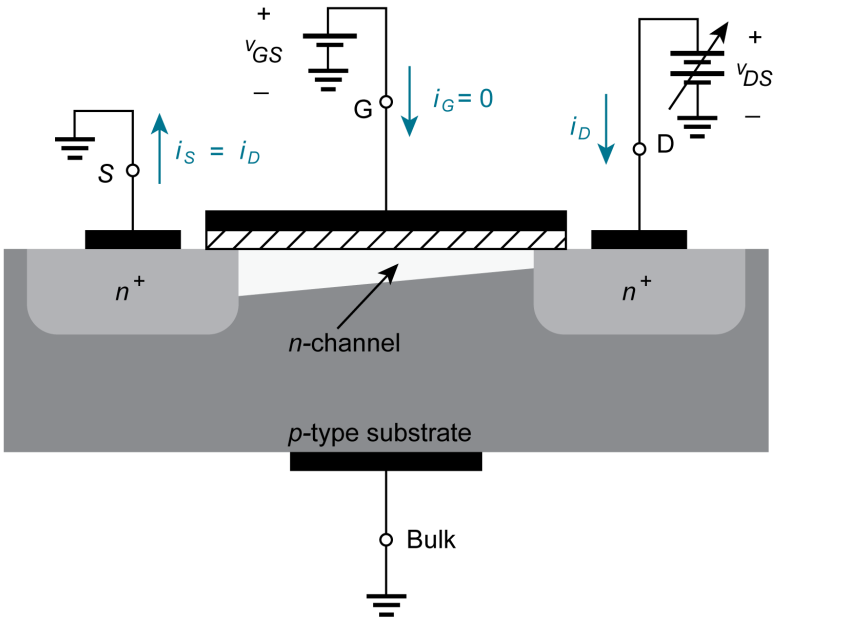

(b) V_{DS} at higher voltages.

Figure 3.9: The above two images illustrate how both a low, Figure 3.9(a), and high, Figure 3.9(b), potential applied to V_{DS} will effect the transistor differently based on a fixed V_{GS}. Notice at a high V_{DS} the channel shape is altered due to the lack of a uniform electric field from V_{GS}.

channel has sufficient free-electrons to move through the channel from the source to the drain under the influence of the electric potential on V_{DS}. In Figure 3.9(a) i_D is drawn in the direction of conventional current. The magnitude of i_D depends on the density of free-electrons in the channel which, as explained before, is regulated by V_{DS}. With $V_{GS} > V_{Th}$ then $i_D > 0$, and as V_{GS} increases i_D increases for a fixed V_{DS}.

With V_{DS} at higher voltages the effects are depicted in Figure 3.9(b). The channel still has sufficient free-electrons with $V_{GS} > V_{Th}$, however the shape of the channel is no longer uniform. With an increase in V_{DS} the electric field in the channel has changed. Although V_{GS} works to induce a uniform distribution of free-electrons in the channel with a higher V_{DS} voltage the effect of the electric field from V_{DS} tapers the channel. As such as V_{DS} increases with a fixed V_{GS} then i_D will increase to a point until i_D reaches a maximum value. Despite any additional increase to V_{DS} the i_D flow will remain unchanged and the transistor is said to be in saturation.

$$i_D = \frac{1}{2}\mu_n C_{ox}\frac{W}{L}(V_{GS} - V_{Th})^2 \tag{3.11}$$

From Equation 3.11 it is clear the simplest approach to configuring a MOSFET is to set V_{GS} to the required value to provide the desired i_D value. From Equation 3.11 i_D is the current in the channel, C_{ox} is the capacitance of the silicon dioxide region, μ_n is the mobility of electrons in the channel, and the W and L arguments are the width and length dimensions of the channel region. V_{Th}, C_{ox}, and $\frac{W}{L}$ vary widely among devices between manufacturers. V_{Th} and μ_n are dependent on temperature with the consequence that when V_{GS} is at a fixed value i_D becomes dependent on temperature. This is something worth considering when designing a MOSFET circuit.

MOSFET Applications

As a three terminal device the MOSFET, like all transistors, is able to control the flow of current by the use of an electric potential. This behaviour has two immediate practical functions, one in the analogue domain and the other in the digital domain.

Analogue applications of the MOSFET are much the same as they are for any transistor. The MOSFET device can be used as a current source for a circuit [75]. However the primary application for the MOSFET is as an amplifier [76]. To configure a MOSFET as an amplifier first the operating range must be identified. V_{GS} is biased with a DC voltage chosen such that it sits within the liner region of the i_D-V_{DS} plot whilst providing enough swing for the input signal such that distortion is avoided. The same is true for the biasing of V_{DS}. In this set up the V_{GS} is the input of the transistor and the output is taken from the drain. The measure of amplification achievable with a transistor is called the gain. In this mode of operation the MOSFET will act between the state of low current flow and high current flow through the channel.

The digital applications of the MOSFET are several. Should the flow of current transition from high to low, caused by an appropriate voltage bias, the MOSFET can act as a switch. If the high and low states of current flow are mapped as logic states then the MOSFET can act as a digital switch in a logic circuit [77]. Using the same characteristics of the MOSFET the device can be used as a memory device. However, in this type of memory device the memory is volatile and as such the transistor must always have a voltage supply to preserve the memory's state.

3.4.2 Floating-Gate MOSFET

The FGMOSFET is a transistor that is structurally similar to the MOSFET. The difference between the MOSFET and the FGMOSFET is the FGMOSFET has a floating-gate embedded within the silicon dioxide region and the MOSFET does not. Since the floating-gate is completely surrounded by a highly resistive material any charge within the floating-gate is electrically isolated and the charge within the floating-gate is said to be trapped. Whilst the transistor is under normal operation the trapped charge has no means of migrating away from the floating-gate.

Electron and Hole Injection

The internal emission of carriers in insulators has achieved some importance in the application of electron and hole injection in FGMOSFET devices. The process can be used to charge or discharge traps in the silicon dioxide region of the transistor, and provide a partial simulation of high-energy radiation [78]. With the internal photoemission approach light is used to excite charge carries [79], where electrons from the conduction band of the silicon migrate from the SiO_2 and travel through the oxide [80]. Alternatively an AC field across the silicon can be used to induce the avalanche process, causing the injection of hot-carriers [79]. By the avalanche approach, of the resulting hot-electrons and hot-holes, some of the charge carries have sufficient energy to cross the Si - SiO_2 barrier and migrate through the transistor.

In order to trap charge in the floating-gate region of the transistor the device needs to be programmed. Programming of the ALD1123E package, the transistor package under test, would exploit the avalanche approach of introducing hot-carriers from the SiO_2 region. Typical mechanisms of programming the FGMOSFET are to use the Fowler-Nordheim tunnelling [81] and hot-carrier injection techniques. To load charge into the floating-gate a specific voltage is applied to V_{GS} in order to induce hot carriers that become trapped in the floating-gate.

Trapped Charge on the Floating-Gate

The addition of trapped charge on the floating-gate alters the electrical characteristics of the device. A FGMOSFET, as with any MOFSET transistor, has an 'on' voltage that is required in order to induce an inversion layer under the SiO_2 region of the transistor. The 'on' voltage is referred to as the threshold voltage, V_{Th}, as it is voltage necessary before the transistor will pass current from the drain to the source, the threshold before which the transistor is 'off'. The V_{Th} voltage the MOSFET requires should be applied to the V_{GS} of the device.

By virtue of the trapped charge of the floating-gate the necessary V_{Th} changes for the transistor. For an n-p-n device, where the the inversion

layer is made up from electrons that migrate away from the heavily doped n^+ regions and into the p-type substrate, the inversion layer is formed by the influence of the electric potential applied to the gate junction of the transistor. If the floating-gate of the n-p-n device if loaded with trapped electrons then the required bias on V_{GS} increases accordingly.

FGMOSFET Structure

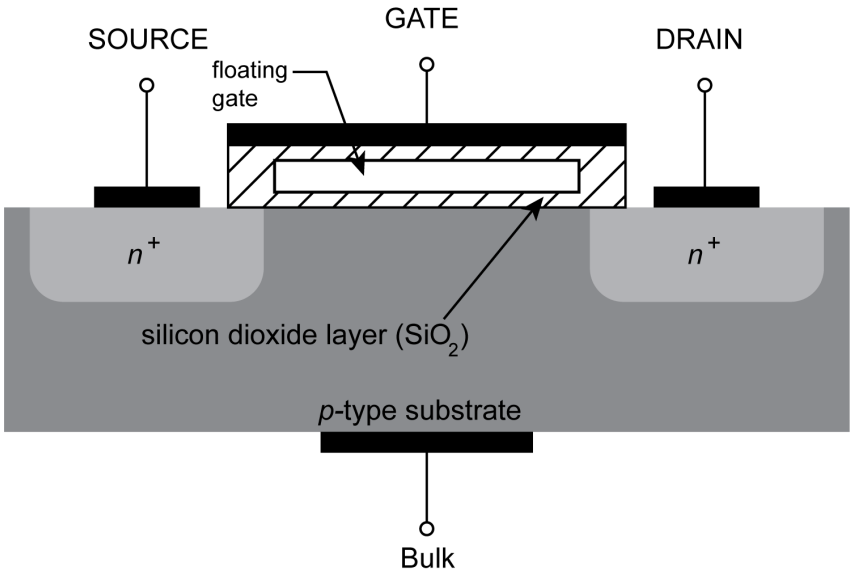

Figure 3.10: The structure of the FGMOSFET device.

The first report of a FGMOSFET was made in 1967 [82]. The first intended applications for the transistor was to store digital data in an EEPROM, EPROM, and FLASH memories. Alternative applications for the FGMOSFET started to crop up once electron tunnelling in a standard CMOS double poly was introduced [83]. With its introduction a cost effective means of building FGMOSFET devices was established and this allowed many researchers to investigate FGMOSFET concepts without requiring access to specialised fabrication processes.

Applications of the FGMOSFET

The digital application of the FGMOSFET is to use the FGMOSFET as a logic state device. If the gate of a p-type FGMOSFET is fully loaded with electrons then the necessary V_{Th} to turn on the transistor increases. This could be indicative of a logic 0, or an off state. However, if the gate is completely devoid of all trapped charge then the necessary V_{Th} to turn-on the transistor decreases. This could be indicative of a logic 1, or an on state. The ability of the FGMOSFET to store charge within its floating-gate does give it a powerful use as a logic state device. However, it is the ability of the FGMOSFET to remember its state even after the power supply to the device has been withdrawn that gives the FGMOSFET its real value as a digital competent. The FGMOSFET is a non-volatile store of a logic state. The common application of the FGMOSFET is within flash memory like that found in a USB pen drive used for data storage.

The analogue application of the FGMOSFET device is the reason why the FGMOSFET can potentially be used as a radiation measurement device. The analogue application of the FGMOSFET device looks to manipulate the stored charge trapped in the floating-gate by the influence of ionising radiation.

The claim that the FGMOSFET can be used as a radiation measurement component looks to exploit the linear relationship between exposure of ionising radiation and the measurable V_{Th} of the FGMOSFET. This linearity is a fundamental requirement for the suitability of the FGMOSFET as a radiation measuring electronic component.

3.4.3 Radiation Effect on Silicon

The broad effects of radiation on silicon are well documented elsewhere [84, 78, 85], however this selection will include a brief outline of radiation damage on silicon to help put into context the potentially detrimental consequences of silicon operating in a radiation heavy environment.

The radiation environment is a name used to categorise the expected working conditions of silicon or an integrated circuit. There are several

defined radiation environments each with their own characteristic types of radiation. Knowing the typical radiation profile of a radiation environment contextualises the application of the silicon and helps the engineer design sufficient protection into the integrated circuit to minimise the harmful and unwanted effects of the radiation. The radiation environment categories include:

- Space.
- High Energy Physics.
- Nuclear.
- Natural Environments.
- Processes Inducing Radiation.

The profile of a radiation environment can typically have either particle or photon radiation, or both.

Radiation damage to silicon will vary based on the type, energy, and intensity of the radiation itself. Generally speaking the higher the energy of an interacting photon, or the greater the mass of the interacting particle, the more destructive the effect will be to the structure of the silicon lattice. The transfer of energy from the photon interacting with the silicon depends on the energy of the photon, the trajectory of the photon, and the kinetic energy of the photon. The type of damage caused to silicon by radiation roughly falls into one of two categories: ionisation damage, and displacement damage.

Ionisation damage is damage typical of photons interacting with silicon. For lower energy X-rays the photoelectric effect is the predominant resulting effect. The photoelectric effect will cause electron-hole pair generation within the lattice due to a transfer of energy between incoming photons and an atom's orbital electrons. In silicon an interacting photo requires an energy of at least 1.1 eV at 302 K for a orbital electron to gain sufficient energy to move from the valence band to the conduction band [86]. For SiO_2 an interacting photo requires at least 8.9 eV of energy to cause an orbital electrons to

migrate from the valance band to the conduction band [87]. The significance of the band gap property to silicon based compounds is reviewed elsewhere [88].

For incoming X-ray radiation with higher energies the Compton effect is observed. In this case the absorbed photon graduates an orbital electron from the valance band to the conduction band and the residual energy from the interaction is ejected as a secondary photon. Should the secondary photon have sufficient energy it may graduate another orbital electron to the conduction band. This energy loss of incoming radiation is commonly referred to as ionisation. Incoming ionising radiation will have one of two effects on the FGMOSFET, either the cause of electron-hole pairs within the silicon dioxide region, or encourage the migration of trapped charge out of the floating-gate. When the Compton effect occurs within the SiO_2 region of the FGMOSFET electron-hole pair production occurs. This is where valence band electrons obtain sufficient energy to graduate to the conduction band.

The electron-positron pair generation is the effect resulting from interacting photons of energies greater than 1.02 MeV. In this type of pair production the photon interacts with the nucleus of the atom. Using the relationship of energy to mass, $E = mc^2$, as defined by Albert Einstein [89], the energy of the incoming photon must be sufficient to create the mass of both the electron and the positron. Any residual energy will be used as kinetic every for both particles. The high energy pair generation is described as, $\gamma \rightarrow e- + e+$.

If there is a strong electric field across the region where electron-hole pair production occurs the graduated electron will move under the field's effect. Thus the doped silicon conducts at a level higher than is normal whilst being irradiated. The positively charged holes that are also created as part of the electron-hole pair production are also mobile, but to a different degree. The production and subsequent trapping of holes in transistor cause serious degradation in transistor performance. This trapped charge alters the electrical properties of the device. To create an electron-hole pair in silicon dioxide the incoming ionising radiation must be of at least 18 eV.

Displacement damage is the damage caused by energetic particles interacting with the silicon's lattice structure. Under an event causing displace-

ment damage an incoming high energy particle will exchange energy through an elastic or inelastic collision with an atom in the silicon lattice structure. Should an incoming particle with sufficient energy collide with a silicon atom then the atom can become displaced from within the silicon lattice structure. This type of defect to the lattice is referred to as a point defect. The alteration to the silicon lattice structure caused by energetic particles is comprehensively discussed elsewhere [90]. However, it should be understood that when enough displacement events occur within the silicon lattice the structure of the compound may become irreversibly destroyed. For a MOS device extensive displacement damage will result in a compromise to the electrical characteristics of the component itself.

The use of silicon based components to measure radiation has long been practiced. Diodes, MOSFETs, and even FGMOSFET devices have all been used as dosimeters. From particle physics to space application the hardening of electronics to the harmful effects of radiation is a science onto itself. In instances where components are to act as radiation sensitive instruments the hardening of select regions of the component is necessary.

In radiotherapy the energy of the radiation beam associated with treatment is measured in electron volts (eV). The energy of the beam is approximately equal to the maximum electric potential multiplied by the charge on an electron. Thus a 1 MV beam will produce photons of no more than 1 MeV.

The range of energies a dosimeter for radiotherapy will experience is determined by the operating range of energies of the linac. To treat superficial structures (i.e. skin cancers), kilovolt X-rays are typically used and for cancers deeper within the patient megavolt energy beams are used to achieve the necessary beam penetration. The radiotherapy linac can typically operate from 100 keV to 25 MeV with beam energy seldom exceeding 1.5 MeV. As such the radiation measurement component, the FGMOSFET, needs to remain operational whilst exposed to radiation of energies from 100 keV to 25 MeV. An operational FGMOSFET used to measure the absorbed dose of ionising radiation requires the device that maintains a linear response to the uniform dose of radiation and remain sufficiently functional such that

the measured absorbed dose can be communicated to whatever logic it feeds into.

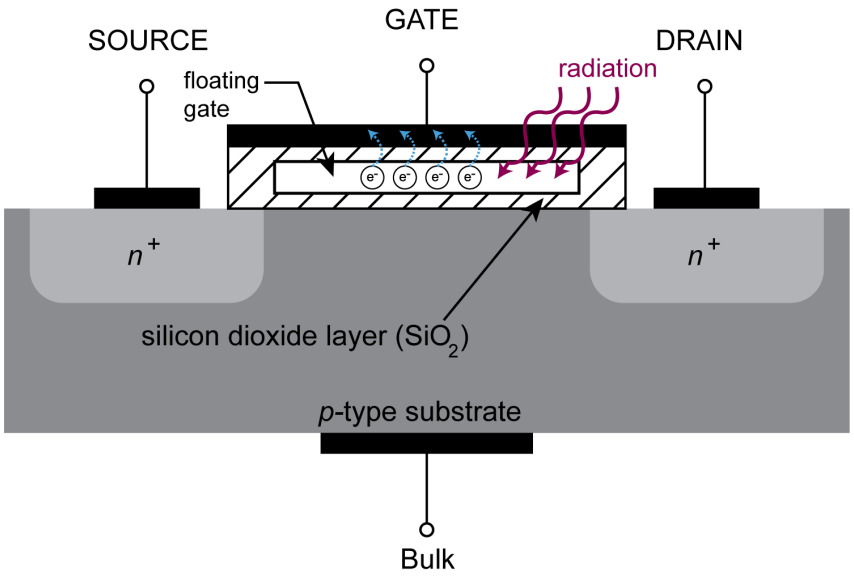

Figure 3.11: The effect of ionising radiation on trapped charge in the FGMOSFET will cause a change in charge density within the transistor's embedded floating-gate.

Assuming adequate radiation hardening is added in the custom design FGMOSFET optimised for IVD it is the only the floating-gate of the FGMOSFET that requires maximum radiation sensitivity. Figure 3.11 demonstrates how the FGMOSFET is expected to respond with exposure to ionising radiation in the radiotherapy application. From this illustration it becomes clear why it is the floating-gate of the transistor that should be the most radiation sensitive region of the entire FGMOSFET structure.

Obviously for radiotherapy with X-ray and γ-ray treatment the FGMOSFET will only ever be subject to the ionising effect of radiation and not the displacement effect caused by particle based radiation. With a well of trapped charge sitting inside the floating-gate the exchange of energy from incoming photons will energise the trapped charge such that is can escape out of the floating-gate and move towards the control-gate under the influence of the bias potential of the control-gate.

This description of how the FGMOSFET acts as a dosimeter is a description of just one method to configuring the FGMOSFET as a dosimeter. There are alternative methods [91], however the method described above is favourable for the programmable type of transistor.

3.4.4 FGMOSFET for Radiation Measurement

This section is included to provide a short summary of the major reasons why the FGMOSFET technology is prefer over other transistors for the development of a implantable dosimeter.

- Fabrication size - smaller footprint than a RADFET.
- Can be integrated onto a single circuit.
- Low manufacturing cost.
- Programmable V_{Th} - making the level of sensitivity selectable.
- Reprogrammable V_{Th} - making the device reusable.

By comparison to the RADFET, although the RADFET is more sensitive a component for the same incoming dose of ionising radiation the footprint on silicon between the RADFET and the FGMOSFET makes the FGMOSFET a favourable component. The sensitivity of the device refers to the mVGy^{-1} of the device.

Given that the FGMOSFET has a smaller physical footprint on silicon the device lends itself to an integrated circuit more naturally. The intended dosimeter for the application of radiotherapy will be designed as an implantable device, and there is an overall design goal that the entire dosimeter should not exceed a 1 mm^3 volume. As such, the smaller the radiation measurement component the more easier it will fit within the proposed dosimeter design.

With the FGMOSFET the charge density on the floating-gate can be set before the device is irradiated. The charge density on the floating-gate will determine the electric field strength the electron-hole pair are subject

to with incoming ionising radiation. The grater the charge density on the floating-gate the more probable the movement of change is at electron-hole pair production.

Reprogramming the FGMOSFET after radiation exposure offers the possibility that the transistor can be reused multiple times. In the application of an implantable dosimeter for radiotherapy it is extremely unlike the device would be reused. However, the same device would also to have use in applications where radiation measurement is continually required, and not from within a patient's tumour.

3.5 Summary

Starting with a brief summary of semiconductor physics this theory chapter has presented the necessary information to understand what effect ionising radiation has on the silicon based structure of the FGMOSFET, and how those effects from ionising radiation are measurable through changes in the electrical characteristics of the FGMOSFET undergoing exposure. Thus making the FGMOSFET a suitable electronic component to measure absorbed dose of radiation. Understanding the FGMOSFET can be used as radiation measurement component this chapter also presented the design requirements of an implantable dosimeter for radiotherapy to improve QA in treatment procedure, where the FGMOSFET as a detector would be at the centre of the design to that new device.

Chapter 4

Micro Antenna Theory

4.1 Introduction

The work completed for this thesis is towards building a new implantable dosimeter for IVD, an instrument that measures the dose of ionising radiation a cancer patient is exposed to during radiotherapy and wirelessly communicates the measured result to the medical physicist overseeing treatment delivery. To achieve this a component in the proposed dosimeter will need to be a micro antenna, an integrated antenna capable of transmitting information on a high frequency EM wave from the implanted dosimeter to the readout electronics. This theory chapter will provide the necessary information to understand the design choices made for the fabrication of a micro antenna for an implantable medical electronic device.

By starting with an overview of Maxwell's equations it can be understood how the propagation of EM waves about a surface are mathematically described. An expression for the efficiency of an antenna is presented next, where the antenna's efficiency is used as the relative performance indicator between the different micro antenna designs. This leads into a section introducing the Poynting vector, an equation that describes the direction of propagation of an EM wave. In the subsequent section, given in a mathematical form, is a general expression of the total power for all three iterations of the micro antenna design. From this general form an expression for the

radiated power, a constituent from the total power, is found. Using this information it can best be understood which portion of a current moving through a conductor is attributed to the radiated signal from the transmitting micro antenna. With the use of software for mathematical computation, Maxwell's equations were used to provide an expression for the radiated signal from the transmitting micro antenna in terms of the dimensions of the micro antenna's design. Expressions for both the single-loop and multi-loop antennas are presented in terms of the dimensions of their design and by describing the micro antenna in this way the relative efficiency of any potential micro antenna design can be predicted. This description of approximate antenna efficiency for the micro antenna leads into a section on the design dimensions and limitations for each of the three fabricated micro antenna designs. This theory chapter closes with a comparison between the predicted performance of the single-loop and multi-loop micro antenna designs, and presents their respective radiation patterns as determined through computer simulation. The predicted radiation pattern was not measured through experimentation, only the relative antenna performance at fixed distances was investigated.

All of this theory and simulation work includes the necessary steps required to obtain information about the predicted performance of the intended micro antenna design. This work was accomplished ahead of the characterisation and performance experiments completed with the fabricated micro antennas. This chapter builds on the basics of electromagnetic theory and therefore, for much of this chapter, its content is a summary of well established theoretical principles of physics that have been extensively documented elsewhere [92, 93, 94, 95].

4.2 Maxwell's Equations

The design process for a new type of micro antenna for medical electronic devices is a process completed in two stages; the first is to use a mathematical model to describe the micro antenna and simulate its performance through computer software, and the second stage is to abstract that computer model

into a physical prototype antenna through a fabrication process and evaluate the real performance of that micro antenna's design. A comparison between the results of the micro antenna's mathematical model, obtained via simulation, with the results measured from the practical characterisation is useful information to determine areas for improvement in any subsequent evaluated micro antenna designs.

It is the work completed by the 19^{th} century Scottish physicist James Clerk Maxwell that forms the basis of mathematical theory necessary to implement a computer simulation that predicts the behaviour of the designed micro antenna. In 1861 Maxwell published the first of a five paper series entitled, "On Physical Lines of Force", in the journal Philosophical Magazine [96, 97, 98, 99, 100] where he outlined a revised understanding of four mathematical equations that describe electric field and magnetic field theory. These four equations include: Gauss' law for an electric field, Gauss' law for a magnetic field, Farady's law, and the Ampère-Maxwell law.

$$\oint_S \vec{E} \cdot \hat{n} \, \mathrm{d}a = \frac{q_{enc}}{\varepsilon_0} \tag{4.1}$$

$$\oint_S \vec{B} \cdot \hat{n} \, \mathrm{d}a = 0 \tag{4.2}$$

$$\oint_C \vec{E} \cdot \mathrm{d}\hat{l} = -\frac{\mathrm{d}}{\mathrm{d}t} \int_S \vec{B} \cdot \hat{n} \, \mathrm{d}a \tag{4.3}$$

$$\oint_C \vec{B} \cdot \mathrm{d}\hat{l} = \mu_0 \left(I_{enc} + \varepsilon_0 \, \frac{\mathrm{d}}{\mathrm{d}t} \int_S \vec{E} \cdot \hat{n} \, \mathrm{d}a \right) \tag{4.4}$$

The permittivity of free space is given the term, ε_0, where the permittivity is a measure of a material's ability to permit an electric field. The unit of measurement for permittivity is farads per metre (Fm^{-1}). $\varepsilon_0 = 8.8542 \times 10^{-12}$ Fm^{-1}. The permeability of free space is given the term, μ_0, where permeability is a measure of a material's ability to permit a magnetic field. The unit of measurement for permeability is Henry per metre (Hm^{-1}). $\mu_0 = 1.2566 \times 10^{-6}$ Hm^{-1}.

Gauss' law for electric fields is described in the integral form in Equa-

tion 4.1. The left side of the equation, $\oint_S \vec{E} \cdot \hat{n}\ \mathrm{d}a$, describes the number of field lines passing through a closed surface (S), otherwise referred to as the electric flux. The right side of the equation, $\frac{q_{enc}}{\varepsilon_0}$, describes the total amount of charge contained within S divided by the permittivity of free space, ε_0. Gauss' law for electric fields describes the relationship between an electric field and the electric charges that cause the electric field.

Gauss' law for magnetic fields is described in the integral form in Equation 4.2. The left side of the equation, $\oint_S \vec{B} \cdot \hat{n}\ \mathrm{d}a$, describes the number of field lines passing through a closed surface (S), otherwise referred to as the magnetic flux. The right side of the equation is 0. Gauss' law for magnetic fields describes the magnetic field as it is generated by a magnetic dipole and because there is no such thing as a magnetic monopole the total magnetic flux passing through S is 0.

Farady's law is described in the integral form in Equation 4.3. The left side of the equation, $\oint_C \vec{E} \cdot \mathrm{d}\hat{l}$, describes the circulation of the electric field around the closed path, C. The right side of the equation, $-\frac{\mathrm{d}}{\mathrm{d}t}\int_S \vec{B} \cdot \hat{n}\ \mathrm{d}a$, describes the rate of change with time of the magnetic flux through any surface bound by C. Faraday's law shows how a changing magnetic field creates an electric field.

The Ampère-Maxwell law is described in the integral form in Equation 4.4. The left side of the equation, $\oint_C \vec{B} \cdot \mathrm{d}\hat{l}$, describes the circulation of the magnetic field around the closed path, C. The right side of the equation, $\mu_0 \left(I_{enc} + \varepsilon_0 \frac{\mathrm{d}}{\mathrm{d}t}\int_S \vec{E} \cdot \hat{n}\ \mathrm{d}a \right)$, is the sum of two sources for the magnetic field: I_{enc}, a steady conduction current, and $\frac{\mathrm{d}}{\mathrm{d}t}\int_S \vec{E} \cdot \hat{n}\ \mathrm{d}a$, the rate of change with time of the electric flux through any surface bound by C. The right side of the equation therefore describes the changing electric flux through any S bound by C. The Ampère-Maxwell law shows how a magnetic field can be created by either an electrical current or by a changing electric field.

$$\nabla^2 \vec{E} = \mu_0 \varepsilon_0 \frac{\partial^2 \vec{E}}{\partial t^2} \tag{4.5}$$

$$\nabla^2 \vec{B} = \mu_0 \varepsilon_0 \frac{\partial^2 \vec{B}}{\partial t^2} \tag{4.6}$$

Collectively this set of equations, the four revised mathematical equations that describe electric field and magnetic field theory (Equations: 4.1, 4.2, 4.3, and 4.4), are referred to as Maxwell's equations and form the basis of the branch of physics known as classical electromagnetism. Using these equations Maxwell deduced the relationship between the electric field and the magnetic field and eventually derived the EM wave equation as published in the 1865 paper, "A Dynamical Theory of the Electromagnetic Field", in which Maxwell also became the first physicist to propose the idea of light as an EM wave [101]. The EM wave equations are defined in Equation 4.5 for the electric field and Equation 4.6 for the magnetic field, and both equations are second order partial differential equations that describe the propagation of EM waves through a vacuum. ∇^2 is the vector Laplace operator, or a differential operator defined over a vector field. $\nabla^2\vec{E}$ and $\nabla^2\vec{B}$ from the left side of both equations describe, respectively, the second derivative of the vector electric field over space and the second derivative of the vector magnetic field over space. $\frac{\partial^2\vec{E}}{\partial t^2}$ and $\frac{\partial^2\vec{B}}{\partial t^2}$ from the right side of both equations describe, respectively, the second derivative of the vector electric field and the second derivative of the vector magnetic field.

4.3 Antenna Efficiency

An EM wave is a wave that takes place in the EM field. All EM waves consist of both an electric and magnetic component. Both the electric and magnetic field oscillate in-phase perpendicular to each other perpetuating the motion of the wave, and perpendicular to the direction of the wave's propagation. EM waves travel at the speed of light, $c \approx 3 \times 10^8$ ms^{-1}.

$$\eta = \frac{R_{rad}}{R_{rad} + R_{loss}} \tag{4.7}$$

The efficiency is given the symbol, η. For the design of a micro antenna in the transmission of EM waves the efficiency is described by Equation 4.7. The micro antenna efficiency is defined as the ratio between the radiation resistance (R_{rad}) and the loss resistance (R_{loss}), where R_{rad} represents the

portion of the signal that is transmitted from the micro antenna and R_{loss} accounts for the remainder of signal that is dissipated through the resistance of the conductor [102, 103]. Both R_{rad} and R_{loss} are a measure of resistance, and therefore their SI unit is the Ohm (Ω).

In the design of a micro antenna for the application of implantable medical electronic devices it is imperative to optimise the efficiency of the micro antenna as a transmitting antenna by reducing the R_{loss} component of the signal through the conductor.

4.4 The Poynting Vector

$$\vec{S} = \vec{E} \times \vec{B} \tag{4.8}$$

In 1884 the English physicist John Henry Poynting published a paper that described how the direction and magnitude of an EM wave is based on the conservation of electric and magnetic fields [104], and thus predicted the existence of what are known as plane waves in classical physics. EM waves are plane waves. The conservation of the energy for the EM wave is mathematically described by Equation 4.8 and is referred to as the Poynting vector. The SI unit for the Poynting vector is the power density (Wm^{-2}) thus making the Poynting vector an expression for the instantaneous flow of power per unit area. $\vec{S}$ denotes the direction of power flow per unit area for an EM wave, $\vec{E}$ is the electric field, and $\vec{H}$ is the magnetic field.

$$\vec{S} = \frac{1}{2}(\vec{E} \times \vec{B}^{*}) \tag{4.9}$$

An expression for the complex power density for the far field is mathematically described by Equation 4.9 [105], and is an amended form of the Poynting vector to describe the radiated field by a magnetic dipole antenna. The $*$ in the magnetic field expression, $\vec{B}^{*}$, denotes the complex conjugate. The complex conjugate of a complex number refers to the expression of that complex number as having the same real component, but with an imaginary component of equal magnitude and opposite sign. The loop antenna is a magnetic dipole antenna. The total power radiated by the current carrying

loop is found by integrating Equation 4.9 over a large spherical radius, from distances r through to ∞, and is therefore a measure of the total radiated power through the far field region of EM radiation.

$$P_f = \frac{1}{2} \oiint_s (\vec{E} \times \vec{B}^*) \cdot d\vec{s} \tag{4.10}$$

The complex power flow through a closed surface is expressed in Equation 4.10, where $d\vec{s} = ds\hat{\vec{n}}$ and $\hat{\vec{n}}$ is the unit normal to the surface directed out from the surface. The integral of the complex Poynting vector over a closed surface, s, gives the total complex power flowing out through the surface s. If the complex Poynting vector represents the complex power density (Wm^{-2}) at a point then the complex power through any surface s (not necessarily a closed surface) can be found by integrating the complex Poynting vector over that surface [106].

4.5 Loop Antenna's Radiated Power

Maxwell's equations can be used to mathematically describe the propagation of EM waves about a surface. In the case of micro antenna design Maxwell's equations were analytically solved to determine an expression for the corresponding electric field, $\vec{E}$, and the magnetic field, $\vec{B}$, for a particular micro antenna design. For each design of micro antenna the analytical solution considered the micro antenna's shape assuming EM radiation through free space. Other relevant physical effects for micro antenna design were neglected in this analysis, including: losses due to substrate coupling, eddy currents, resistance, and influence of the contacts [107].

The Poynting vector defined in Equation 4.8 can be thought of as representing the energy flux which is the rate of flow of energy ($\mathrm{Jm^{-2}s^{-1}}$) of the EM field. The complex power density vector defined in Equation 4.9 is used to determine the far field energy flux of the normal component (at 90°) of the Poynting vector over a surface at a radius r where the far field extends to infinity. The total complex power, P_{total}, flowing through a spherical surface at radius r was obtained by integrating the normal component of $\vec{S}$ over this

surface.

$$P_{total} = A_1 + \frac{A_2}{r^2} + j\frac{A_3}{r^3} \tag{4.11}$$

From the antenna layout an algebraic expression for the vector potential ($\vec{A}$) in space, as a function of the geometry and current, was obtained. Next, from Maxwells equations, the corresponding expressions for $\vec{E}$ and $\vec{B}$ were calculated. From these latter expressions a formula for the Poynting vector as a function of the driving current through the micro antenna was obtained. For the third antenna layout, the multi-loop micro antenna, the total expression of the Poynting vector was obtained by summing the Poyinting vectors corresponding to each single nested loop. The angular dependency of the far field was obtained from the normal component of the Poynting vector over a surface of radius, r, in the limit to infinite distance. Carrying out the integration for all three micro antenna designs, a general expression for the total complex power for the micro antenna design is expressed in Equation 4.11. A_1 and A_2 from the right side of Equation 4.11 represent the radiation resistance, R_{rad}, or the portion of the signal that is transmitted from the micro antenna. A_3 from the right side of Equation 4.11 represents the stored energy in the near field, the reactive power. However, only the A_1 term from Equation 4.11 represents the radiated power from r to infinity and is therefore the only term that can be used to approximate R_{rad} for the micro antenna design. R_{rad} is found by equating the radiated power (P_{rad}) at infinity to the power dissipated by a resistor, assuming $I_0 = 1$ A, as shown in Equation 4.12 and Equation 4.13.

$$P_{rad} = A_1 = \frac{1}{2}R_{rad}I_0^2 \tag{4.12}$$

$$R_{rad} = 2A_1 \tag{4.13}$$

In the following two subsections an expression for R_{rad} for both the single-loop and multi-loop micro antenna is outlined based on the dimensions of the micro antenna's design. With a mathematical expression of R_{rad} for a

micro antenna's design the subsequent calculation of the micro antenna's P_{rad} and η becomes straightforward. It is from this arrangement that only small changes are required to the computer model of a micro antenna's design to predict the expected efficiency of that micro antenna.

It should be noted that for the following two subsections, Section 4.7.1 and Section 4.7.2, there is an expression for the single-loop, Equation 4.14, and multi-loop, Equation 4.15, micro antenna. Each of these two equations is based on a mathematical description of the wire trace the micro antenna makes around the circuit. A straight line is the simplest trace upon which to integrate to find the complex power flow through a surface of the micro antenna's wire trace. As such, both Equation 4.14 and Equation 4.15 are described as the sum of their individual sides.

4.5.1 Single-Loop Design

From the mathematically deduced approximation of R_{rad} in Equation 4.12 the single-loop micro antenna radiation resistance is expressed as:

$$\begin{aligned} R_{rad} =& \frac{10}{60}\frac{\Delta L k^3}{\pi\varepsilon\omega}\left[\left(1+\frac{1}{10}k^2\Delta L^2\right)B^2\right. \\ &\left.+\left(-2+\frac{3}{10}k^2\Delta L^2\right)B+\left(1+\frac{6}{10}k^2\Delta L^2\right)\right] \end{aligned} \tag{4.14}$$

Where the terms in Equation 4.14 include: $\Delta L = L - W$, the difference between the antenna side length (L) and the track width (W), $k = \frac{2\pi}{\lambda}$, the wave vector, and $B = \frac{\Delta L - G}{\Delta L}$, the size of the gap ($G$) between the contact pads.

4.5.2 Multi-Loop Design

From the mathematically deduced approximation of R_{rad} in Equation 4.12 the multi-loop micro antenna radiation resistance is expressed as:

$$R_{rad} = M_1N^5 + M_2N^4 + M_3N^3 + M_4N^2 + M_5N \tag{4.15}$$

The coefficients of the terms in Equation 4.15 include:

$$M_1 = \frac{8a^4k^5}{15\pi\omega\varepsilon}$$

$$M_2 = \frac{a^4k^5}{3\pi\omega\varepsilon}\left(\frac{7}{2} + 4a^{-1}\Delta L\right)$$

$$M_3 = \frac{a^4k^5}{3\pi\omega\varepsilon}\left(\frac{53}{30} + 7a^{-1}\Delta L + 4a^{-2}\Delta L^2\right)$$

$$M_4 = \frac{a^4k^5}{3\pi\omega\varepsilon}\left(-\frac{7}{20} + \frac{53}{20}a^{-1}\Delta L + \frac{21}{4}a^{-2}\Delta L^2 + 2a^{-3}\Delta L^3\right)$$

$$M_5 = \frac{a^4k^5}{3\pi\omega\varepsilon}\left(-\frac{13}{60} - \frac{7}{20}a^{-1}\Delta L + \frac{53}{40}a^{-2}\Delta L^2 + \frac{7}{4}a^{-3}\Delta L^3 + \frac{1}{3}a^{-2}k^{-2}\right)$$

Where a is the gap between nested tracks (S) of the multi-loop antenna design. The expression found in Equation 4.15 indicates that the R_{rad} increases with the number of loops in the multi-loop design. However, as the number of loops increase so too does R_{loss} due to the increase in track length, thus causing an overall reduction in the efficiency of the micro antenna. The optimum performance indicator of the efficiency of the micro antenna's design is where R_{rad} is larger compared to R_{loss}.

4.6 Micro Antenna Design

EM waves are produced by the acceleration of charge through a conductor. The change of velocity by the moving charge will induce the propagation of a magnetic field and that will, in turn, induce the propagation of an electric field and so on. Thus EM radiation is created. That is to say a conductor that has an alternating current passing through it will emit EM radiation at the same frequency as the alternating current's oscillations. It is under this principle that the transmitting antenna can be used for communication. The receiving antenna operates in the reverse of this principle, assuming the

receiver antenna is orientated in the same direction as the polarised wave. The incoming EM wave will encourage the movement of charge within the antenna at the same frequency as the wave itself. By tuning a capacitor in an LC tank circuit, an efficient transfer of energy will be achieved between the incoming EM wave and the charges within the antenna's conductor.

Presented in the sections that follow are the dimensions of all three types of micro antenna design that were investigated. The practical characterisation was completed for the current batch of fabricated micro antennas before a subsequent batch of micro antennas was produced. It was due to this sequential approach to antenna design that the results from the current batch of micro antennas could be interpreted before the fabrication of any subsequent antenna design. Thus the next batch of micro antennas included favourable amendments to its design based on the data provided by the last batch of micro antennas. The chosen dimensions for all three batches of fabricated micro antennas was therefore based on the combination of simulation results and practical characterisation results.

4.6.1 First Batch: Single-Loop

Figure 4.1 shows the chosen dimensions for the first batch of micro antennas and is a single-loop design. The design and fabrication of this first micro antenna was very much a learning process. The simulated results were compared to the practically measured characteristics of the design. Using the results obtained in the design, fabrication, and characterisation of this first batch of micro antennas the assessment of each stage of the antenna design evaluation process was recognised. Thus a better understanding of processes, and errors to processes, for each stage of antenna evaluation was avoided in subsequent evaluated batches of micro antennas. Notice in Figure 4.1 the dimensions included are: the track width (W), the length of one side (L), and the gap between the contact pads (G). These were the major dimension parameters that could be altered between fabrication batches.

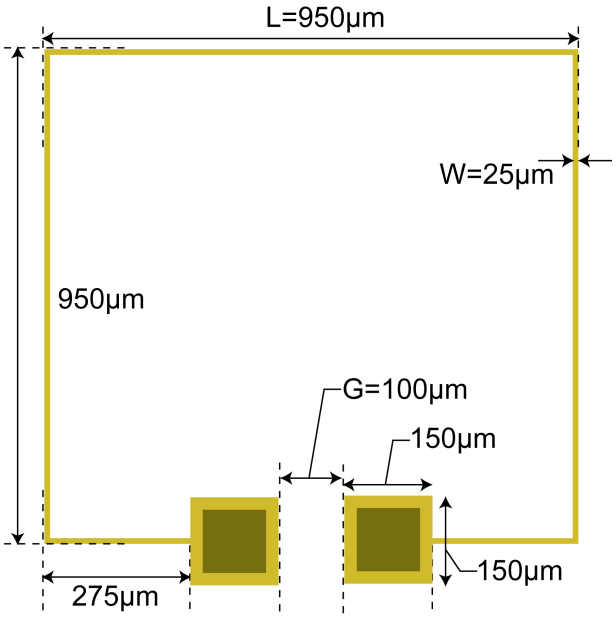

Figure 4.1: Batch 1 micro antenna dimensions.

4.6.2 Second Batch: Single-Loop

By the second batch of fabricated micro antennas, a couple of revisions were made to the dimensions of the single-loop design over the design to the first batch and those revisions are illustrated in Figure 4.2. The micro antenna's shape in the second batch was altered to help improve its performance over the performance of the first batch of micro antennas. Those revisions to the antenna's dimensions included increasing both W and G. From the expression in Equation 4.14 the R_{rad} attribute of the micro antenna can be resolved for both the W and G dimensions. The simulation data therefore suggested these revisions would produce an improvement to antenna performance based on the calculated antenna efficiency.

4.6.3 Third Batch: Multi-Loop

The third batch of micro antennas was a multi-loop design and the dimensions of this design are presented in Figure 4.3. Unlike the single-loop design of the previous two fabricated batches it was the ambition of the work com-

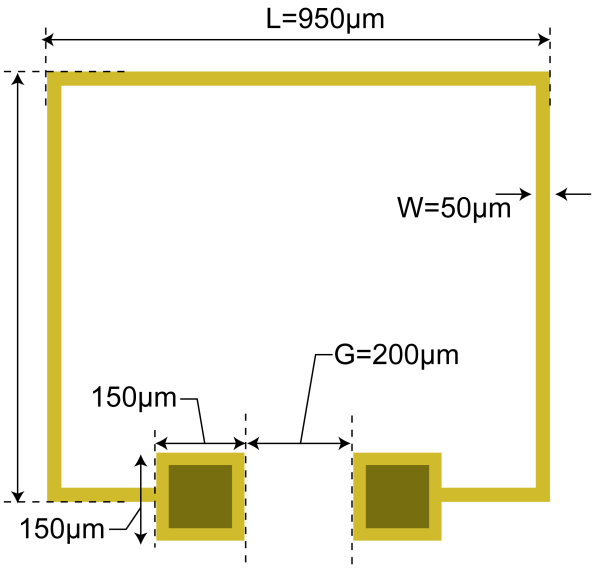

Figure 4.2: Batch 2 micro antenna dimensions.

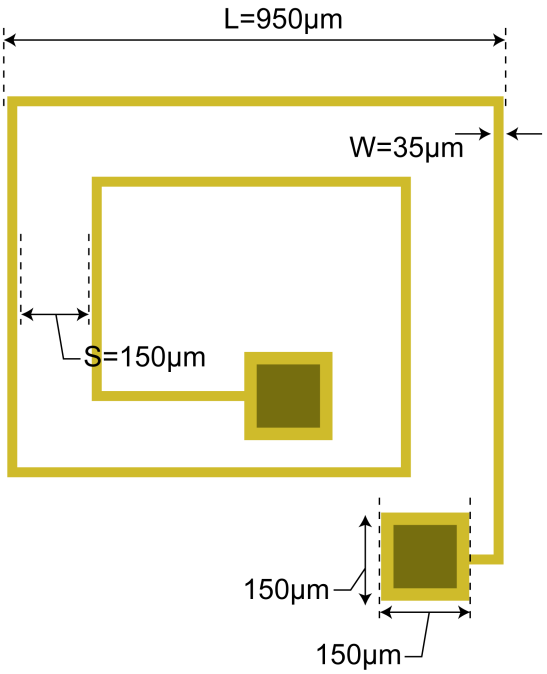

Figure 4.3: Batch 3 micro antenna dimensions.

pleted for the third batch of micro antennas to determine the performance of the multi-loop design. With data on both the single-loop and the multi-loop design a performance comparison between the two design approaches can be made from the data gathered in the experiment.

4.6.4 Fabrication Limitations

In the design of the micro antenna, for both the single-loop and multi-loop design, there were some dimensions to the micro antenna that could be adjusted to improve the predicted efficiency of the micro antenna. These dimensions included the track width (W), the number of loops (N), the gap between the contact pads (G), and the spacing between the loops (S). However, due to the technical characteristics of the available fabrication process the depth (or thickness) of the track was fixed at 0.5 μm. Before the fabrication of any micro antennas began it was assumed that these dimensions were the only adjustable parameters in the design of the micro antenna that would improve the real-world performance of the micro antenna.

Due to the time constraints and costs involved in the fabrication of the micro antennas a subsequent batch of micro antennas was only fabricated after completing the performance analysis and characterisation of the current batch of micro antennas. It was because of this iterative approach to the fabrication of the micro antennas that it was discovered that the track exposure was an additional adjustable dimension to the micro antenna design that would alter the real-world performance of the micro antenna. Track exposure refers to the upper surface of the track on a circuit being exposed to the natural surrounding environment. In this case the track exposure left the wire trace of the micro antenna exposed to air. As such, for the second and third batches of micro antennas, the micro antenna track was embedded within a silicon dioxide layer to keep the track from oxidising and thus altering its conductive properties and making the conductivity more predictable. This is the difference between the theory and practical implementation of antenna design and it was fortunate that the experiment proceeded in stages based on the sequential fabrication of batch iterations, otherwise this study might

never have accommodated the need to refine micro antenna design including the track exposure.

4.7 Micro Antenna Simulations

Having an understanding of the mathematics for micro antenna simulation for both single-loop and multi-loop antennas, and knowing the dimension of the micro antenna being simulated, the performance of the micro antenna as a transmitting antenna can be simulated by computer software. For the calculation of R_{rad} and the plots presented in Figure 4.4 and Figure 4.5 the Maple 14 software simulation package was used. Maple 14 is a general purpose commercial mathematics software. For the single-loop micro antenna design Equation 4.14 formed the bases on the Maple 14 simulation, and for the multi-loop micro antenna design Equation 4.15 was used in the Maple 14 simulation package. Figure 4.4 is the polar plot and radiation pattern for the first batch of micro antennas. It is therefore the lesser refined design revision, between the design of the first and second batches, of the single-loop micro antenna. The second batch of single-loop micro antenna was predicted to outperform the first batch of micro antennas. As Figure 4.5 is an illustration of both the polar plot and radiation pattern of the multi-loop micro antenna design, it is therefore the simulated behaviour of the micro antenna from the third batch of fabricated micro antennas. The third batch of micro antennas was predicted to out perform the first batch of micro antennas.

In this section the typical results from a micro antenna simulation are presented for both the single-loop and multi-loop design. The dimensions for each fabricated batch of micro antennas was, in part, chosen based on the results of the micro antenna simulations.

For a transmitting antenna the energy radiated from the antenna forms an EM field and for the loop antenna design the EM field is not equal in all directions. The EM field a transmitting antenna forms can be described by its radiation pattern and polar plot. The radiation pattern and polar plot for both the single-loop and multi-loop antenna is found using simulation software. The radiation pattern and polar plot describe the propagation of

the antenna's transmitting EM wave for the far field of operation, where the boundary of both plots is from the micro antenna up to a distance at infinity. The axis of measurement in both plots is therefore the power (W) of the measured signal as a function of distance. $r = \infty, P_{Rad} = 1$ pW.

4.7.1 Single-Loop Design

Simulating the single-loop micro antenna design produced the two plots, presented in Figure 4.4, that describe the radiation pattern of the emitted EM energy from the transmitting micro antenna. The dimensions used to produce the plots in Figure 4.4 were taken from the second batch of micro antennas.

4.7.2 Multi-Loop Design

Simulating the multi-loop micro antenna design produced the two plots presented in Figure 4.5 which describes the radiation pattern of the emitted EM energy from the transmitting micro antenna. The dimensions used to produce the plots in Figure 4.5 were taken from the third batch of micro antennas.

4.7.3 Antenna Efficiency

Batch No.	G (μm)	W (μm)	N	η
2	200	50	1	14.0×10^{-6}
3	200	35	2	9.40×10^{-6}
1	100	25	1	1.70×10^{-6}

Table 4.1: Predicted relative performance of micro antenna design.

Table 4.1 is a summary of the relative performance of all three micro antenna designs. G, W, and N are physical dimensions to the micro antenna design. As illustrated in Figure 4.1, Figure 4.2, and Figure 4.3 the G dimension is the separation of the track pads, W is the track width, and N

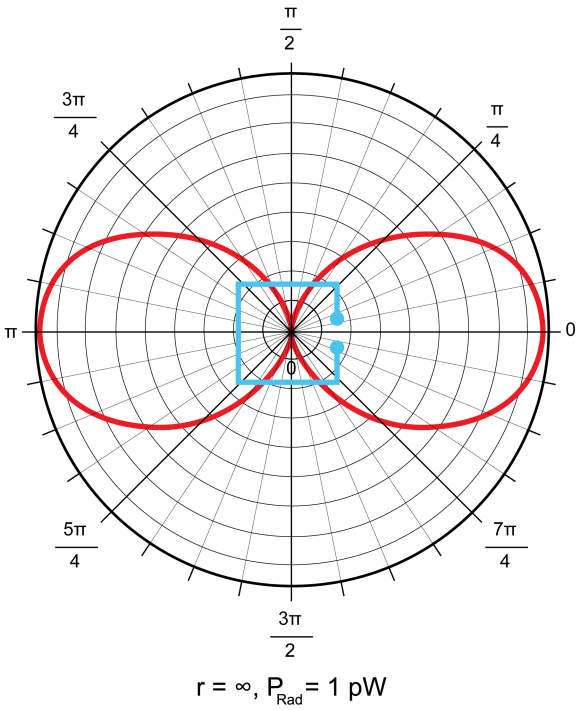

(a) Single-loop polar plot.

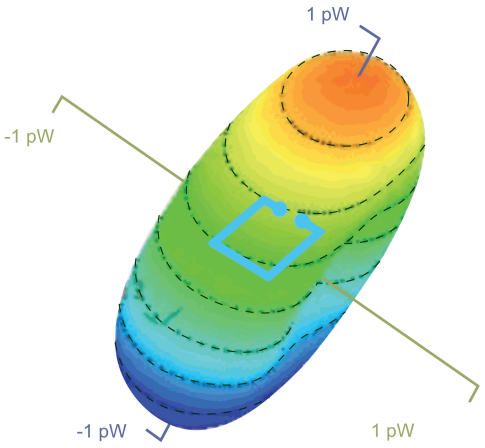

(b) Single-loop radiation pattern.

Figure 4.4: Understanding the EM wave energy as it radiates away from the transmitting micro antenna. Figure 4.4(a) shows the polar plot. Figure 4.4(b) shows the radiation pattern for the single-loop micro antenna design.

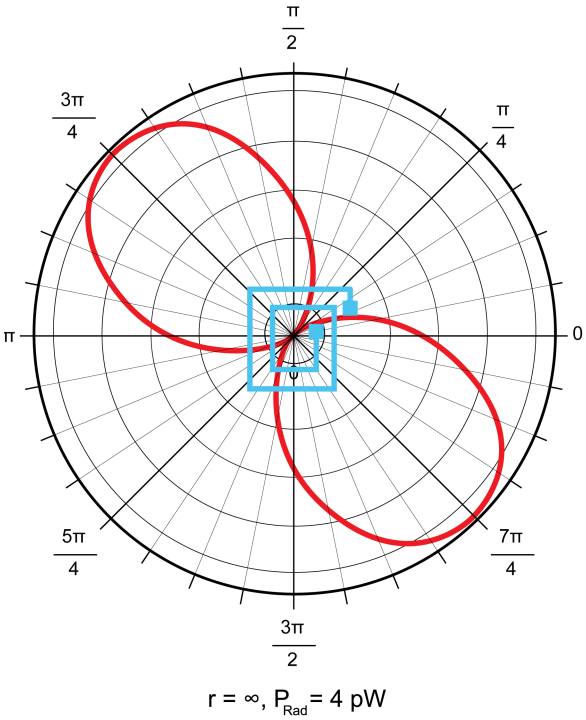

(a) Multi-loop polar plot.

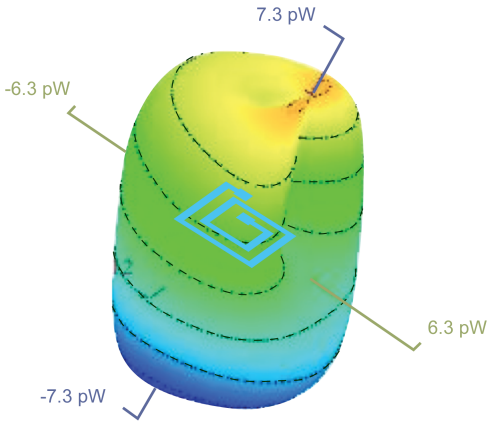

(b) Multi-loop radiation pattern.

Figure 4.5: Understanding the EM wave energy as it radiates away from the transmitting micro antenna. Figure 4.5(a) shows the polar plot. Figure 4.5(b) shows the radiation pattern for the multi-loop micro antenna design.

is the number of loops in the antenna's design. The oder of the three micro antenna designs in Table 4.1 is by the fourth characteristic of the micro antenna, the predicted efficiency, η. It should be noted that the dimension for the separation of tracks for concentric loops, S, has not been listed. This dimension is only applicable to the design of batch number three, and listed below.

The estimated efficiency for the first batch of micro antennas with $G = 100$ μm and $W = 25$ μm, was $\eta = 1.70 \times 10^{-6}$. With the revisions to the dimensions of the second batch of micro antennas, $G = 200$ μm and $W = 50$ μm, then the estimated efficiency was found to be $\eta = 14.0 \times 10^{-6}$. According to this simulation work the predicted efficiency of the single-loop micro antenna design is improved by increasing the track width and increasing the gap between the contact pads. The increase in antenna efficiency caused by increasing the track width is due to a reduction in ohmic losses through the track. The increase in antenna efficiency caused by increasing the gap between the contact pads is thought to be a consequence of a reduction in phase cancellation of the EM waves generated by the parallel tracks of the loop.

The estimated efficiency for the third batch of micro antennas was a more involved calculation as it is based on a multi-loop micro antenna design. The optimum efficiency for the multi-loop micro antenna was found by calculating the estimated efficiency for an increasing number of loops (N), where an increasing number of loops would improve the magnetic flux of the micro antenna but also increase the ohmic losses through the track as the track increased in overall length. It was found for $N = 2$, $S = 125$ μm, and $W = 35$ μm that $\eta = 9.40 \times 10^{-6}$. It was therefore expected that the order of relative performance between all three different designs of micro antenna would be; the second batch of single-loop micro antennas as the best performing, the third batch of multi-loop micro antennas as the second best performing, and the poorest performing micro antenna would be the first batch of micro antennas.

Referring back to Equation 4.7 it is clear that the efficiency, η, of a micro antenna is characterised by the ratio between the radiation resistance (R_{rad})

and the loss resistance (R_{loss} of the micro antenna. As η is a ratio it is without a unit. This measure of efficiency is comparable amongst the there micro antenna designs only. The expected performance of the micro antenna was measured experimentally, and the results of that work are presented in Chapter 6. As the micro antenna efficiency is ratio the simulation work completed to obtain η for each micro antenna design, and thus predict the performance of the micro antenna, was only done to indicate an expected performance improvement relative to each micro antenna design. To measure the degree of performance improvement between each of the three micro antenna designs experimental lab work was completed.

4.8 Summary

Starting with a brief summary of Maxwell's equations it was quickly shown in this chapter how, through Poynting vector analysis, the relative predicted efficiency of the micro antenna design was calculate based on the dimensions of the micro antenna's design. Included in this chapter is the necessary theory to understand the design choices made in the design of the micro antenna. The work completed in this chapter was necessary to describe the predicted performance of the intended micro antenna design, and was accomplished ahead of the characterisation and performance experiments completed with the fabricated micro antennas.

Chapter 5

Transistor Experiment and Results

5.1 Introduction

This is a results chapter and the data presented within this chapter make a credible academic contribution to the field of IVD for radiotherapy. The results discussed in this chapter have undergone peer review and been published in the Journal of Instrumentation [108].

This chapter will begin with a quick overview of the expected working environment for a medical instrument operating during the course of a radiotherapy treatment. An overview of this working environment will contextualise the aims and objectives of this study. For an electronic dosimeter for radiotherapy there will need to be an electronic component capable of measuring radiation. This chapter presents the work and results of a study that investigated the suitability of the FGMOSFET as the electronic component capable of measuring the absorbed dose of ionising radiation as typically delivered to a patient in the field of medical radiotherapy. The chapter will provide a detailed report on every stage to the FGMOSFET experiment should there be a need to replicate the results found.

5.2 The Operating Environment

The gray is the SI unit used to quantify the absorbed dose of ionising radiation. The gray is defined as the absorption of one joule of ionising radiation by one kilogram of matter, human tissue, where 1 eV is equivalent to 1.602×10^{-19} J. The gray is given the symbol Gy. It is the unit used in the context of radiotherapy to describe the quantity of intended dose of ionising radiation a patient has been prescribed. The delivery of a patient's treatment is typically split up over several fractions and, depending on the type and location of the cancer, the dose of ionising radiation is chosen. A treatment dose seldom exceeds 80 Gy.

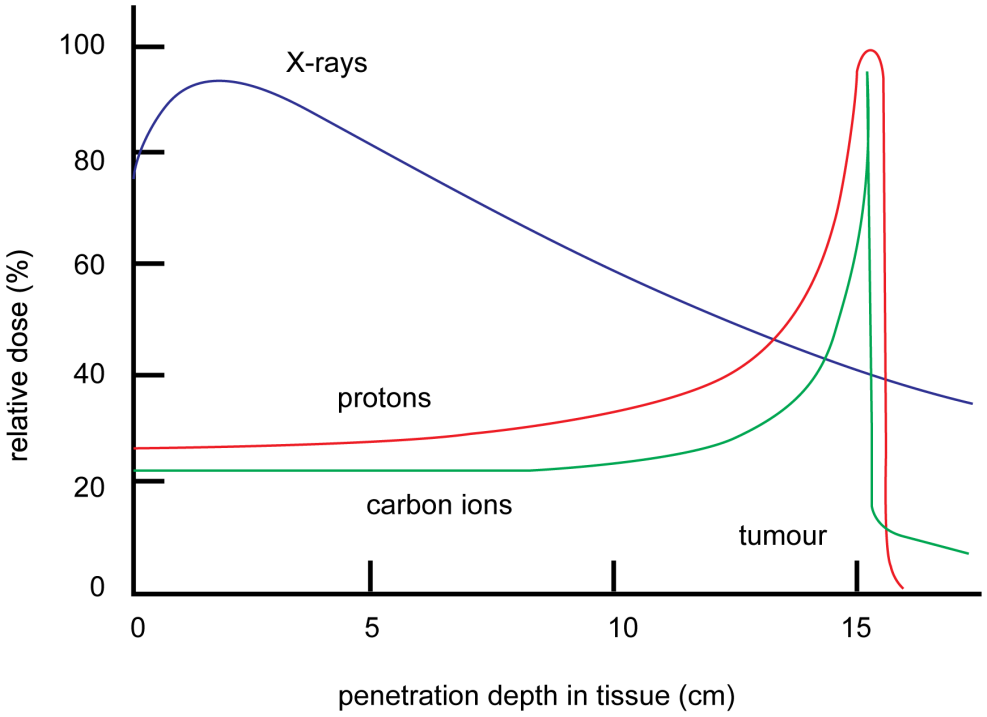

Figure 5.1: Profile of absorbed dose of ionising radiation in human tissue [109].

Although the medical physicist will configure the linac beam energy, a patient's treatment is still characterised by a unit of absorbed dose of ionising radiation. To understand this point take a moment to study Figure 5.1 [109].

Radiotherapy is the process of using ionising radiation to kill cells. Radiotherapy is a treatment where the radiation source is outside the patient, and brachytherapy is the name given to a treatment where the radiation source is placed within the patient. The radiation beam of EBRT can be anything from high energy photons including X-rays and γ-rays, to accelerated particles including electrons, protons, and carbon ions.

Figure 5.1 shows how the absorbed dose changes as the radiation beam passes through the patient's body. The origin of the x-axis in Figure 5.1 is the point where the patient tissue begins. Depending on the type of beam the absorbed dose profile will vary. It is not the energy of the beam that will determine the dose profile, and ultimately what portion of the beam's dose has reached the target volume, but it is the beam type that determines what portion of the beam's dose that has reached the target volume.

It is important to note that this absorbed dose profile does not describe the photons/particles as losing energy. On the contrary, only an energy exchange with interacting atoms will result in a loss of energy to the photons/particles of the radiation beam. However, what the absorbed dose profile does describe is how protons, photons, and carbon ions are delivered to the tumour. The dose deposited by protons remains relatively constant as they travel through the normal tissues towards the the target volume. The kinetic energy of the protons is transferred to the tumour by electrons knocked out of atoms. These electrons ionise DNA, and their biological effective resembles that of MV photons [110]. At the target volume there is a sharp rise in the dose deposited by the proton particle. This peak in the plot shown in Figure 5.1, and is referred to as the Bragg peak. Both protons and carbon ions exhibit a Bragg peak. Thus, the biological effectiveness of the particle based beam sharply increases at the target volume [110]. The Bragg peak is a result of elastic scattering.

By contrast, for photon based dose profile, i.e. for X-ray based radiotherapy, the dose profile in Figure 5.1 shows an exponential decrease in the transmitted intensity with increasing depth is due to absorption. From a photon beam the absorbed dose of radiation at the target volume is only a fraction of the overall dose. It is because of this characteristic of the X-ray

radiation beam that the treatment with X-ray radiation is delivered such that the sum of the absorbed dose at the target volume meets the required absorbed dose per fraction. That is why a modern gantry for X-ray based treatment must move around the patient to deliver a portion of the treatment dose from multiple directions.

By contrast the absorbed dose of high energy particles tend to peak at a distances from the source. That is, the number of beam particles interacting with atoms is greatest at a distance from the source. The linac producing the beam of high energy particles can manipulate the beam such that the Bragg peak of absorbed dose occurs at a predetermined distance from the source. Despite this seemingly advantageous characteristic of the treatment, using a particle based radiation beam the dose is still delivered with a rotating gantry. A rotating gantry delivering partial dose from multiple angles will minimise the collateral damage to healthy cells surrounding the target volume.

$$-\frac{dE}{dx} = \frac{4\pi}{m_e c^2} \cdot \frac{nz^2}{\beta^2} \cdot \left(\frac{e^2}{4\pi\varepsilon_0}\right)^2 \cdot \left[\ln\left(\frac{2m_e c^2\beta^2}{I \cdot (1-\beta^2)}\right) - \beta^2\right] \tag{5.1}$$

Equation 5.1 is a mathematical expression for charged particles as they move through matter, and how they interact with the electrons of atoms in that material [111]. Equation 5.1 is the Bethe formula. v is the velocity of a particle, c is the speed of light, $\beta = {}^{v}/_{c}$, E is the energy of a particle, x is the distance travelled by a particle, z is the particle charge, e is the charge of the electron, m_e is the rest mass of the electron, n is the electron density of the target, I is the mean excitation potential of the target, and ε_0 is the vacuum permittivity. The Bethe formula describes the energy loss per distance travelled of charged particles travelling thorough matter.

5.3 Experiment Aims and Objectives

This study was to determine the suitability of the FGMOSFET as a radiation measurement component that can be used in medical radiotherapy. The intended instrument the FGMOSFET will be used with is an implantable

dosimeter. A dosimeter providing a real-time measurement of the absorbed dose during a patient's treatment will improve the confidence of both doctors and patients in a potentially lethal procedure. An implantable dosimeter works to improve the QA of radiotherapy by measuring the absorbed dose during treatment delivery for that fraction and any discrepancy between the absorbed dose and the intended dose will alert the medical physicist of the treatment error. In order for the FGMOSFET to work in this application it should be a cost effective low power active component capable of accurately measuring the absorbed dose of ionising radiation with energies typical of cancer treatment.

5.3.1 Operational Experiment Objectives

Several factors determine the dose of radiation a patient will be prescribed, including location and size of the tumour, but a considerate bias is also given towards the radiosensitivity of the patient's cancer. Radioresistance is a measure of the relative resilience between cells, tissues, and organisms to the harmful effects to radiation, and radiosensitivity describes the relative susceptibility to the lethal effect of radiation [112]. X-ray radiation is most effective on cells that have a greater reproductive activity [113], for example in bone marrow where the rate of cell division is high. The most radioresistant cancers receive the heaviest doses of ionising radiation. For the FGMOSFET to operate within medical radiotherapy it needs to be sufficiently radioresistant to remain able to measure the dose of radiation it has been exposed to whilst still being a functional component throughout a patient's treatment. As such the FGMOSFET should be exposed to 100 Gy of ionising radiation, considerably more than 80 Gy typical for treatment of highly radioresistant cancers, for confidence that the FGMOSFET is reliably capable of performing as a radiation measurement component throughout a patent's entire course of treatment.

Medical use of ionising radiation to treat a cancer patient will operate with energies from 10 KeV to 25 MeV. The FGMOSFET should be able to operate within this range of radiation energy. X-rays generated in the

$10 - 30$ keV range are known as Grenz rays [114], whereas the energy range for superficial-treatment lilacs is about $30 - 125$ keV. Orthovoltage linacs generate X-rays from $125 - 500$ keV. The MeV linac has been the standard radiotherapy equipment for the past 30 years, and its production of X-rays is identical to that of a low energy linac. However, the energy range of MeV linac is quite broad by comparison, from $4 - 24$ MeV [110].

Treatment of a patient is typically completed over a number of fractions delivered weekly. For the FGMOSFET to be successful as a radiation measuring component in medical radiotherapy it should be able to accurately measure radiation during each session and also retain its predictable response to ionising radiation between treatment sessions. Configuring the dosimeter to a known state before treatment is not outside the scope of acceptable operation, but the response of the FGMOSFET must remain predictable week on week for the entire course of the treatment.

5.3.2 Technical Experiment Objectives

In addition to these operation-related performance requirements there were a few additional areas of technical interest this study was looking to satisfy from FGMOSFET exposure to ionising radiation. Analogous to the response of cell biology to ionising radiation when a silicon device is exposed to ionising radiation there are both immediate and a latent effects caused by radiation damage.

Also of interest, the discernible performance difference found in the ability of the FGMOSFET to act as a device measuring the absorbed dose of ionising radiation when the density of charge on the floating-gate region of the transistor is maximum, minimum, or in between. It is known that the performance of the FGMOSFET as a dosimeter is the result of the movement of charge within the transistor caused by the very radiation it is measuring, and it is therefore pertinent to investigate the difference in shift of electrical characteristics of the FGMOSFET with a different pre-charged density on its floating-gate region when subject to ionising radiation.

Within the FGMOSFET the V_{Th} of the device is determined by the stored

charge of the floating-gate. In other words, the stored charge of the floating-gate of the FGMOSFET is the pre-charge density of the device. In the context of the conventional use of the FGMOSFET in digital electronics the stored charge of the floating-gate is what defines the electrical bias needed on the transistor's gate in order to switch the device from an 'on' to an 'off' state, and vice versa. However, in the analogue context the stored charge of the floating-gate is exploited in an alternative manner to determine the absorbed dose of ionising radiation the device has been exposed to. Incoming ionising radiation will cause a shift of stored charge through one of two mechanism, electron-hole pair production, or migration of majority carriers. In this analogue context the pre-change density will have a bearing on the V_{Th} of the device. As more ionising radition comes in the more V_{Th} will shift, either positively or negatively depending on the majority carriers of the device. However, in addition to this effect, the pre-charge density will determine the rate at which the V_{Th} property of the transistor will vary for a constant rate of incoming ionising radiation. The greater the density of trapped charge within the FGMOSFET the greater the probability of movement of charge due to exposure to ionising radiation. As such, observing to what degree of difference the pre-charge density makes on the FGMOSFET a measure of device sensitivity becomes possible. If at a high pre-charge density the FGMOSFET exhibits a significant rate of change of V_{Th}, by comparison to the rate of change of V_{Th} at a lower pre-charge density, then the device would possibly be useful in low-dose high-precision applications. However, equally as interesting is a transistor with a small or negligible rate of change in V_{Th} for the same radiation exposure and pre-charge density, as such a device would have a greater region of linearity under which it exhibited a response to incoming EM waves. In such a scenario that device would be would possibly be useful in high-dose long delivery duration applications.

Consideration of the recoverability of the FGMOSFET after exposure to ionising radiation is consideration of the immediate effects of ionising radiation on the FGMOSFET. The principle method of operation by which the FGMOSFET is capable of acting as a radiation measurement component has to do with the displacement of stored charge within the device. This

effect of ionising radiation on the FGMOSFET has been extensively studied elsewhere [115]. Incoming ionising radiation will induce movement of stored charge within the FGMOSFET. This induced movement of stored charge has been credited to two phenomena, electron-hole pair generation within the silicon dioxide region near either the floating-gate or the interface of the transistor, and the displacement of stored charge from the floating-gate region of the transistor [116]. However a closer look at the recoverability of the FGMOSFET is thought to provide an insight into the predominant cause of charge migration within the FGMOSFET during ionising radiation exposure.

Recoverability of the FGMOSFET refers to the quantity of pre-charge density the transistor can achieve after its exposure to ionising radiation. It is know that the change in V_{Th} is what is observed during, and after, radiation exposure of the transistor, and that this change in V_{Th} is caused by one of two phenomena. However, if the majority effect causing this change in V_{Th} of the FGMOSFET undergoing radiation exposure is through the displacement of stored charge from within the floating-gate region of the transistor then the majority of the pre-charge density of the transistor can be restored after irradiation. By contrast, if the majority effect causing the change in V_{Th} of the FGMOSFET undergoing radiation exposure is through electron-hole pair generation within the silicon dioxide region then the majority of the pre-charge density of the transistor can not be restored after irradiation. This is because the pre-charge density of the FGMOSFET refers to the forced trapping of majority carriers in the floating-gate region of the device.

Consideration of the annealing effects of ionising radiation is consideration of the latent effects of ionising radiation on silicon. In the fabrication of doped silicon, controlled annealing is used to introduce dopant impurity atoms into the crystal structure of the lattice. This process alters the electrical properties of the semiconductor.

5.4 Experiment Overview

This experiment was to determine the radiation effects on sub-millimetre FGMOSFET devices, specifically to determine if the FGMOSFET is suitable to measure the absorbed dose of relatively low energies of ionising radiation typically produced by an X-ray/γ-ray linac routinely used to treat a cancer patient.

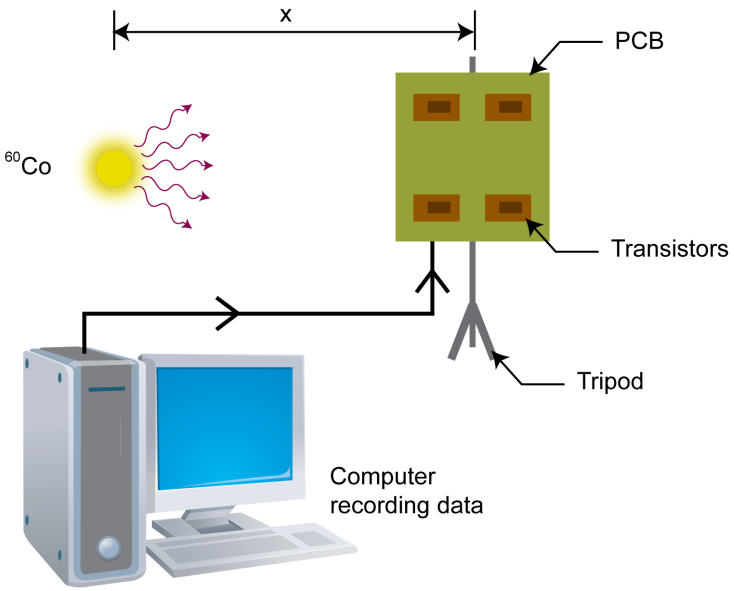

Figure 5.2: Experiment apparatus as set-up to irradiate an array of FGMOSFET devices with ionising radiation.

Figure 5.2 is a graphic to illustrate the experimental set-up necessary to irradiate a sample of FGMOSFET devices with a low dose radiation source. This experimental set-up was adopted to determine the suitability of the FGMOSFET to measure the absorbed dose of ionising radiation typical of medical radiotherpay. A printed circuit board (PCB) was designed and fabricated specifically to house an array of FGMOSFET devices securely whilst they were being irradiated. A ^{60}Co source was used to provide a uniform field of constant radiation that the FGMOSFET devices were exposed to while the experiment was running. A tripod clamp was used to hold the PCB in a

fixed position and at a fixed distance from the radiation source. The tripod clamp used to hold the PCB was orientated so that the PCB was directly facing the radiation source providing the most uniform possible field of exposure to the transistors. The tripod clamp was placed at a predetermined distance from the radiation source, a distance that would ultimately determine the duration of exposure. The distance between the radiation source and the PCB is marked by x in Figure 5.2. A customised cable was assembled for the experiment to provide reliable measurements as data moved to and from the PCB and a computer. The process of recording measurements for the duration of the experiment was automated by a computer programme. The results from the experiment were stored on the computer for later analysis.

The objective of the study was to evaluate the change in the electrical characteristics of the FGMOSFET based on its exposure to ionising radiation. An observable shift in the electrical characteristics of the FGMOSFET by exposure to ionising radiation is known to occur due to the movement of charge within the FGMOSFET. By exposing the FGMOSFET to a controlled source of ionising radiation whilst accurately recording, in real-time, any shift in the electrical characteristics of the FGMOSFET a correlation can be made between the rate of absorbed dose of ionising radiation and the observed shift in electrical properties of the FGMOSFET.

5.4.1 The Radiation Bunker

With permission from Brunel University their low dose radiation bunker was used to carry out this experiment. Figure 5.3 is a plan-view of the radiation bunker at Brunel University that clearly marks the layout of the bunker.

The bunker has a swipe card and key lock on the main entrance. Anyone entering the bunker will step into the observation post. The location of the observation post is a safe place to stand while any experiment is underway. The observation post has space for the experimental apparatus any user may want to operate whilst their experiment is running. The bunker itself is built around the radiation chamber. The radiation chamber is lined by concrete walls on every side and it is where the ^{60}Co source is kept. The ^{60}Co source is

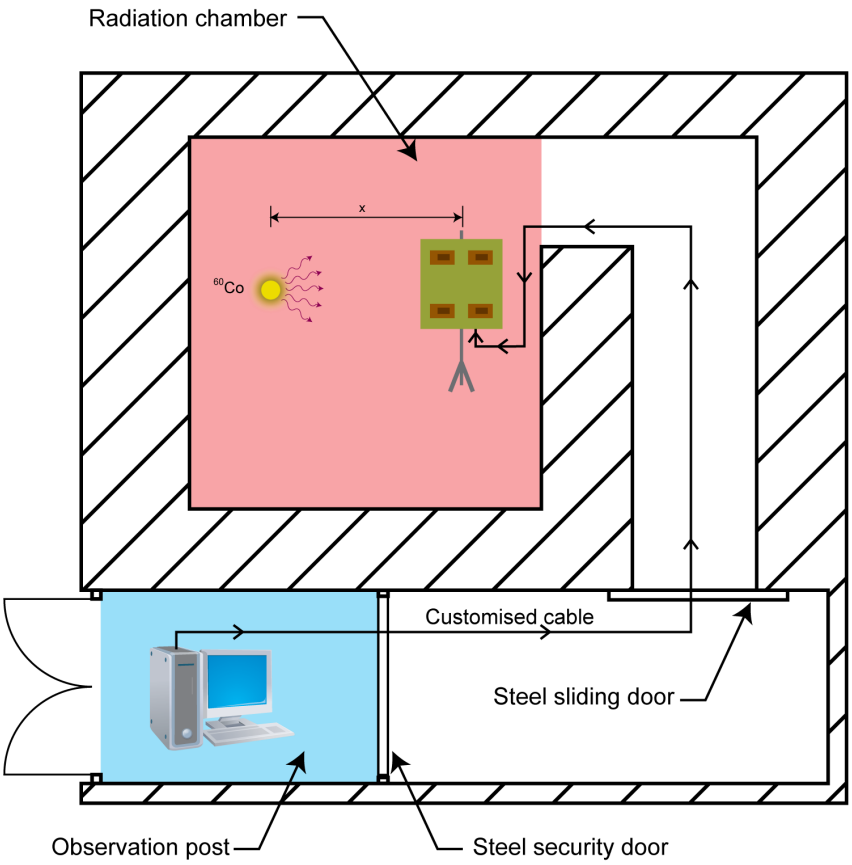

Figure 5.3: A plan-view of the low dose radiation bunker at Brunel University.

secured within a mechanised box that is operated from the observation post. When the radiation source is opened the ^{60}Co source will fill the radiation chamber with a uniform radial field of γ radiation. Also in Figure 5.3 the experimental apparatus set-up from Figure 5.2 is superimposed on the bunker plan-view layout. This additional information has been added to help depict how the experiment was implemented from within the bunker.

Working with materials as hazardous as ^{60}Co necessitates strict adherence to rigorous health, safety, and security protocols. These measures include swipe card and key access to the bunker, a log book to record users present during sessions, thermoluminescent dosimeter badges to detect accidental dose overexposure, and two steel security doors between the radiation chamber and the observation post. The ^{60}Co source is normally secured in a closed state and the source is unrevealed. When the ^{60}Co source is unrevealed the radiation chamber can be unlocked, users can enter the radiation chamber, and it is safe for the users to set-up the apparatus inside the radiation chamber for the experiment. The ^{60}Co source cannot be revealed whist the two steel security doors granting access to the radiation chamber are open and unlocked. The key required to reveal the ^{60}Co source is the same key used to unlock the steel security door adjacent to the observation post. The key cannot be removed from this steel security door until the steel security door has been pulled over to the closed position and its lock has been turned to the locked position. To turn the lock to the locked position on the steel security door the user must be standing on the observation post side of the steel security door. Only when the key is used from inside the observation post can the ^{60}Co source be moved to the open state and the radiation source be revealed. Once the ^{60}Co source is revealed the flow of γ radiation begins. It is imperative for user safety that this protocol is not compromised.

5.4.2 The Radiation Source

The radiation source of the low dose bunker at Brunel University is a ^{60}Co source, a radioisotope with a 5.27 year half-life. ^{60}Co will decay, by beta decay, to the stable isotope of nickel-60 (^{60}Ni). The decay scheme for ^{60}Co

is shown in Figure 5.4. This decay scheme depicts the decay of ^{60}Co. Note there are two γ photons emitted as the unstable ^{60}Co radioisotope decays to the stable ^{60}Ni isotope. The beta emission of the ^{60}Co source results in the emission of two γ-rays, one with 1.17 MeV and the other with 1.33 MeV of energy. However the 1.17 MeV energy photons account for more than 99 % of the irradiated γ-rays produced by the decaying radioisotope. Using a radiation source emitting photons of 1.17 MeV of energy is a suitable source substitution to replicate the typical radiation energy a cancer patient would receive from a radiotherapy linac to treat a cancer they have been diagnosed with.

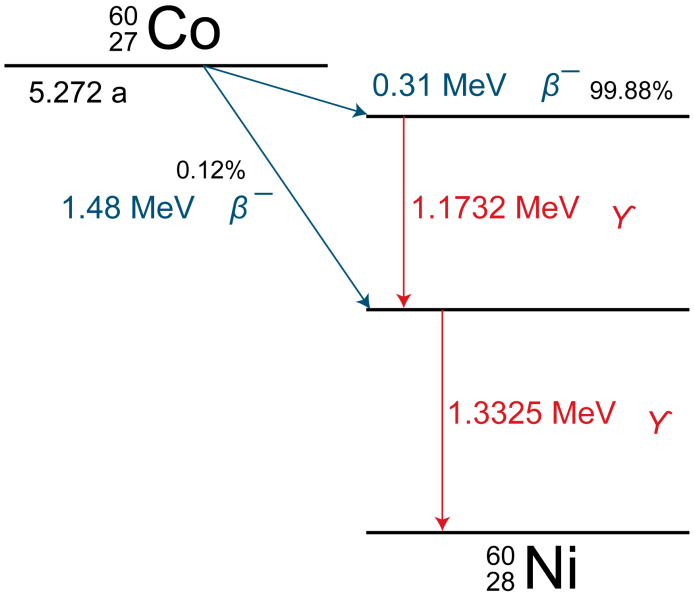

Figure 5.4: The decay scheme for a ^{60}Co radioisotope.

Before the experiment could begin the ^{60}Co source had to be calibrated. Calibration before starting the experiment is done to determine the dose rate of the ^{60}Co source. The present operating dose rate for the source is needed to determine the precise set-up of the equipment for the experiment. As the ^{60}Co source is a radioisotope the number of beta decay events diminishes with time, and it therefore follows that the rate of γ-rays produced by the radioisotope also decreases with time. The present operating dose rate from

the ^{60}Co source is a critical calibration measurement for the experiment. Typically the ^{60}Co source is being used to irradiate a target with a precise dose of radiation and the effect from this total dose exposure is what the user is measuring. The experimental data the user is looking to obtain from a ^{60}Co based radiation experiment is defined by the total dose of radiation the target has been exposed to. The total dose of radiation the user wants the target to receive is determined by dividing the total intended dose by the present operating dose rate of the ^{60}Co source. The resulting number is the duration of time the target needs to be exposed to the ^{60}Co source. What makes determining the present operating dose rate of the ^{60}Co source more complex is that the radial emission of ionising radiation coming from the ^{60}Co source obeys Newton's inverse square law. The inverse square law can be used to describe the propagation of EM waves when the photons are emitted from a single source. It states, the dose rate from the radiation source is inversely proportional to the square of the distance from the radiation source. This means the dose rate at 2 m from the ^{60}Co source is $\frac{1}{r^2}$ of the dose rate at 1 m. In other words the critical pre-experiment calibration measurement of the present operating dose rate from the ^{60}Co source is necessary to determine both the duration of the experiment and the precise distance the target needs to be from the source to ensure the total dose received by the target matches the intended dose to be received by the target.

To calibrate the radiation source, and determine its present operating dose rate, two steps are taken. First is to determine the expected operating dose rate for the radiation source, and second is to confirm the present observed dose rate for the radiation source. The expected operating dose rate for the ^{60}Co source is found to be referring to the decay profile for the particular source. The present observed dose rate for the ^{60}Co source is made by using a digital dose rate meter.

Table 5.1 shows the dose decay profile for the low dose ^{60}Co radiation bunker at Brunel University. Table 5.1 is only an extract from the full dose decay profile for the working life for this particular ^{60}Co sample at the Brunel University bunker. Table 5.1 shows the dose decay profile for 2008, from month 96 through to month 108 of the working life for the source, and as

	Activity		Dose Rate @ 10 cm		Dose Rate @ 40 cm	
Date	Half-Life	Ci	Gy/min	mGy/sec	Gy/min	mGy/sec
Jan '08	1.5180	10.44	0.1996	3.3273	0.0125	0.2080
Feb	1.5338	10.33	0.1975	3.2910	0.0123	0.2057
Mar	1.5497	10.22	0.1953	3.2551	0.0122	0.2034
Apr	1.5655	10.10	0.1932	3.2197	0.0121	0.2012
May	1.5813	9.99	0.1911	3.1846	0.0119	0.1990
Jun	1.5971	9.89	0.1890	3.1499	0.0118	0.1969
Jul	1.6129	9.78	0.1869	3.1155	0.0117	0.1947
Aug	1.6287	9.67	0.1849	3.0816	0.0116	0.1926
Sep	1.6445	9.57	0.1829	3.0480	0.0114	0.1905
Oct	1.6603	9.46	0.1809	3.0148	0.0113	0.1884
Nov	1.6762	9.36	0.1789	2.9819	0.0112	0.1864
Dec	1.6920	9.26	0.1770	2.9494	0.0111	0.1843
Jan '09	1.7078	9.16	0.1750	2.9173	0.0109	0.1823

Table 5.1: The decay profile data of the ^{60}Co source in the low dose radiation bunker at Brunel University for the year of 2008, as expected by the provider of the ^{60}Co source.

the experiment was carried out in July 2008 it is the July record from the table that is most relevant to the experiment's set-up. The data presented in Table 5.1 is taken from a compressive table provided with the ^{60}Co, and, as such, the data in this table was not measured or calculated as part of the experimental process. This data is provided as a point of reference.

In order to confirm the expected dose rate of the radiation source a PTW Farmer Air Ionisation Chamber is placed at 10 cm directly in front of the radiation source, the radiation chamber in the bunker is sealed, and the dose rate was measured using a Thermo Scientific NE2670 Farmer Dosemeter from the observation post within the bunker.

On the 23rd of July 2008, with the ionisation chamber at 10 cm from the ^{60}Co source, the NE2670 recorded a dose rate of 3.3333 mGys^{-1}. From Table 5.1 the expected dose rate is 3.1155 mGys^{-1}. That gives an operating error of $\pm$6.99 %, an error that should be considered when estimating the absorbed dose of radiation the experiment's target has received. This measurement completes the calibration of the radiation source, a necessary calibration before the experiment begins in order to determine the distance

the radiation source should be from the target, or x in Figure 5.2.

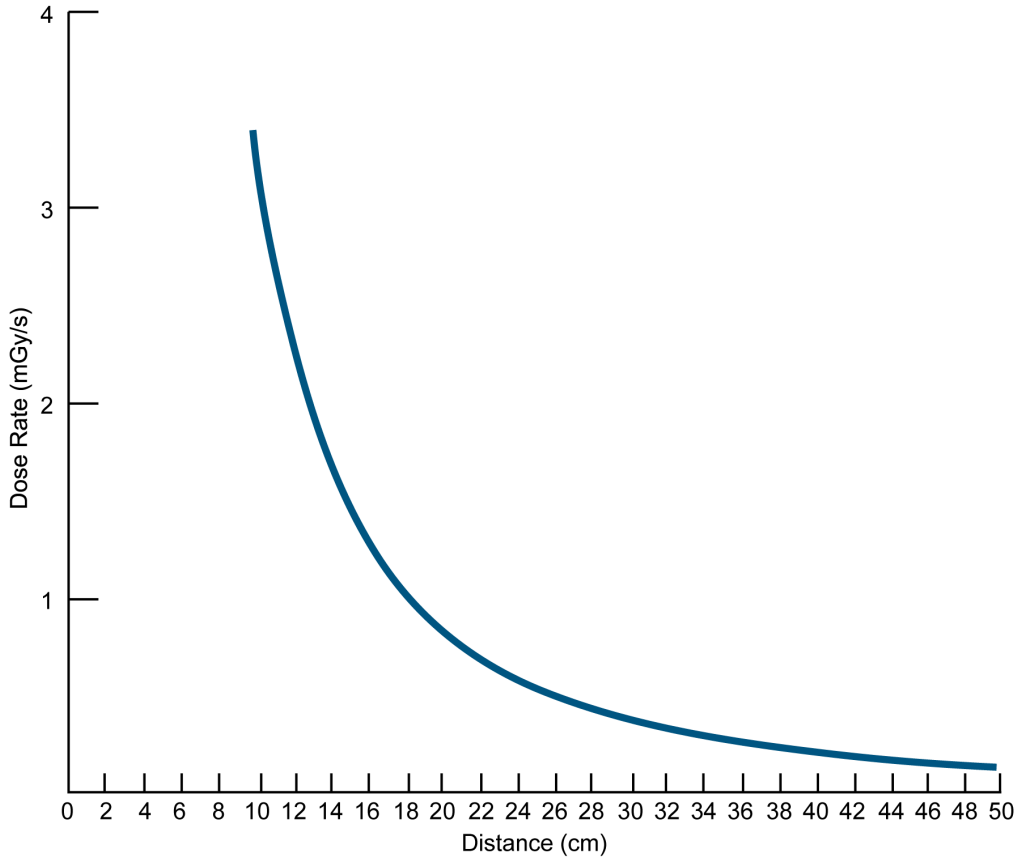

Figure 5.5: The absorbed dose as a function of distance for the ^{60}Co source in the low dose radiation bunker at Brunel University.

Knowing a dose rate at a fixed distance from the source is the only necessary piece of information required to determine the dose rate at any reasonable distance from the source. Using a single calibration point a dose/distance profile can be drawn up. Working with the dose rate of 3.3333 mGys^{-1} at 10 cm from the ^{60}Co source recorded on the 23rd of July, 2008 the dose/distance profile from Figure 5.5 is drawn up. The 23rd of July, 2008 is a significant date as this is the date that the transistors under test were irradiated. This plot is characteristic of the inverse square law and it depicts the relationship between dose rate and distance, that the dose rate

is diminishing as one over the square of the distance from the source.

Table 5.2 is an extract from a more complete table describing the absorbed dose of radiation as a function of distance from the radiation source. The extract shown in Table 5.2 is presented to better understand the distance chosen for the experiment, the distance between the radiation source and the centre of the PCB. Table 5.2 has been included to justify the initial value chosen for x in Figure 5.2.

		Dose Rate		Total Dose (Gy)		
x (cm)	$1/r^2$	$mGys^{-1}$	Gys^{-1}	185 min	186 min	187 min
8.5	0.01384	4.61315	0.00461	51.206	51.483	51.760
8.6	0.01352	4.50649	0.00451	50.022	50.292	50.563
8.7	0.01321	4.40349	0.00440	48.879	49.143	49.407
8.8	0.01291	4.30398	0.00430	47.774	48.032	48.291
8.9	0.01262	4.20780	0.00421	46.707	46.959	47.212
9.0	0.01235	4.11481	0.00411	45.674	45.921	46.168
9.1	0.01208	4.02488	0.00402	44.676	44.918	45.159
9.2	0.01181	3.93785	0.00394	43.710	43.946	44.183

Table 5.2: Data for the dose as a function of distance for the ^{60}Co source in the low dose radiation bunker at Brunel University for the year of 2008.

5.4.3 The FGMOSFET, ALD1123E

The MOSFET transistor is an electronic component fabricated from the arrangement of three doped silicon regions. Silicon is known to be sensitive to ionising radiation such that with sufficient exposure to ionising radiation the silicon structure of the MOSFET transistor will degrade such that the transistor may no longer functions with acceptable performance. This kind of degradation is irreversible. This limitation of the MOSFET transistors, its susceptibility to ionising radiation, extends to the FGMOSFET. If the FGMOSFET is exposed to sufficiently energetic ionising radiation for a sufficiently long period of time then the FGMOSFET component will become irreversibly damaged beyond any practical use. However, despite the damage caused by ionising radiation on silicon, the assumption that the FGMOSFET will be a successful candidate as an electronic component capable of meas-

uring the absorbed dose of radiation comes not from its commonality with all MOS transistors in its response to ionising radiation, but instead its favour will be justified with the addition of a the floating-gate region to the MOSFET's structure. More specifically, optimising the shape and size of the floating-gate region to the FGMOSFET can potentially lead to considerably greater performance of the FGMOSFET as a radiation measuring component for medical dosimetry over any alternative MOS transistor.

The use of RADFET devices as dosimeters for ionising radiation is well established [117, 118, 119]. These devices are normally operated with a large gate biases, $10 - 100$ V, for optimum electron-hole pair generation caused by radiation exposure [91]. RADFET devices can also be operated with 0 V on the V_{GS}, but the sensitivity due to radiation exposure is generally reduced by a factor of $5 - 10$ [117]. Due to the fabrication limitations and more demanding operation requirements the FGMOSFET is favoured over the RADFET.

If the FGMOSFET has a floating-gate region that is significantly larger in proportion to the rest of the component then, by virtue of the difference in proportionate size of the adjacent regions, when the FGMOSFET is exposed to ionising radiation the floating-gate region of the transistor will absorb considerably more ionising radiation compared to the rest of the transistor. It is this design advantage of the FGMOSFET that should prove the FGMOSFET to be sufficiently resilient to the damaging effects of ionising radiation, yet still function after the most aggressive of radiotherapy regimes a patient might be prescribed and also perform with the necessary sensitivity.

To validate the suitability the MOS transistor in the measurement of the absorbed dose of ionising radiation during medical radiotherapy this experiment used a FGMOSET component that is commercially available, the ALD1123E from Advanced Linear Devices Inc. (ALD). Based in Sunnyvale, California, ALD has been in the business of developing and manufacturing CMOS linear integrated circuits since 1985.

The ALD1123E is a monolithic quad electronically programmable analogue device consisting of four n-type FGMOSFET devices. The choice to use a commercially available FGMOSFET component instead of designing a

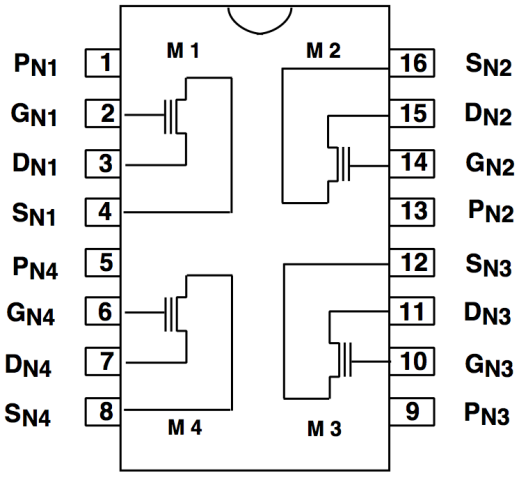

Figure 5.6: The pin diagram of the ALD1123E, a package enclosing four FGMOSFET devices, each with an electrically adjustable V_{Th}.

transistor from the ground up, such that it would be optimised to the particularly disagreeable operating conditions of medical dosimetry, is twofold. For one, without having first completed some preliminary work to demonstrate the theory behind the FGMOSFET as a radiation measurement component for medical radiotherapy it is unlikely to secure the funding required to pay for the fabrication of a custom design FGMOSFET optimised for the intended application. However the second reason to go with a commercially available FGMOSFET device instead of a custom design component, and arguably a more valid reason for the decision to use the ALD1123E, is that the four transistors on the ALD1123E chip have electrically adjustable V_{Th}, or turn-on voltage.

Using the E100 EPAD programmer in conjunction with the ALD1123E IC devices the V_{Th} of each transistor in the package can be programmed. Programming a transistor on the ALD1123E using the E100 external programmer will result in the charge density on the floating-gate region of the transistor being altered. The programmer works to add charge to the floating-gate of the FGMOSGET device and thus increase the necessary V_{GS} to attract a sufficient number of charge carriers into the inversion region of the transistor to enable a flow of current between the drain and source

when a V_{DS} potential is applied. The V_{Th} of a transistor can be set between 1.000 V and 3.000 V with steps of 0.1 mV. Due to the electrical isolation of the floating-gate in the transistor any charge added to this region has no means to migrate out of this region provided the transistor is used under conventional operating conditions. There is no limit to the number of times a transistor in the ALD1123E package can be programmed.

Exposing the ALD1123E to ionising radiation constitutes unconventional operating conditions and it is under the influence of ionising radiation that the behaviour of the FGMOSFET was studied. The experiment was to quantify a measurable shift in the electrical characteristics of the FGMOSFET by exposing it to ionising radiation, specifically addressing the shift in the V_{Th} based on its exposure to ionising radiation. By using ALD1123E devices in conjunction with the E100 programmer an array of transistors was used, each with their own programmed V_{Th}, and this experimental configuration afforded two important characteristics of the FGMOSFET device to be investigated. Firstly, programming the array of transistors to varying V_{Th} across the array meant the experiment could investigate the performance difference between transistors with different densities of charge in their floating-gate region when exposed to the same dose of ionising radiation. Secondly, to programme a ALD1123E device for a second time after its exposure to ionising radiation meant the predominant effect of ionising radiation on the FGMOSFET could be isolated. To programme the device after its exposure to ionising radiation meant the cause of the movement of charge within the FGMOSFET due to ionising radiation could be isolated to either the displacement of stored charge from within the floating-gate region of the transistor or the electron-hole pair generation within the silicon dioxide region near either the floating-gate or the interface of the transistor. The premise for this assumption has to do with the processes involved when the FGMOSFET is being programmed. The E100 programmer includes a specialist circuit to safely apply an inordinate bias to V_{GS} inducing the hot-carrier injection technique where free-electrons are encouraged into the floating-gate region by the force of an electric field. Once charge is trapped in the floating-gate region, and the transistor returned to a circuit of normal operation, the V_{Th} for the

transistor will become permanently altered. So should the FGMOSFET be programmed to a maximum V_{Th} initially and then when the transistor is irradiated by a controlled source of ionising radiation the V_{Th} value will diminish. After radiation exposure is complete the transistor can be programmed back to V_{Th} maximum, if obtainable. The question then becomes, by programming the FGMOSFET after its been irradiated, can the electrical characteristics of the device be recovered to pre-irradiation performance. This recoverability of the transistor is a means to measure the portion of the ionising radiation that is responsible for irreversible destructive damage to the FGMOSFET. Should the irradiated transistor be programmed to the same pre-irradiation maximum V_{Th}, and the electrical characteristics of the transistor match its pre-irradiation performance, then it becomes reasonable to approximate that the majority of the absorbed dose of ionising radiation acted on the stored charge within the floating-gate region of the FGMOSFET device and not on any other part of the transistors. Or, at least to say, any absorbed ionising radiation by parts of the transistor outside the floating-gate region left negligible effects on the transistor such that its performance was persevered between harsh radiation sessions.

This arrangement of the ALD1123E IC being used in conjunction with the E100 programmer means both the recoverability of the FGMOSFET and the radiation hardness of the device could be quantified.

5.4.4 Printed Circuit Board

From Figure 5.3 it is clear a PCB was used to hold the irradiated transistors in place during the experiment. Considerable effort was spent calculating the duration of the experiment based on the present operating dose rate of the radiation source and the distance of the transistors from the source. As such it was imperative that the position and orientation for the array of transistors remained fixed and secure throughout the experiment. The solution used was a PCB circuit to hold four ALD1123E devices in place, provide a bias circuit to ensure a constant I_{DS}, and provide a reliable cable connector for continuous data to and from the PCB and the computer recording the results.

The PCB was held in place by a clamp on a tripod. This made it easier to position the PCB at a measured distance from the source.

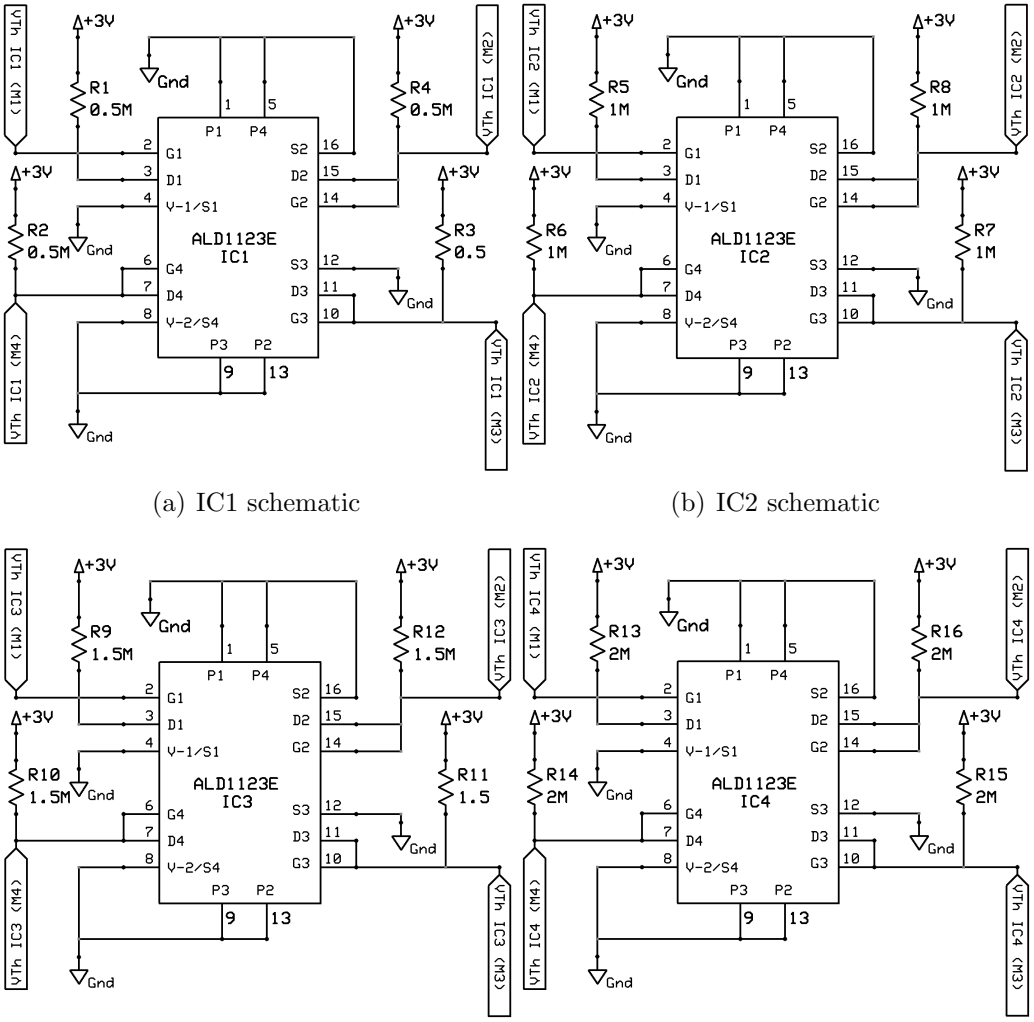

(a) IC1 schematic

(b) IC2 schematic

(c) IC3 schematic

(d) IC4 schematic

Figure 5.7: Various edge detection algorithms

Before the PCB could be fabricated a schematic of the intended circuit was required. From the circuit schematic the CAD work necessary to layout the PCB could be accomplished. Figure 5.7 is a summary of the four IC packages used on the PCB. For the four ALD1123E transistor IC packages each circuit is presented through; Figure 5.7(a), Figure 5.7(b), Figure 5.7(c),

and Figure 5.7(d). The current limiting resistor network for each IC is on the V_{GS} pin of each transistor. Note that each IC houses four transistors, and so there is a current limiting resistor network at each V_{GS} pin on each of the four transistors. The resistor network for IC1 has a 0.5 MΩ bias on V_{GS}, for IC2 with 1 MΩ bias on V_{GS}, for IC3 with 1.5 MΩ bias on V_{GS}, and IC4 with 2 MΩ bias on V_{GS}. However, the schematic of the fabricated PCB is captured through five figures in total. In addition to the four transistor ICs, and their respective current limiting resistor networks, a connector was required to bridge communication between the PCB and the PC recording experimental measurements.

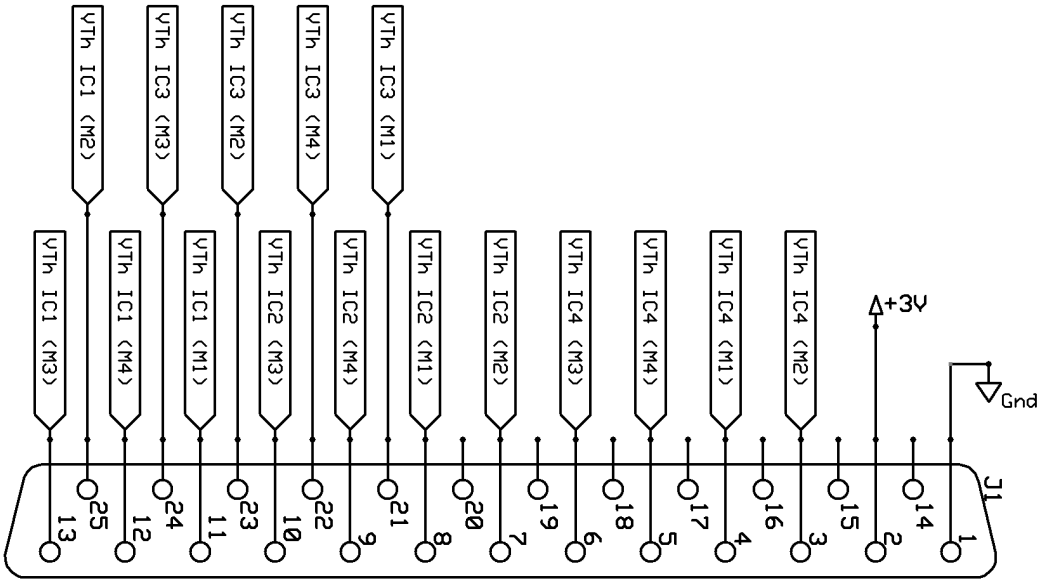

Figure 5.8: 25-way parallel port connector, from PCB to PC..

The fifth schematic required to build the PCB to house four ALD1123E packages is presented in Figure 5.8, the 25-way parallel port connector. This connector provided the interface between the PCB and the PC taking measurements. Only 16 of the 25 lines on the 25-way connector were required. But in order to work with an established form-factor a 25-way parallel port adapter was used.

To understand the link between each of the individual schematic diagrams consider each terminal with the same label to be hardwired on the PCB. For

example, in Figure 5.7(a) the V_{out} used to measure the change in V_{Th} for the first transistor from the first IC throughout the experiment is labelled with the terminal, "V_{Th} IC_1 (M_1)". This is pin 2 of IC1. From Figure 5.8 the terminal labelled, "V_{Th} IC_1 (M_1)", is connect to pin 11 of the 25-way parallel port connector. Therefore, for the PCB CAD layout, pin 2 from IC1 is connected to pin 11 of the 25-way connector.

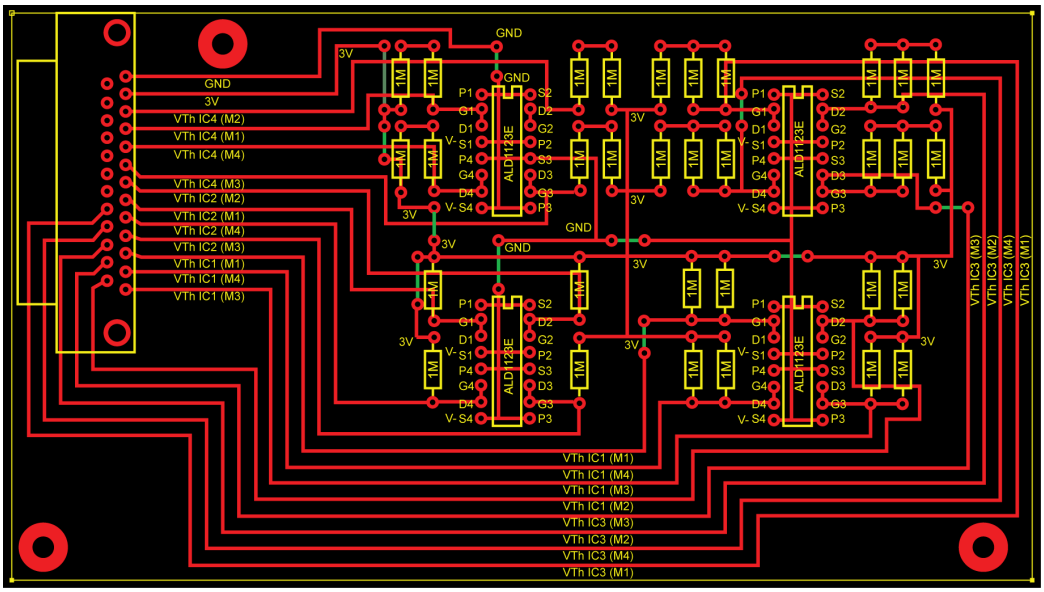

Figure 5.9: The CAD diagram of the PCB circuit containing four ALD1123E devices.

The CAD of the circuit for the PCB is presented in Figure 5.9. This is a simple circuit and highlights how only a limited number of components were necessary for the successful operation of the circuit. The circuit contained four ALD1123E chips, and each ALD1123E chip contains four FGMOSFET devices. The experiment was designed to measure any change in V_{Th} due to ionising radiation and so the V_{GS} pin of each of the four transistors from each of the ALD1123E chips had to run from the PCB to the computer recording the results from the experiment. That is a total of 16 data lines from the PCB to the computer. It is worth noting that there was no power supply included as part of the electronic circuit on the PCB. In addition to the 16 datalines the PCB also had a 3 V power line and a ground line running to

the PCB from the computer recording the experiment's result.

To meet the experimental objectives the four ALD1123E packages were programmed before the experiment began. To make it easier to determine which transistor was programmed to what initial V_{Th} all four transistors on a single ALD1123E package were programmed to the same V_{Th}. However in order to investigate by how much, if at all, the magnitude of the programmed V_{Th} makes to the rate of change of V_{Th} due to ionising radiation, each of the four ALD1123E packages was programmed to a different initial V_{Th}. So for all four transistors the approximate initial threshold voltages were as follows: $V_{Th1} = 1$ V, $V_{Th2} = 2$ V, and $V_{Th3} = 3$ V. For V_{Th4} the package was programmed beyond the recommended operating V_{Th}, and instead programmed to the maximum possible V_{Th}. This was a necessary measure to investigate which region of the FGMOSFET responds most to ionising radiation. As such, $V_{Th4} = 3.5$ V.

The other requirement of the PCB circuit was to ensure $I_{DS} = 1$ μA across all transistors. The circuit for each transistor is kept in saturation with the gate and drain shorted together. The source is pulled to ground, and the ground is common to all devices. Depending on the initial V_{Th} a specific arrangement of resistors biased the drain pin of the transistor. For example, a transistor from IC_2 was programmed with a $V_{Th} = 2$ V, and with the need for $I_{DS} = 1$ μA a resistance of 1 MΩ between the supply rail and the gate was chosen.

To the left of the diagram is the footprint of a standard 25-way parallel port connector. Although the total number of lines running from the PCB was 18 it was thought that a standard parallel port connector would provide a secure connection between the PCB and computer recording the results.

5.4.5 Electrical Noise Issues

From Figure 5.3 it is clear a cable was needed to run from the PCB holding the array of transistors inside the radiation chamber to the computer in the observation post recording the experiment results. Although only 18 lines were needed the cable chosen was an adapted 25-way cable. Using a standard

25-way parallel cable that was adapted to the experiment meant a reliable signal could be transported from the radiation target to the computer.

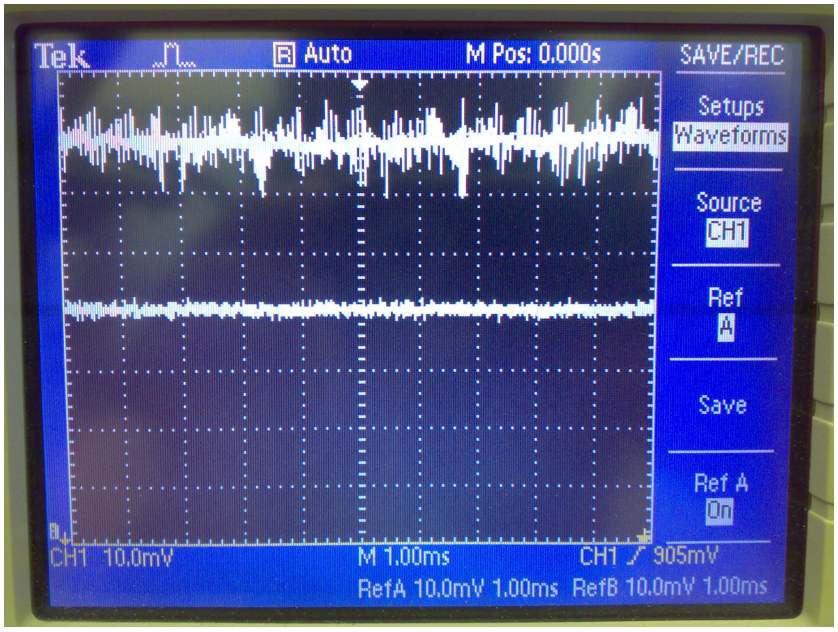

Figure 5.10: This image is a screen capture from an oscilloscope used to measure the relative difference in signal quality of the customised cable assembled for this experiment.

The screening of the 15 m cable assembled was found to be crucial as the noise levels measured without proper screening were around 10 times higher. The Figure 5.10 is a screen shot from the oscilloscope used to measure the signal V_{GS} from the first IC. The signal to the top of the figure is from the cable without screening, and the signal below that is of the cable with screening. Testing the quality of the customised cable improved the reliability of the data the experiment produced.

5.4.6 LabVIEW Automation

Referring to Figure 5.3 the layout of the experimental apparatus within the bunker is reviewed. Included is a computer positioned at the observation post. This computer was used to observe the progress of the experiment

while the experiment was running, as well as to record the data gathered from the experiment.

The computer was running an instance of LabVIEW, a popular tool for the automation of the experimental process and typically used in conjunction with National Instruments' data acquisition (DAQ) hardware. LabVIEW boasts a user-friendly interface and its graphical programming language makes experiment automation intuitive to set-up.

For the experiment completed the LabVIEW programme recorded data from all 16 transistors across all four ALD1123E devices. The LabVIEW programme was set so that every second it would record the V_{GS} value for each of the transistors.

The data points captured from the LabVIEW programme wrote directly to an Excel spreadsheet. An Excel spreadsheet is a useful starting point for the manipulation of experimental data. An Excel spreadsheet can be quickly manipulated to produce a plot depicting the relationship observed in the experiment. However for the experiment completed with the ALD1123E devices the number of data points gathered in total rendered Excel an ineffective means of working with that data.

Having the experiment automated by using LabVIEW had the distinct advantage that the V_{GS} values for each of the transistors could be captured simultaneously as well as removing the chance of human error if the data was instead recorded by hand. The other beneficial feature to using LabVIEW to automate the experiment was the data could be plotted in real time. In other words while the experiment was running. This meant that when the experiment was running for the first time the expected decrease of V_{Th} was observed while the measured V_{GS} was being recorded. This gave confidence that the experiment had been set-up correctly.

5.4.7 Data Acquisition Interface

Although it was a cable commonly used for a parallel port interface that was customised to carry the 16 analogue V_{GS} lines, one 3 V line, and one ground line from the PCB to the computer running LabVIEW, this standard

parallel port cable was unsuitable as the interconnect between the PCB and the LabVIEW software. For the LabVIEW software to be able to record an analogue measurement of V_{GS} per transistor per second it required a Data Acquisition (DAQ) interface.

For the experiment a PCI-6259 from National Instruments was fitted to the computer. The PCI-6259 is a high speed multifunction DAQ PCI board that was connected to a SCB-68 I/O connector block. The PCI-6259 has 32 analog inputs working at 1×10^6 samples per second per channel with a 16-bit analog to digital converter. The PCI-6259 was more than capable of making the required accurate measurements of the V_{GS} at one sample per channel per second. The 18 lines from the adapted 25-way cable connected to the SCB-68 block, and from there the PCI-6259 DAQ board was addressable by the LabVIEW software.

5.5 Experiment Procedure

The experimental set-up is illustrated in Figure 5.3 and it shows that the PCB is positioned at a predetermined distance from the radiation source denoted by an x. For the experimental procedure that was carried out to determine the suitability of the FGMOSFET as an electronic component capable of measuring the absorbed dose of ionising radiation the PCB was positioned 8.7 cm from the ^{60}Co radiation source. At that distance the dose rate is 4.40 mGys^{-1} as described in Table 5.2.

Before any of the transistors were exposed to a single dose of ionising radiation all 16 transistors were programmed to have their initial V_{Th} set to a predetermined value. To make it easier to keep track of the initial V_{Th} for each transistor all four transistors on a single ALD1123E device were programmed to the same level. Sharing the initial V_{Th} on more than one transistor improved the reliability of the data found in the experiment. The transistors were programmed as such: $V_{Th1} = 1$ V, $V_{Th2} = 2$ V, and $V_{Th3} = 3$ V. To satisfy the experimental objectives V_{Th4} was programmed to the maximum possible value such that $V_{Th4} = 3.5$ V.

The experiment intended to deliver a dose as close as possible to 100 Gy

of ionising radiation, with the energy of the ionising radiation remaining unchanged at 1.17 MeV throughout the experiment. The delivery of the dose of radiation was broken into 4 phases. The phases were either radiation-on, where the ^{60}Co source is exposed, or radiation-off, where the ^{60}Co source is closed. The first phase was a long radiation-on phase. The second phase was a short radiation-off phase. The third phase was a long radiation-on phase. The fourth and final phase was a long radiation-off phase. Breaking up the dose exposure received by the FGMOSFET devices was an initiative to satisfy the complete list of experimental objectives specified at the outset. Having a first phase as a long radiation-on phase ensured there was an opportunity to observe the expected effect of a decrease in V_{GS} before carrying out the entire experiment. If this initial phase failed to produce the predicted response then the experiment was either at fault or the known effects of ionising radiation to silicon have been incorrect. With a pause between the two major doses of radiation as a short radiation-off phase, and with all transistors still biased, there was an opportunity to; first, observe an immediate halt in the decrease of V_{GS} thus confirming that it was the incoming ionising radiation causing the change in electrical characteristics of the transistor and, second, to observe any immediate annealing effects in the transistor once the incoming radiation was suspended. The advantage to making the third phase a long radiation-on phase was to bring symmetry to the first long radiation-on phase and add reliability to transistor performance as a component measurably sensitive to the effects of ionising radiation. If the measurable response of the shift in electrical characteristics of the transistors exposed to ionising radiation is reproducible then its occurrence is not an anomaly. The fourth and final phase of the experiment was a long radiation-off phase where all the transistors were still biased but with no exposure to radiation. This was to observe what long term annealing effects can occur within the transistors.

The first phase ran for 3.1 hours. The second phase ran for 1 hour. The third phase ran for 3.1 hours. The fourth phase ran for 16.5 hours. At a dose rate of 4.40 mGys^{-1} at 8.7 cm from the ^{60}Co radiation source both the long radiation-on phases were exposed to $TotalDose = 2 \times (3.1 \times 60 \times 60 \times 4.4 \times 10^{-3})$ Gy. That works out at a dose of 49.1 Gy for both the first and third

phases of the experiment, or 98.2 Gy total.

5.6 Experiment Results

In an effort to assess the suitability of the FGMOSFET as a dose measurement electronic component for the application of medical science this experiment ran for 7.2 hours automatically gathering a single value for V_{GS} of each of the 16 transistors at a rate of one data point per second. Thus totalling 26, 170 data points per transistor and more than 420 k data points over all. Analysis of this data was achieved by working with the C++ programming language using the object orientated principles of C++, direct access to memory, and the ROOT framework, to manage this large dataset. The ROOT framework, developed at CERN for the purpose of data analysis in particle physics, includes a sophisticated library of tools to translate large datasets into meaningful information.

The first calculation made after the experiment was complete was to determine more precisely the dose of ionising radiation the array of transistors was exposed to. The PCB was position 8.7 cm from the ^{60}Co radiation source, but that 8.7 cm was measured from the midpoint between all four ALD1123E devices of the PCB. On closer inspection, after the experiment was complete, it was found that each of the ALD1123E devices was 2.7 cm from the midpoint where the measurement between the PCB and the radiation source was taken. A simple pythagorean calculation corrects the distance from the ^{60}Co radiation source to the midpoint of each ALD1123E device from 8.7 cm to 9.1 cm. Referring to Table 5.2 the dose rate of ionising radiation for the ^{60}Co source that the transistors were exposed to changes from 4.40 mGys^{-1} at 8.7 cm to 4.03 mGys^{-1} at 9.1 cm. As the first and third phases of the experiment were both long radiation-on phases totalling 6.2 hours in duration, the corrected total dose of ionising radiation the FGMOSET devices were exposed to is 89.95 Gy for 6.2 hours.

In an effort to provide clarity to the initial outcome of the experiment Figure 5.11 shows the data from just one transistor from the four separate ALD1123E devices. As each ALD1123E chip was programmed to different

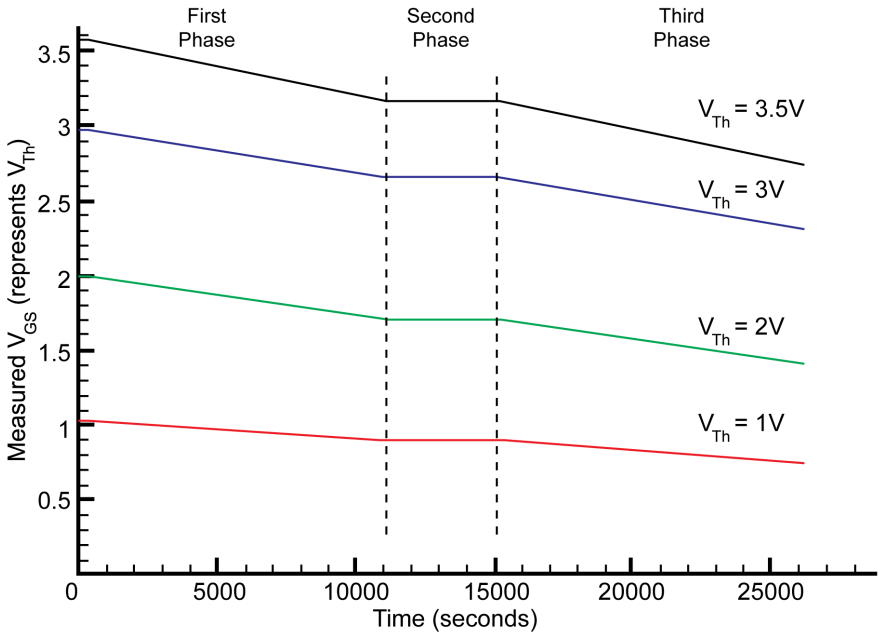

Figure 5.11: A plot expressing V_{GS} against time from the third transistor from each of the four ALD1123E devices.

V_{Th} values before the experiment began, this plot provides a snapshot of what was precisely experienced by each transistor whilst they were irradiated by the ^{60}Co radiation source for 6.2 hours at a radiation energy level of 1.17 MeV throughout the experiment. The first observation to make from this plot is how the plot is clearly divided into three distinct phases. The first phase is characterised by the first downward slope in each of the four transistors presented in Figure 5.11. The second phase is characterised as a flat line, V_{GS} is no longer decreasing though the second phase. The third phase is characterised by the same downward slope found in the first phase. It is also worth mentioning that the transition between the three phases occurs at the same point in time for all four transistors and because Figure 5.11 shows data from each to the ALD1123E devices being irradiated it can be said that the cause for transition between the phases must be the same for all four ALD1123E devices. The second observation to make from the plot presented in Figure 5.11 is the distinct difference in gradient between the

four transistors. The gradient of the decaying V_{GS} is symmetric about the first and third phase of the experiment for each transistor suggesting the slope is responding to the same stimulus in both the first and third phases of the experiment, while the difference in slope between the four transistors correlates to their different initial programmed V_{Th} values.

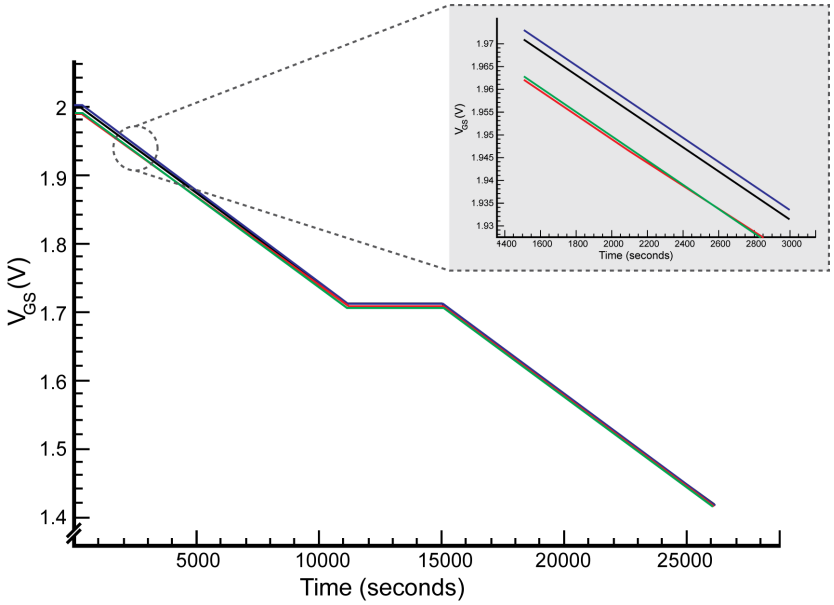

Figure 5.12: This plot shows the data from all four transistors on the ALD1123E device programmed with $V_{Th} = 2$ V before the experiment began.

On closer inspection of the data another interesting result is discovered. Figure 5.12 presents the measured V_{GS} as a function of time from four transistors again but, unlike Figure 5.11, the data in this plot is for four transistors all from the same ALD1123E device. That means all four transistors started the experiment with the same programmed value, $V_{Th} = 2$ V. If the four separate transistors are hard to distinguish in Figure 5.12 it is due to the high quality matching achieved within the fabrication process, a testament to the quality of engineering from ALD. To highlight the fact there are in indeed four transistors in this plot a snippet of the plot is scaled up to illustrate just what is going on with the V_{GS} characteristic of the FGMOSFET while the experiment is running. This snippet is taken only 20 minutes

into the experiment highlighting that there is no delay to the response of the FGMOSFET to ionising radiation. The snippet is a detailed view over a period of approximately 30 minutes. The most noteworthy observation to be made from the data presented as a snippet compared to the data being presented as a whole, although on the scale of the entire experiment it may appear unclear, is that there is indeed a marginal discrepancy between each of the four transistors from a single programmed ALD1123E device. For a more precise and quantified measure of the sensitivity of the FGMOSFET to ionising radiation a statistical analysis is needed.

The sensitivity of the FGMOSFET is measured as the change in V_{GS} as a function of time. With the way the experiment was set-up the total dose for each transistor is known to be 89.95 Gy at 9.1 cm from the ^{60}Co radiation source. At this distance the dose rate is measured at 4.03 mGys^{-1}. Therefore to determine the sensitivity of the FGMOSFET as a radiation measuring electronic component the rate of change of V_{GS} was calculated. An approximation of the sensitivity to dose of the FGMOSFET was statistically determined by calculating the gradient of a least square linear fit using all the measured V_{GS} data during both the long radiation-on phases of the experiment. The sensitivity of the FGMOSFET to the dose of ionising radiation was calculated from the data points measured during the long radiation-on phases of the experiment, a total of $10,878$ from a possible $26,170$ data points for each transistor.

	First Phase Sensitivity		Third Phase Sensitivity	
Transistor	VGy^{-1}	σ	VGy^{-1}	σ
1	6.52×10^{-3}	0.196×10^{-6}	6.54×10^{-3}	0.300×10^{-6}
2	6.55×10^{-3}	0.118×10^{-6}	6.57×10^{-3}	0.207×10^{-6}
3	6.67×10^{-3}	0.155×10^{-6}	6.65×10^{-3}	0.390×10^{-6}
4	6.61×10^{-3}	0.157×10^{-6}	6.64×10^{-3}	0.210×10^{-6}

Table 5.3: Approximate sensitivity of the ALD1123E device programmed to $V_{Th} = 2$ V and calculated by taking a least square linear fit of the data from the two irradiation phases.

Table 5.3 provides a summary of the approximated sensitivity for the ALD1123E device programmed to $V_{Th} = 2$ V. This table highlights the mar-

ginal discrepancy shown in the scaled up snippet from Figure 5.12. Notice how close each approximate sensitivity is between the four devices and the symmetry found between the two phases of radiation exposure. The data presented in Table 5.3 shows the amplitude of the approximate sensitivity calculated for the transistors in the ALD1123E device programmed to $V_{Th} = 2$ V. Of course, looking at Figure 5.12 the direction of sensitivity could be expressed as a negative number highlighting it was a decaying shift in V_{GS} the experiment observed. In addition to this, from the data presented in Table 5.3, σ is the error for the data collected on each transistor measured, where each transistor was programmed with a threshold voltage, $V_{Th} = 2$ V. Each σ value in Table 5.3 is for one of the four transistors in the $V_{Th} = 2$ V sample. σ is an indicator of how tight the data is about a line of best fit for the dataset presented. The smaller the value for σ the lower the measure of erroneous data points off the line of best fit, thus giving more confidence in the data itself.

	Initial V_{Th}	First Phase Sensitivity		Third Phase Sensitivity	
Chip	V	VGy^{-1}	σ	VGy^{-1}	σ
1	1.0	3.1×10^{-3}	13.5×10^{-6}	3.2×10^{-3}	12.3×10^{-6}
2	2.0	6.5×10^{-3}	66.5×10^{-6}	6.6×10^{-3}	53.5×10^{-6}
3	3.0	7.2×10^{-3}	20.6×10^{-6}	7.5×10^{-3}	43.5×10^{-6}
4	3.5	8.9×10^{-3}	230×10^{-6}	9.3×10^{-3}	310×10^{-6}

Table 5.4: Approximate sensitivity of all ALD1123E devices calculated by taking a least square linear fit of the data from two irradiation phases.

Table 5.4 provides a summary of the approximated sensitivity for all four of the ALD1123E devices. Each of the ALD1123E devices had all four transistors on that device programmed to the same initial V_{Th}. The sensitivity of each ALD1123E device was statistically determined by calculating the gradient of a least square linear fit using all the measured V_{GS} data during both the long radiation-on phases of the experiment. Notice again in Table 5.4, as observed in Table 5.3, there is symmetry about the two long radiation-on phases of the experiment and that the symmetry was found to change when the initial V_{Th} for the chip was higher. Notice also that the sensitivity of each ALD1123E device was found to increase when the initial V_{Th} for the

chip was higher. This observed trend of an exaggerated response to ionising radiation with a higher initial V_{Th} for the ALD1123E device is summarised in Figure 5.13.

A possible explanation as to why this phenomenon was observed suggests it is the presence of a greater electric field in a transistor that gives a transistor with a higher initial V_{Th} a greater probability of encouraging the movement of charge. The magnitude of the electric field majorities carriers, and charge in the silicon dioxide region, are subject to is dependent on the pre-charge density of the floating-gate region. For a FGMOSFET with free electrons trapped within its floating-gate region an electric field between the p-type substrate and the floating-gate's trapped charge will form. Consider the instance where incoming ionising radiation causes electron-hole pair generation through the Compton effect, if the electron of the electron-hole pair is subject to a strong electric field it will have a tendency to migrate away from its parent atom before it drops back to an energy state of an orbital electron. The stronger the electric field the more likely this effect is to occur.

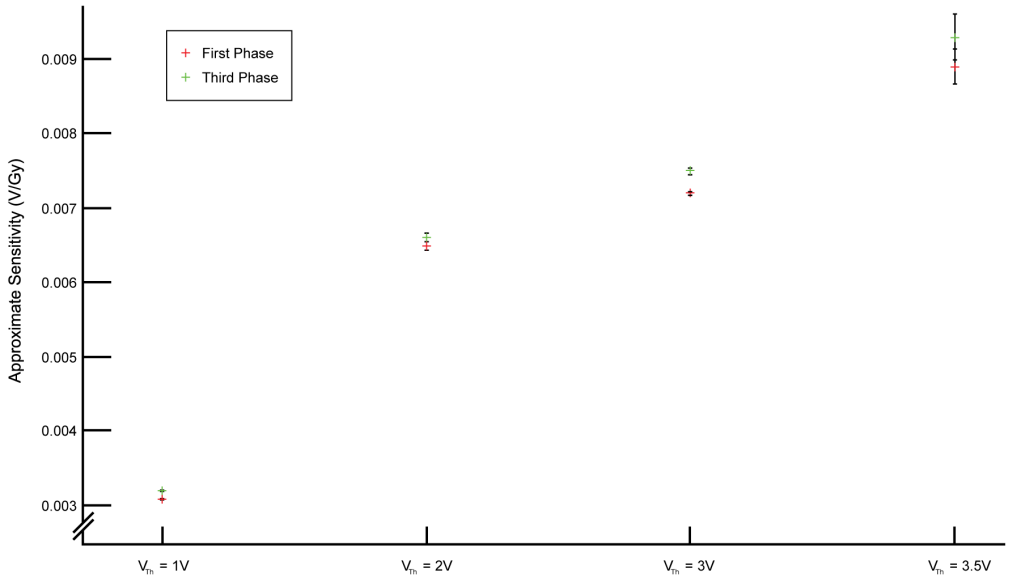

Figure 5.13: A plot to highlight the relationship between the calculated approximate sensitivity and the initial programmed V_{Th}.

The fourth and final phase of the experiment was a long radiation-off

phase where all the transistors were still biased but had no additional exposure to ionising radiation. During the fourth phase the experiment continued running, the computer continued gathering data at one data point per second, and data was gathered for a 16.5 hour duration. It was in this stage of the experiment that critical data for the annealing effects of the transistors was gathered.

$$y = A - (B \times e^{-\frac{\sqrt{t}}{T_0}}) \tag{5.2}$$

Data from the fourth stage of the experiment shows the transistors to slowly recover some of their lost V_{GS}. Using a modified exponential equation a fit was found for the data from the 16.5 hour observation period. The adapted exponential equation is described in Equation 5.2. This equation is simply an expression to fit the data based on the shape of the curve, and the significance of the equation holds no value beyond this point. $y = 1 - e^{-x}$ gives the general shape of the curve. The term, A, is a y-axis offset shifting the y-axis intercept and defining the point at which the curve will asymptote. The term, B, is an x-axis offset.

To help illustrate the measured annealing effects Figure 5.14 is a plot from just a single transistor programmed to $V_{Th} = 1$ V during the fourth phase of the experiment. Figure 5.14 is a plot including 60 k data points with each data point being measured a second apart. This plot shows an overall voltage recovery in the fourth phase of the experiment. In addition to understanding the direction the annealing effect experienced by the transistor's post irradiation the plot presented in Figure 5.14 highlights the chosen fitting curve for the modified exponential equation presented in Equation 5.2. A complete presentation of the observed annealing characteristics across all 16 transistors for the 16.5 hour period is presented in Table 5.5.

Apart from the voltage recovery the other interesting feature of the plot in Figure 5.14 is the 'ripple' on the gradually increasing curve. The rate at which the curve increases in V_{GS} is marginal by comparison to the decay of V_{GS} based on radiation exposure. However, no explanation for the noise on the data was determined. This shape could be the result of errors within the

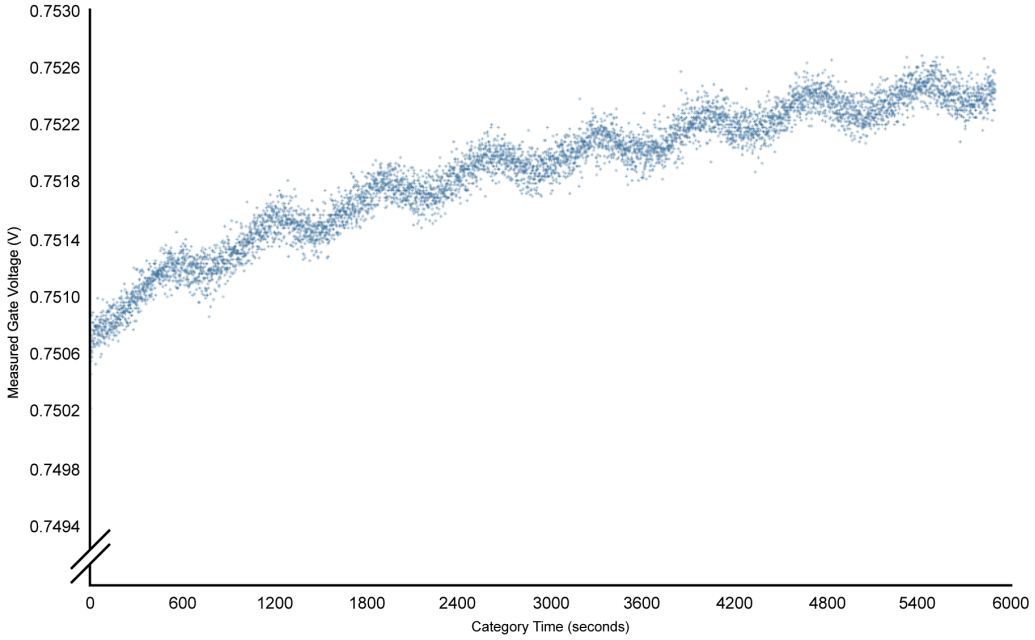

Figure 5.14: This plot shows the typical annealing effects as experiences by just one transistor programmed to $V_{Th} = 1$ V.

measurement process. Further research would be required to understand the precise cause of this effect. As no further work was completed to explore the cause of the noise on the data there is no expected behaviour to this noise.

	Initial V_{Th}	Coefficient B	
Chip	V	V	σ
1	1.0	7.6×10^{-3}	1.0×10^{-3}
2	2.0	9.0×10^{-3}	0.9×10^{-3}
3	3.0	7.0×10^{-3}	0.9×10^{-3}
4	3.5	8.0×10^{-3}	0.9×10^{-3}

Table 5.5: The data presented in the above table provides coefficient values for each initial V_{Th} a transistor may have been programmed with. The data in this table supports the proposed modified exponential fit to characterise the annealing effects observed in the fourth phase of the experiment.

The annealing effect, presented by data in Table 5.5, was an important effect to measure as part of the experimental process. Annealing within the FGMOSFET is the recovery of the V_{Th} characteristic of FGMOSFET. If the

alteration to the V_{Th} characteristic of the FGMOSFET is, in part, caused by the Compton effect of electron-hole pair generation within the silicon dioxide region of the transistor then the recovery of the V_{Th} characteristic is the electron-hole recombination occurring after radiation exposure. Now, most normally the FGMOSFET is used as a digital component, and the profiling of the effect of radiation exposure on the device is used to determine its suitability in space application. As such the annealing effect would routinely be considered negligible as a digital component works within discrete logic states, where these states have a wide tolerance for voltage differences. However, in the application of the device as a radiation measurement component the device is being used in an analogue context. Due to the continue nature of analogue electronics any small differential in electrical characteristics of the transistor will produce a margin of uncertainty into its operation.

The last result to report from this experiment concerns an observation after the radiation-on fourth phase. After the forth phase of the experiment was complete all four ALD1123E devices were removed from the PCB and stored, unbiased, at room temperature for three days. All four ALD1123E were effectively switched off. After the three day period the four ALD1123E devices were programmed for a second time to their initial V_{Th} using the E100 EPAD programmer. A breakdown of the average percentage recoverability measured is presented in Table 5.6. From this table it is worth noting that the recoverability of the FGMOSFET seems to degrade as the initial V_{Th} of the transistor is higher. The measured results include a limit of accuracy about the programmer capable of voltage adjustments of 0.1 mV between a 1.000 V and 3.000 V range.

Table 5.6 presents the average recoverability found for programming each of the four ALD1123E devices after the fourth phase of the experiment was complete. Recoverability is considered the measure of how much of the initial pre-programmed threshold voltage the device can achieve after radiation exposure. If radiation exposure is primarily causing a change in the electrical characteristics of the transistor, but also causing irreparable degradation of the device, then it is reasonable to assume that after radiation exposure the transistor is no longer capable of performing to the level it was origin-

	Initial V_{Th}	Programmed V_{Th}	
Chip	V	%	σ
1	1.0	98.5	0.7
2	2.0	100.1	0.2
3	3.0	89.9	15
4	3.5	73.1	6.5

Table 5.6: This table presents the average recoverability found for programming each of the four ALD1123E devices after the fourth phase of the experiment was complete.

ally calibrated to. As such the recoverability of the device is measured as a percentage, highlighting the degree of performance loss due to radiation exposure.

5.7 Experiment Conclusion

The results presented in this chapter are based on the investigated effects of γ radiation from a ^{60}Co source on the electrical characteristics of a commercially available programmable floating-gate NMOS transistor. As illustrated in Figure 5.11 there was a measurable change in the V_{Th} across all transistors, irrespective of their initial programmed V_{Th}, with excellent linearity and little sensitivity spread being observed.

All 16 transistors in the experiment were initially thought to be exposed to a dose of 98.2 Gy of ionising radiation, but this measurement was later corrected to a more accurate value where the total dose received by the transistors was 89.95 Gy. Although 89.95 Gy is less than the 100 Gy dose intended for the experiment it is still a dose that exceeds the most aggressive of radiotherapy treatment plans a patient could be prescribed. Thus making the results presented in this chapter still within the context of the application of medical radiotherapy.

During radiation exposure the absorbed dose of ionising radiation was measured in real-time as a shift in the measured V_{GS}. The approximate sensitivity across all devices was calculated with the maximum sensitivity of 9 mVGy^{-1} found for the transistors programmed with the initial $V_{Th} = 3.5$ V.

The sensitivity saturation at higher biases is consistent with the floating-gate transistor approaching the limit of its charge storage capacity, i.e. the greater the initial V_{Th} of the device the stronger an electric field the electron-hole pairs produced will be subject to.

Figure 5.11 also highlights the difference in the response of a FGMOSFET depending on its initial V_{Th}. The gradient to all four plots in Figure 5.11 shows that the rate of change of measured V_{GS} is greater for transistors with a higher initial V_{Th} compared to transistors with a lower initial V_{Th}.

At room temperature the annealing effect that was measured during the fourth phase of the experiment found a maximum recovery of 8 mV over a 16.5 hour period.

The final stage of the experiment investigated the recoverability of the transistors, what portion of ionising radiation exposure caused permanent irreversible damage to the transistors. It was found that for the devices programmed to the highest initial V_{Th} that their recoverability, post irradiation, was poorest with only an approximate 73% of their initial V_{Th} being recoverable.

A closer look at the recoverability of the FGMOSFET is thought to provide an insight into the predominant cause of charge migration within the FGMOSFET during ionising radiation exposure. The two possibilities include; electron-hole pair generation within the silicon dioxide region near either the floating-gate or the interface of the transistor, and the displacement of stored charge from the floating-gate region of the transistor. Whatever charge cannot be recovered once the transistor has been programmed after exposure to ionising radiation is due to the electron-hole pair generation within the silicon dioxide region of the FGMOSFET.

The major physics points of the FGMOSGET include; electron-hole pair generation within the silicon dioxide region of the transistor, the induced electric field caused by the pre-charged floating-gate region of the transistor, and the movement of change based on the Compton effect.

With the experiment investigating the response of the FGMOSFET across all programmed initial V_{Th} values the radioresistance of the transistors in the ALD1123E package was investigated. As all the devices continued to respond

to the total dose of radiation throughout the duration of the experiment the FGMOSFET was found to be sufficiently radioresistant to the harmful effects of ionising radiation whilst still remaining functional as a component measuring the received dose of ionising radiation.

A scanning electron microscope was used to capture an image of the integrated circuit beneath the protective packaging surrounding the ALD1123E device and it was estimated the footprint to a single transistor is approximately $75 \times 200\ \mu\text{m}^2$. At this size footprint it proves promising that a customised device could be used in a more final implementation of a dosimeter that would be small enough for an implantable medical application.

It has been recognised that the medical application of ionising radiation in the treatment of cancer is with an operating range of energies from 50 KeV to 25 MeV for an X-ray/γ-ray radiation beam. This experiment used a ^{60}Co radiation source capable of producing 1.17 MeV γ radiation only. This experiment did not investigate the performance of the FGMOSFET through the range of operating energies for radiotherapy but it did observe the response of the FGMOSFET by measuring its change in electrical characteristics during its exposure to ionising radiation of an energy within the range of operating energies for radiotherapy.

The structure of this experiment was broken into phases with the dose of radiation being delivered during two long radiation-on phases separated by a short radiation-off phase. The response of the transistors exposed to ionising radiation was consistent between the two long radiation-on phases. This symmetry about the first and third phase of the experiment shows a performance consistency between the dose exposure sessions, and is comparable to the expected operating conditions of the practical dosimeter in radiotherapy being used while the patient returns week on week for their followup radiotherapy appointment.

The second phase of the experiment was a short radiation-off phase that clearly shows an immediate halt in the decay of the measured V_{GS} when the radiation source has been closed. This response from all 16 FGMOSFET devices supports the idea that it is the ionising radiation that is responsible for the change in electrical characteristics of the transistor.

The size, sensitivity, and programming characteristics of these devices suggest that this type of floating-gate technology would be suitable as an electronic component capable of measuring the absorbed dose of ionising radiation for the application of medical dosimetry for radiotherapy.

5.8 Further Work

The work completed to achieve the results presented in this chapter was substantial, however more can be done to improve this study to assess more completely the suitability of the FGMOSFET as an electronic component for the measurement of absorbed dose of radiation.

Testing the FGMOSFET with a 100 Gy dose of ionising radiation would determine if the FGMOSFET is sufficiently resilient to retain performance in the harshest of cancer treatments.

Although the results presented demonstrate the suitability of the FGMOSFET as a radiation dosimeter for medical radiotherapy, the FGMOSFET has been demonstrated to operate at one specific energy of X-rays only. Testing the FGMOSFET against the spectrum of energies a patient may be prescribed would be a prudent calculation to ensure the FGMOSFET is operational across the full energy spectrum for radiotherapy. The ^{60}Co source is a strong 1.17 MeV energy source, and although the data gathered from experimenting with this radioisotope forms a good bases of knowledge about the performance of the FGMOSFET, and that modelling of the effect of varying energies could be simulated, the range of energies practical radiotherapy extends to far exceeds the mid-level 1.17 MeV photons used here.

The X-ray/γ-ray based radiation source represents the treatment technology of the vast majority of oncology clinics in the UK. However high energy photons only make up one type of radiation that can be used in the treatment of cancer. Testing the FGMOSFET as a dosimeter in treatments using a proton or heavier ion beam would be to assess the suitability of the FGMOSFET for the next generation of technologies to be adopted more widely in the treatment of cancer.

The most important next step for this project would be to repeat the

experiment after the development of a custom designed FGMOSFET for the intended application of medical radiotherapy. The results in this chapter clearly demonstrate the FGMOSFET can be used as an electronic component to measure the absorbed dose of radiation but the FGMOSFET in the form presented by the ALD1123E package is not suitable for an implantable dosimeter. A custom design FGMOSFET is needed to confirm it can be integrated with the other necessary electronics to form an integrated system and act as a functional implantable dosimeter.

This chapter has presented the results from a study to investigate the performance of a commercially available programmable FGMOSFET as a radiation measurement component. It has been presented in this chapter that measuring the V_{GS} of a FGMOSFET while it is exposed to ionising radiation will provide a real-time measurement of the absorbed dose of radiation the transistor has been exposed to. It has been shown that the response of the FGMOSFET when exposed to ionising radiation produces excellent linearity between the measured V_{GS} and the dose it has been exposed to, with a sensitivity of up to 9 mVGy^{-1} recorded.

5.9 Summary

This chapter has presented an experiment to characterise the suitability of the FGMOSFET as an electronic component for radiation measurement. This chapter has presented the experimental method where the FGMOSFET was exposed to a ^{60}Co radiation source producing 1.17 MeV γ radiation at a dose rate of approximately 4.03 mGys^{-1} at 9.1 cm from the source. This chapter has presented the results of the experiment using the ALD1123E, a commercially available chip containing four separate FGMOSFET devices each with a programmable initial V_{Th}. The best sensitivity found was 9 mVGy^{-1} and the worst recoverability was 73% of their initial threshold voltage for the transistors programmable to the highest $V_{Th} = 3.5$ V. This chapter has presented the conclusions of the experiment stating the ALD1123E provides strong evidence of the suitability of the FGMOSFET as a radiation measurement device for medical dosimetry, but that further work should be carried

out to characterise a custom built transistor optimised for the application of IVD.

Chapter 6

Micro Antenna Experiment and Results

6.1 Introduction

This is a results chapter and the data presented within this chapter make up a credible academic contribution to the field of in-vivo dosimetry for radiotherapy. The results discussed in this chapter have undergone peer review and been published in the journal of Radiation Measurements Journal [120].

This chapter will begin with a quick overview of the expected working environment for a medical instrument operating during the course of a radiotherapy treatment. An overview of this working environment will contextualise the aims and objectives of this study. For an implantable electronic dosimeter for radiotherapy there will need to be an antenna to provide wireless communication between the device and the medical physicist. This chapter presents the work and results of a study that characterised three alternative micro antenna designs to determine which design is best suited for IVD. The chapter will provide a detailed report on every stage to the micro antenna experiment should there be a need to replicate the results found.

6.2 The Operating Environment

Radiotherapy is the use of an external source of ionising radiation to target a predetermined volume of a patient within which lies a cancerous growth. Ionising radiation is lethal to all cells, healthy and malignant, and radiotherapy is indiscriminate in dose delivery. All exposed cells within the target volume, and along the axis of propagation the radiation beam is aligned with, are subject to the same harmful effects of radiation exposure. The need for continual improvements to QA in radiotherapy is paramount to ensure confidence in patient safety. Dosimetry, the measurement of absorbed dose of radiation, is a popular choice for QA technology in radiotherapy where verification of the intended dose can be made by comparing it with the measured dose during treatment. Up until very recently, despite the literal meaning of IVD, dosimetry during treatment has been completed using external dosimeters. The delivered dose is then estimated using a mathematical calculation of the absorbed dose at the target volume. The reason for this crude approach to QA in radiotherapy is mainly due to a lack of available cost effective implantable dosimeters for radiotherapy. One recent study using an internal dosimeter during patient treatment has highlighted the previously unknown and undetected inaccuracies of conventional EBRT in the treatment of cancer, finding a > 5 % variance in 40 % of breast cancer patients, and a > 5 % variance in 36 % of prostate cancer patients, across 1,600 fractions [121]. The results from this study demonstrate the advantages of having the treatment dosimeter implanted within the patient. Not only will an implantable dosimeter improve QA in radiotherapy by accurately measuring the absorbed dose but it will also accurately measure the absorbed dose at the target volume and inform the medical physicist of what portion of the intended dose was delivered to the cancer.

As an implantable dosimeter is intended to be internalised during radiotherapy treatment a natural consideration is the risk to a patient undergoing treatment. Implantable medical devices monitor and treat physiological conditions within the body, and these devices, including; pacemakers, implantable cardiac defibrillators, drug delivery systems, and neuro-stimulators, can

help manage a broad range of medical issues, such as cardiac arrhythmia, diabetes, and Parkinson's disease [122]. More than 25 million patients in America alone have one type of implantable medical device or another [123]. Due to the possible dangers of such medical devices, and their prevalence within modern medical treatment, regular review of risks and recommendations on the routine use of implantable deceives is discussed [124].

Fabricating such an implantable medical dosimeter, capable of running over several treatment fractions, and maintaining reliability throughout the patient's treatment programme, is not without its challenges. It has been recognised that should an implantable dosimeter for IVD be made from semiconductor materials it is possible to overcome some of the fabrication and design challenges by integrating a silicon based dose measurement component with the control electronics in a single integrated circuit [125]. Of course any implanted medical device taking real-time measurements would require wireless communication to connect the medical physicist with the device before the measurement could be read out. Although previous attempts to build an implantable dosimeter for IVD have been successful [126] the advantage of an integrated circuit design, where both the control electronics and dose measurement electronics are are sub-millimetre, is lost when the antenna for such a dosimeter is anything larger than sub-millimetre. It was therefore the ambition of this experiment to design and characterise a sub-millimetre antenna that could be added to the integrated circuit, including the control electronics and dose measurement electronics, of a new enhanced dosimeter to keep the overall design of the dosimeter sub-millimetre.

Radiotherapy is a treatment of cancer delivered at a specialist oncology clinic, a clicic that is usually apart of a hospital. The sensitive nature of electronic equipment in a hospital's operating environment has led the Medicines and Healthcare products Regulatory Agency (MHRA) to recognise that electromagnetic radiation can interfere with some medical devices [127]. Particularly if used within 2 m of such devices. As such the MHRA has advised on an NHS hospital-wide ban of mobile phones where necessary. It is such sensitivities over the potential risks associated with unrestrained use of wireless electronic devices within a hospitals that has led to some governments

allocating a dedicated band of frequencies for their explicit use within the medical context. This includes the 1999 introduction of the Medical Implant Communication Service (MICS) specification by the US Federal Communications Commission (FCC) [128].

The MICS specification is an unlicensed range of frequencies that can only be used by medical electronics including the pacemaker and the camera pill amongst other examples [129, 130, 131]. It has been determined that the MICS range of frequencies, from the available range of frequencies at the time the FCC was making a decision, best meet the technical requirements for medical devices. The technical requirements for the assessed MICS frequencies determined how conducive the tested frequencies were to the propagation of EM waves within the human body.

It is therefore prudent in the design of a new enhanced implantable dosimeter that requires a wireless channel for communication to adhere to the MICS specification. Thus ensuring its compatibility within the operating environment of a hospital. This chapter presents the work and results of a study that characterised three alternative micro antenna designs to determine which of these design is best suited for IVD while accommodating the MICS specification where possible.

6.3 Experiment Aims and Objectives

An implantable dosimeter for routine use to improve QA in radiotherapy has an operation related performance requirement of wireless communication. An implantable dosimeter for IVD is a dosimeter that is placed inside the target volume of the patient before radiotherapy treatment begins and remains inside the target volume throughout the course the of treatment until all treatment fractions are complete. It is therefore necessary for the implanted dosimeter to have a wireless channel of communication for the medical physicist to be able to interrogate the device and determine the absorbed dose of ionising radiation the dosimeter has recorded. This study was to determine the best micro antenna for wireless communication for an implantable dosimeter for radiotherapy.

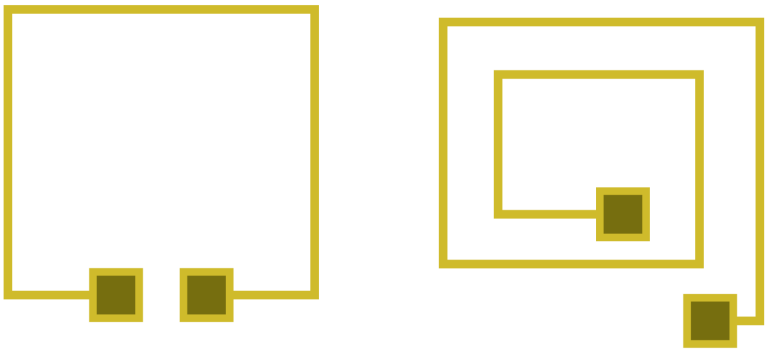

(a) Single-loop design. (b) Multi-loop design.

Figure 6.1: The two design types of micro antenna characterised for dosimetry application. Figure 6.1(a) the single-loop design. Figure 6.1(b) the multi-loop design.

Figure 6.1 illustrates the difference between the two types of design of micro antenna this study characterised for IVD. The multi-loop antenna design for Figure 6.1(b) differs from the single-loop antenna design of Figure 6.1(a) by containing more than one loop of antenna trace about itself. It was the ambition of the experiment presented in this chapter to complete a performance comparison between the single-loop and multi-loop design approach of the micro antenna for wireless medical devices.

The MICS specification, defined by the FCC, states that electronic devices used within a hospital environment for the wireless communication of biotelemetry between a patient's medical sensors and a doctor's corresponding readout equipment can safely operate within an unlicensed band of frequencies dedicated to this application provided the electronic device operates within the specification. The MICS specification declares the 401 MHz to 406 MHz range of frequencies as reserved for the wireless communication of medical devices, provided the maximum transmit power is low. Low power means an equivalent isotropic radiated power that is no greater than 25 μW and a maximum bandwidth does not exceed 100 kHz at any one time. Thus the MICS specification obliges a low data rate system. Using the established FCC specification for RF operation in wireless medical electronics as a

guideline on performance requirements of a micro antenna for an implantable dosimeter it was the ambition of this experiment to characterise the response of both the single-loop and multi-loop antenna design using no more than 100 kHz of bandwidth close to the allocated 401 MHz to 406 MHz range of frequencies.

Given that an implantable dosimeter will measure the absorbed dose of ionising radiation within the target volume during radiotherapy treatment, and that radiotherapy treatment will be delivered within the hospital environment of an oncology clinic, the expected operational requirements for IVD are uniquely low power and short range. That means, for any integrated micro antenna sharing the same circuit as a silicon based dosimeter component and control electronics, the received signal communicating the measured absorbed dose of ionising radiation need only be a discernible signal above the background noise and at no more than 2 m from the patient.

6.4 Experiment Overview

The aim of this experiment was to investigate the RF performance achievable by a custom built integrated micro antenna fabricated on an integrated piece of silicon, and to determine the best micro antenna between the single-loop and multi-loop design for the application of medical dosimetry to improve QA in radiotherapy as part of a cost effective implantable dosimeter for IVD.

Fabrication of the micro antennas was completed by the Micro and Nanotechnology Centre (MNTC), a group based at RAL. Funding for the fabrication of the micro antennas was provided by the Innovations Ltd. group, also based at RAL. The Innovations Ltd. group granted a £20,000 sum to pay for the work completed by MNTC. The funding from Innovations Ltd. covered the cost of micro antenna fabrication only, and came with a mandatory requirement. The experimental objective was for the results obtained from characterising the micro antennas fabricated by the MNTC to further support the innovation of a new enhanced dosimeter design. That design should eventually include the micro antenna as part of an integrated circuit where the shared silicon would also include a dose measurement component

and control electronics. The Innovations Ltd. funding was therefore a funding provided to carry out a feasibility study working towards a proof in concept of the proposed dosimeter. The funding from Innovations Ltd. covered the cost of the MNTC fabricating three batches of micro antennas only. The micro antenna design could be altered between each batch and each antenna in a batch was be identical. It was therefore imperative that the design for each batch of micro antennas was optimised, without mistakes, and sufficient to meet the experimental objectives. A sample of three micro antennas from a fabrication batch was used for the experimental procedure.

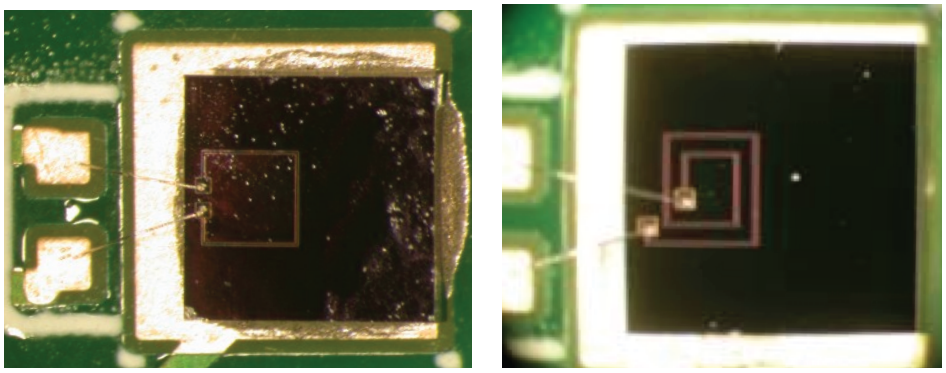

(a) Single-loop antenna. (b) Multi-loop antenna.

Figure 6.2: The wire bond interconnect between the micro antenna and PCB for, the single-loop design in Figure 6.2(a), and the multi-loop design in Figure 6.2(b).

Figure 6.2 shows the technique of wire bonding being used as an interconnect is made between the PCB and the IC containing the antenna. In total three batches of micro antennas were fabricated by the MNTC. The first and second batches were of the single-loop micro antenna design, and the third batch was of the multi-loop micro antenna design. The sample of three micro antennas characterised each were mounted to their individual PCB before being characterised by the complete experiment procedure. The process of characterising a sample of micro antennas from each fabricated batch was to build a performance profile as a function of distance of the micro antennas by measuring a revived signal that the micro antenna was transmitting. The information gained from characterising a batch of micro

antennas was used to optimise the design of the subsequent batch of micro antennas the MNTC produced.

6.4.1 Antenna Fabrication Process

Before the fabrication of a particular micro antenna design an estimate of the expected performance of the micro antenna design was predicted based on a derivation of the micro antenna's layout using Maxwells equations and the Maple mathematical package. Once the shape and size of the micro antenna had been determined the micro antenna design was modelled using Synopsis TCAD, a computer simulation software that helps to optimise semiconductor device design. Based on the TCAD schematic the MNTC produced a batch of micro antennas.

In total three batches of micro antennas were fabricated by the MNTC. Each subsequent batch of micro antennas was only fabricated after the characterisation of the pervious batch was complete. In this way the data gathered on a batch of micro antennas could be used to make improvements to a subsequent batch before it was fabricated by the MNTC.

Before the design of any micro antenna was started a couple of necessary design rules were observed. The design of the micro antenna should not exceed 1 mm in length on any side to ensure its compatibility with the overall design requirements of a new enhanced dosimeter for IVD. In addition, the design of the micro antenna should observe a void in the centre of the antenna loop to improve the quality of the magnetic flux produced by the micro antenna, thus improving the overall efficiency of the loop based micro antenna. The magnetic permeability, μ, depends on the medium within which the field exists, and within a vacuum the magnetic permeability is, $\mu_0 = 4\pi \times 10^{-7}$ Hm^{-1} [132]. The permeability of a material characterises the response of that material to a magnetic field. In a simplified model the permeability of a material is often regarded a constant for that given material. All micro antennas were fabricated on a double polished 520 μm silicon n-type with a resistivity between 1 $\Omega\mathrm{cm}^{-1}$ and 10 $\Omega\mathrm{cm}^{-1}$.

From Figure 6.3 the size and dimensions of the fabrication process for

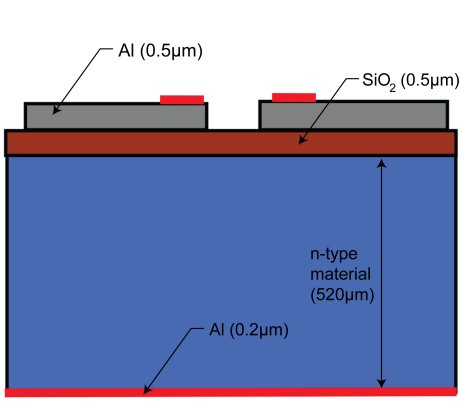

(a) Schematic for first batch.

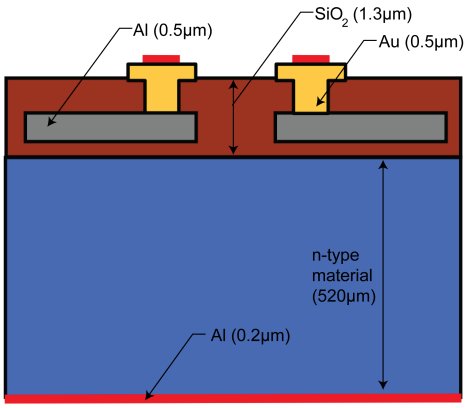

(b) Schematic for second batch.

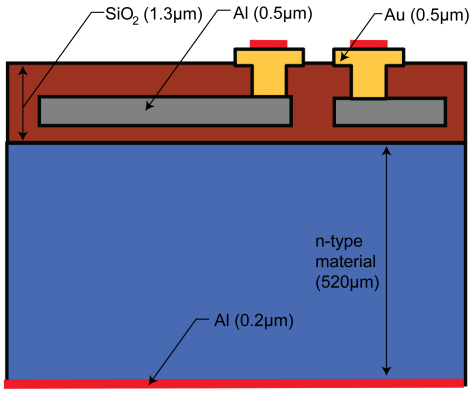

(c) Schematic for third batch.

Figure 6.3: Above are the schematics of the three batches of micro antenna fabricated by the MNTC. Figure 6.3(a) schematic for the first batch. Figure 6.3(b) schematic for the second batch. Figure 6.3(c) schematic for the third batch.

all three batches of micro antenna, as completed by the MNTC, can be appreciated. For the fabrication of the first batch of micro antennas, as shown in Figure 6.3(a), a 200 nm layer of aluminium was deposited onto the reverse side of the polished silicon 520 μm thick substrate using a sputter coating technique. From the front face of the silicon wafer a 0.5 μm thick insulation layerof SiO_2 was deposited using the plasma-enhanced chemical vapour deposition (PECVD) technique. Electron beam lithography was then used, with a 0.9 μm thick positive tone resist to form the device template, and a 0.5 μm thick aluminium layer was deposited using a thermal heating technique, and finally the lift off process was used to clear the resist. For the second and third batch of micro antennas, as shown in Figure 6.3(b) and Figure 6.3(c), the fabrication process was adapted slightly to instead leave the micro antenna trace embedded within the SiO_2 layer of insulation. To achieve this an additional 0.8 μm layer of SiO_2 was deposited using PECVD and the embedded micro antenna was added using the photolithography technique.

The need to introduce an additional 0.8 μm layer of SiO_2 to embed the top surface of the micro antenna trace was only considered after the first batch of micro antennas was fabricated and tested. In the lab the performance of the first batch of micro antennas was lower than expected. A theorised explanation of this underperformance was to do with the exposure of the top surface of the micro antenna trace. As the top surface of the micro antenna trace was exposed to air it was subject to the possible effect of interacting with oxygen in the air, and partially oxidising. With the introduction of the this impurity to the top surface of the micro antenna trace the conductivity of the trace itself would become compromised. So, for the subsequent fabricated batches of micro antenna the top surface of the micro antenna trace was buried under a 0.8 μm layer of SiO_2 to keep the electrical properties of the traces from becoming altered.

6.4.2 Printed Circuit Board

Each batch of fabricated micro antennas from the MNTC at RAL came on a single slice of silicon. The individual micro antennas were diced to fit a

2.54 mm^2 area and separated from the rest of the silicon wafer. Each micro antenna was subject to a rigours experimental procedure consisting of two experiments over several stages. Given the fragility of each separated micro antenna the handling of the micro antenna in each stage of the experiment had to be done with great care. To help make the handling of each individual micro antenna safe a PCB was fabricated to house each micro antenna throughout each stage of the experimental procedure.

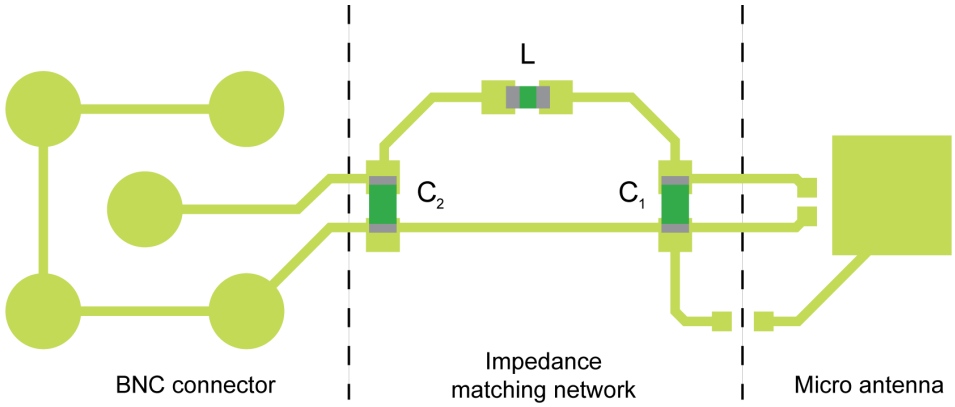

Figure 6.4: A schematic of the PCB to mount a micro antenna.

Figure 6.4 shows the CAD layout of the PCB used to house a single micro antenna from a batch produced by the the MNTC at RAL. There are three sections to the PCB. On the right of the PCB is a 2.54 mm^2 area where the separated micro antenna was mounted to the PCB using a strong adhesive. On the left of the PCB is a space to fit a BNC connector to interface the micro antenna with experimental apparatus. The middle section of the PCB adds the impedance matching network of inductors and capacitors between the micro antenna and the source of the incoming signal.

The impedance matching network includes two parallel capacitors, C_1 and C_2, and a single series inductor, L. For an efficient power transfer of the signal from the source, coming form the BNC connector, to the micro antenna, transmitting the high frequency signal, there needs to be a matched impedance between the source and micro antenna. If the BNC connector is attached to a standard bench-top function generator then the output impedance of that device would be 50Ω. In order for an efficient transfer of

the signal from the function generator into the micro antenna the impedance matching network of components needs to match the impedance of the micro antenna to 50Ω. The impedance analyser, presented in Section 6.4.5 is a standard piece of bench-top lab equipment capable of performing an impedance analysis of an attached component, and provides a recommended set of components for a impedance matching network to shift the tested component to match a 50Ω interface. The data presented in Figure 6.9 illustrates this point.

After the micro antenna was mounted to the PCB an electrical connection between the PCB and the micro antenna's IC was made using a wire bond technique. The wire bonds between the PCB and the mounted micro antenna were even more fragile than the micro antenna occupying a diced 2.54 mm^2 area of silicon.

Including a BNC connector in the PCB was a way to interface the mounted micro antenna with alternative experimental apparatus. The characterisation process of a micro antenna was completed in multiple stages using two experiment. By having a BNC connector to interface the mounted micro antenna with different experimental apparatus made switching between the different stages and experiments of the experimental processes safe.

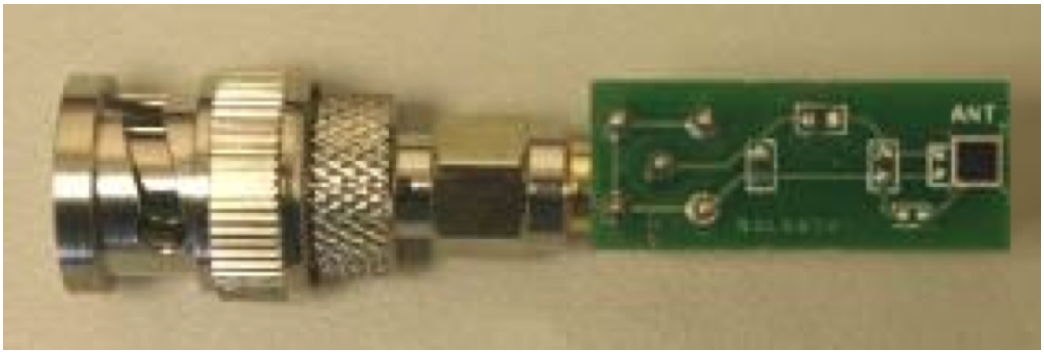

Figure 6.5: The full PCB with, mounted micro antenna to the right, impedance matching network in the centre, and the BNC connector to the left.

Figure 6.5 is a photo of the micro antenna as it was used throughout the experimental process mounted to a PCB. Note that the micro antenna in Figure 6.5 is located to the right of the PCB. This convenient configuration

made handling the delicate micro antenna safe whilst completing the multiple stages of the micro antenna characterisation process.

The following subsections will provide an introduction to some of the more sophisticated lab equipment used to complete this experiment including; a function generator, a spectrum analyser, and an impedance analyser. These instruments were used across two separate experiments to complete a characterisation of the performance of each antenna design under the requirements of the MICS specifications.

6.4.3 Function Generator

Figure 6.6: The HM8134-3 function generator.

The HM8134-3 function generator from HAMEG Instruments GmbH, presented in Figure 6.6, was used to generate a high frequency signal for the micro antenna being characterised. The function generator is capable of producing an output signal between 1 Hz and 1.2 GHz at a power between -127 dBm and 13 dBm. For the purposes of this experiment, to characterise the performance of the fabricated micro antennas for the use with the MICS specification, this piece of lab equipment was adequate.

In addition to the HM8134-3 function generator producing the necessary output signal required for the experiment, this particular piece of hardware was also controllable via a software using an RS-232 interface.

6.4.4 Spectrum Analyser

The HMS3000 spectrum analyser from HAMEG Instruments GmbH, presented in Figure 6.7, was used to measure the received signal transmitted by

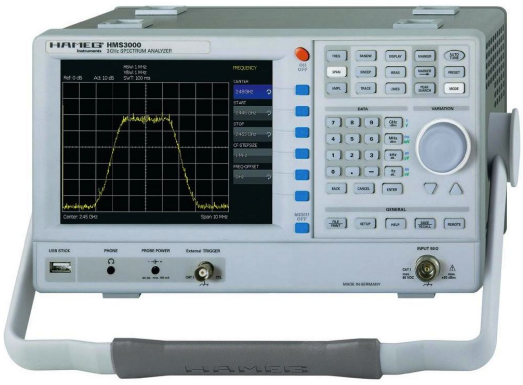

Figure 6.7: The HMS3000 spectrum analyser.

the micro antenna being characterised. This spectrum analyser is capable of measuring the spectrum between 100 kHz and 3 GHz of a signal with an amplitude between −114 dBm and 20 dBm. Thus making this piece of equipment suitable in the characterisation of the fabricated micro antennas.

In addition to the HMS3000 spectrum analyser accurately measuring the received signal transmitted by the micro antenna, this particular piece of hardware was also controllable via a software using a USB interface.

The spectrum analyser has a signal input on the front face. This signal input enabled a BNC connector to attached to the device. Any attached component to the BNC connector of the spectrum analyser was the interface for the source of the high frequency signal under test. For the sake of the experiment where the performance of the custom designed micro antenna was being assessed it was a large free-standing tripod based RF antenna that was used to provide the incoming signal. The large antenna was connected to the spectrum analyser via the BNC connecter, and the measured signal was received via the large antenna.

6.4.5 Impedance Analyser

The E4991A impedance analyser from Agilent Technologies, presented in Figure 6.8, was used to perform a frequency response analysis of the micro antenna being characterised. This impedance analyser is capable of performing a frequency sweep between 1 MHz and 3 GHz. For the purposes of this

Figure 6.8: The E4991A impedance analyser.

experiment, to characterise the performance of the fabricated micro antennas for the use with the MICS specification by testing the micro antennas between 401 MHz and 406 MHz, this piece of lab equipment was suitable.

In addition to the E4991A impedance analyser accurately profiling the frequency responses of the micro antenna, this particular piece of hardware was also controllable via a software using a LAN interface.

6.4.6 Computer Automation

The scientific work necessary to characterise the fabricated micro antennas was slow, time consuming, and methodical work. The experimental process was completed in multiple stages and needed two experiment to accurately measure the performance difference between the three different fabricated antenna designs. As such, to minimise human error in the results recording process of the experiment, computer automation of the lab apparatus was implemented. Wherever possible a single computer running the Linux operating system communicated with the lab apparatus via a number of protocols including; USB, RS-232, and LAN. Communication with the individual apparatus was accomplished using the C programming language and the POSIX API to communicate directly with the hardware devices attached to the computer's operating system. The computer program would either set the input stimulus to the experiment, the signal on the function generator driving the micro antenna under testing, and record the experiment output,

capture the peak amplitude measured by the spectrum analyser operating over a particular range of frequencies. The recorded results were written to a text file and saved for analysis after the experiment was complete. Capturing data in this way minimised the possibility of human error in transcribing a record of the measurements whilst saving the results into a favourable format for later analysis.

6.5 Experiment Procedure

The characterisation of each fabricated micro antenna was a task completed in several stages. The stages towards micro antenna characterisation was achieved with the repeat use of two devised experiments. The first experiment was to assess the impedance matching between the source of the high frequency signal and the micro antenna itself. The second experiment was to assess the performance of the micro antenna in transmitting the high frequency signal over a distance. In this way, from the results found in this process, a comparison could be made between the different designed micro antennas in each fabrication batch.

6.5.1 Experiment 1: Impedance Characterisation

This experiment was completed using the E4991A impedance analyser. The micro antenna was fixed to the front of the E4991A using the BNC connector on the PCB. The impedance analyser was set to sweep between 1 MHz and 700 MHz taking a measurement of the micro antenna's impedance and phase at 1 MHz intervals across the range. The output from the experiment was to produce a plot of the entire range of frequencies as shown in Figure 6.9.

Recall from Figure 6.4 the components L, C_1, and C_2 combine to form the impedance matching network of the micro antenna's PCB. Before the performance analysis of the micro antenna as a transmitter can be started the impedance matching network of PCB must be populated to ensure a maximum transfer of power between the function generator producing the high frequency test signal and the micro antenna transmitting that signal.

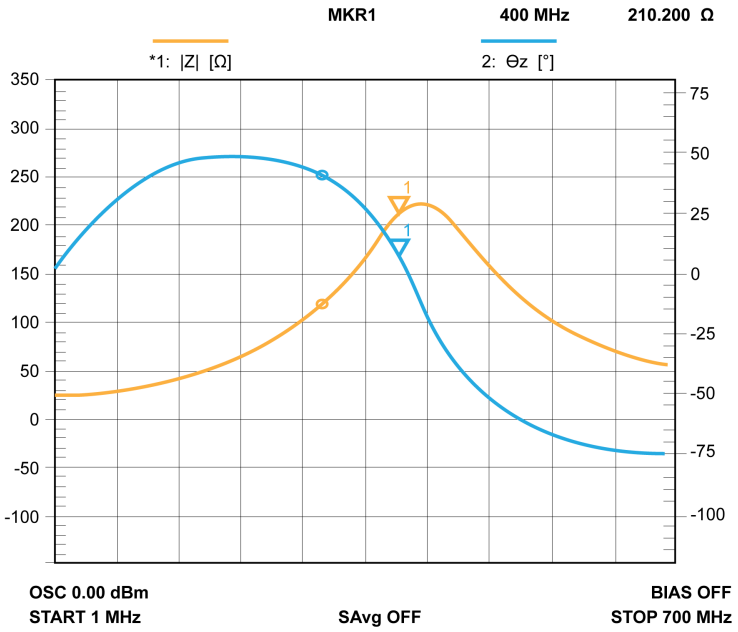

(a) Unmatched antenna plot.

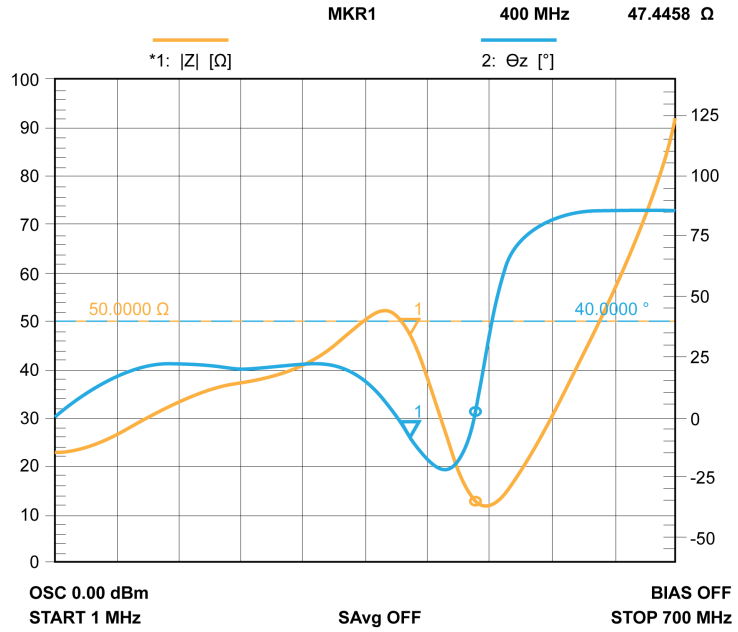

(b) Matched antenna plot.

Figure 6.9: The output from the impedance analysis. Figure 6.9(a) is the impedance profile of the unmatched micro antenna. Figure 6.9(b) is the impedance profile of the matched micro antenna.

Using the E4991A impedance analyser with the unmatched micro antenna an impedance plot was found, as shown in Figure 6.9(a). From this impedance plot an equivalent circuit model was obtained. Using the values of the equivalent circuit model in the PCB's impedance matching network and repeating the same impedance characterisation experiment a new impedance plot was found, as shown in Figure 6.9(b). What is significant about the new impedance plot with the optimised impedance matching components is the shift of the measured impedance amplitude at 400 MHz, from 210.200 Ω in the unmatched configuration to 47.4458 Ω in the matched configuration. Now that the micro antenna has an impedance that is matched to the signal source it is used in the second experiment, the power/distance characterisation, to more reliably characterise the antenna's performance.

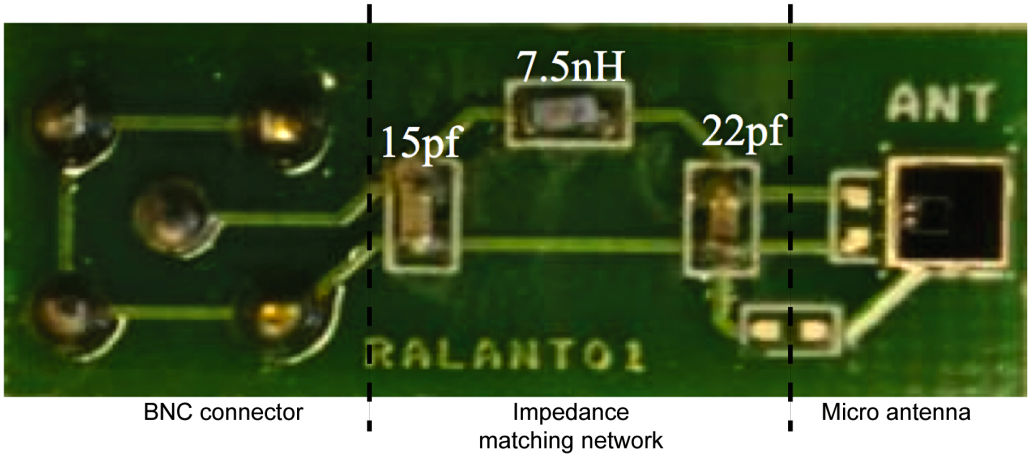

Figure 6.10: The populated impedance matching network with the recommended values of the equivalent circuit.

Figure 6.10 is included for completeness, and it shows a closeup of the PCB with its mounted micro antenna and the recommended components for impedance matching based on the first run of the impedance characterisation experiment.

6.5.2 Experiment 2 - Power/Distance Characterisation

In this experiment a characterisation of the micro antenna's power as a function of distance was completed. Figure 6.11 provides an illustration of the experiment's layout. For this experiment both the HM8134-3 function generator and HMS3000 spectrum analyser were used in conjunction with automation from a Linux computer. The objective was to measure, by feeding a fixed signal produced by the function generator into the micro antenna, at what distance from the micro antenna could a measurable received signal be detected. The spectrum analyser displayed any measurable transmitted signal received by the large antenna.

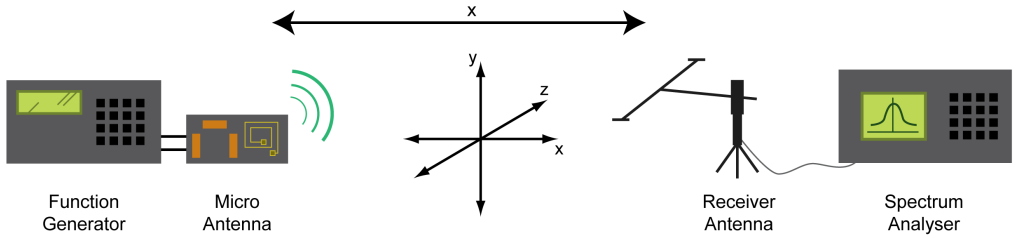

Figure 6.11: Experimental apparatus layout for experiment 2 - RF analysis of the micro antenna.

The measured received signal was taken at four distances from the transmitting micro antenna; 0.5 m, 1.0 m, 1.5 m, and 2.0 m. The received signal was measured at each distance through three axes of orientation for the large antenna and through three aces of orientation for the micro antenna. During the experiment set up, to ensure the received signal was the intended signal, generated in the function generator and transmitted by the micro antenna, the function generator first sends a 400 MHz signal and it is observed as a narrow spike on the spectrum displayed by the spectrum analyser. The function generator is then turned off and the spike on the spectrum analyser drops off to the noise level. This is repeated, with the transmitting signal being adjusted through a number of frequencies. This gives confidence the received signal is the signal being generated by the function generator.

The received signal was measured for the fully shielded, partially shielded, and unshielded micro antenna. Shielding of the micro antenna refers to

concealing part, or all, of the micro antenna using a conductive copper tape in order to determine what portion of the received signal was transmitted through the micro antenna itself and not through wiring or apparatus junctions. This experiment was completed for each micro antenna tested using an input signal of 0 dBm at 400 MHz.

6.5.3 Stages of the Experiment

For this experiment to characterise the micro antennas the experiment had to be completed in a number of stages. The stages included within the characterisation process repeated the use of the two different experiments. Based on the results of the characterisation process for the three tested micro antenna designs a performance comparison between the three designs was used to determine which of the three designs is best suited as the micro antenna for a wireless implantable dosimeter.

The first stage of the experiment was to determine a baseline performance of the fabricated micro antenna. After mounting to a PCB each micro antenna from a fabrication sample a wire bond link between the micro antenna and the PCB was made. For the first stage of the experiment a temporary 0 Ω link was made across the L component of the PCB's impedance matching networking. Without any further changes to the impedance matching networking of the PCB a baseline performance could be established. The PCB housing the micro antenna was fixed to the function generator of the second experiment, the power/distance characterisation experiment. The power/distance characterisation of an antenna was achieved by measuring the amplitude of the received signal at a fixed distances between the transmitting micro antenna and the receiver antenna. The amplitude of the received signal was measured at four distances between the transmitting micro antenna and the receiving large antenna. At each of those four distances the power amplitude of the received signal was measured through the three axes of orientations for the receiver antenna, and through the three axes of orientations for the micro antenna. At each of the four distances the power amplitude of the received signal was measured with the micro antenna being

fully shielded, partially shielded, and unshielded, using a conductive copper tape. This experimental process is illustrated in Figure 6.11. These measurements of the received signal's power combine to form a performance snapshot as a function of distance for the individual micro antenna.

After a baseline of micro antenna performance was established the next stage of the experiment was completed. The impedance matching configuration of the micro antenna was approached. Using the first experiment, the impedance characterisation experiment, an equivalent circuit model was obtained for the unmatched micro antenna. Using the information from the equivalent circuit model the impedance matching network of the PCB was altered and the first experiment was run for a second time on the micro antenna. By repeating the impedance characterisation experiment after the impedance matching network of the PCB was updated the effectiveness of the matching network was recorded. The first experiment performs an analysis of the micro antenna's response to an applied signal between 1 MHz and 700 MHz at 1 MHz intervals. Now that the micro antenna has an improved matching network the response of the micro antenna at the 400 MHz target frequency should be much closer to the ideal 50 Ω.

Replacing the first experiment for the second experiment the RF performance for the the micro antenna is completed for a second time. This was the final stage of the experiment to characterise the micro antenna with the optimum components added to the matching network of the PCB. Again the measured amplitude of the power of the received signal was completed for all four distances through each of the three axes of orientations of the receiver antenna and micro antenna, and for the fully shielded, partially shielded, and unshielded micro antenna setup.

6.6 Experiment Results

This experiment was to determine, between three custom designed micro antennas, the best performing micro antenna operating to the requirements of a medical wireless implantable dosimeter for IVD. To determine which of the three micro antenna designs was best suited for implantable medical

electronics a batch of each micro antenna design was fabricated and tested using a series of rigours and methodical experimental stages incorporating two individual experiments. The results of this experimental procedure are presented here.

Receiver Antenna Orientation	Micro Antenna Orientation	dBm at 0.50 m	dBm at 1.00 m	dBm at 1.50 m	dBm at 2.0 m
Straight Horizontal	Straight	-56.97	-59.90	-67.39	-68.26
Straight Horizontal	Straight 90°	-57.02	-61.53	-67.23	-67.48
Straight Horizontal	Upright	-57.41	-59.29	-67.62	-68.34
Straight Vertical	Straight	-55.48	-61.91	-58.60	-71.69
Straight Vertical	Straight 90°	-55.11	-61.55	-59.25	-70.72
Straight Vertical	Upright	-56.48	-61.19	-58.77	-70.96
Rotated Horizontal	Straight	-57.18	-59.60	-67.62	-62.09
Rotated Horizontal	Straight 90°	-57.02	-59.38	-67.64	-61.98
Rotated Horizontal	Upright	-57.10	-59.80	-67.85	-62.46

Table 6.1: A results sample from the power/distance characterisation experiment for one of the micro antennas from the second batch of fabricated antennas.

Table 6.1 is a sample of measurements taken as part of the power/distance characterisation experiment for one of the micro antennas under test from the second batch of fabricated antennas. This small snapshot of data collected is for the partially shielded antenna configuration only, and includes 36 data points in total. Three times as many data points were measured to also include the same antenna under fully shielded and unshielded conditions. So the total number of data points for the matched micro antenna in the power/distance characterisation experiment is 108. This measurement process was repeated for all three micro antennas that make a sample from a batch of fabricated micro antennas. Therefore an entire sample of micro antennas includes 324 data points for the power/distance characterisation experiment. Including all three fabricated iterations of the micro antenna, and knowing that the power/distance characterisation experiment was completed twice, once before the optimised impedance matching network and once after, in total this experiment accumulated $1,944$ data points to characterise the performance of all tested micro antennas.

	Antenna A				Antenna C				Antenna E			
Distance (m):	0.25	0.50	0.75	1.00	0.25	0.50	0.75	1.00	0.25	0.50	0.75	1.00
Large Ant Straight & Horiz												
Small Ant Straight	-58.52	-58.98	-69.97	-64.27	-55.64	-56.69	-66.82	-61.97	-54.86	-55.14	-65.91	-60.58
Small Ant Straight $-90°$	-57.12	-57.39	-66.97	-63.20	-56.31	-56.50	-66.99	-62.38	-54.05	-54.11	-63.79	-59.79
Small Ant Upright	-55.23	-56.04	-66.48	-62.82	-55.51	-55.97	-65.92	-61.50	-52.94	-53.31	-63.69	-60.13
Large Antenna Straight & Vert												
Small Antenna Straight	-60.12	-65.18	-63.97	-69.06	-59.23	-64.81	-62.80	-68.35	-57.07	-62.42	-60.77	-66.07
Small Antenna Straight $-90°$	-60.88	-65.12	-63.76	-68.91	-57.16	-62.53	-63.16	-70.07	-56.88	-61.48	-60.13	-65.83
Small Antenna Upright	-60.63	-69.30	-66.94	-63.66	-59.71	-68.37	-66.77	-63.24	-58.09	-66.97	-64.75	-61.24
Large Antenna Rotated & Horiz												
Small Antenna Straight	-80.49	-64.34	-70.55	-80.40	-79.84	-62.78	-68.16	-77.04	-77.80	-60.99	-66.70	-75.63
Small Antenna Straight $-90°$	-80.43	-63.76	-69.62	-79.95	-84.24	-62.57	-68.52	-77.51	-77.31	-60.47	-66.49	-77.31
Small Antenna Upright	-78.23	-64.05	-70.02	-74.09	-77.34	-64.04	-70.54	-76.44	-76.77	-61.23	-67.63	-72.97

Table 6.2: Data from power/distance experiment for the first batch of micro antennas in the unshielded arrangement.

	Antenna A				Antenna C				Antenna E			
Distance (m):	0.25	0.50	0.75	1.00	0.25	0.50	0.75	1.00	0.25	0.50	0.75	1.00
Large Ant Straight & Horiz												
Small Ant Straight	-86.66	-85.79	-88.75	-88.28	-61.68	-62.74	-73.19	-67.96	-67.01	-67.78	-78.99	-73.04
Small Ant Straight $-90°$	-85.99	-85.39	-88.58	-88.31	-61.61	-62.20	-73.07	-67.88	-65.92	-66.55	-77.47	-72.30
Small Ant Upright	-76.33	-77.25	-86.27	-82.77	-61.62	-62.28	-73.63	-68.55	-66.36	-67.18	-79.25	-74.61
Large Antenna Straight & Vert												
Small Antenna Straight	-87.06	-88.15	-88.06	-88.81	-64.89	-69.26	-69.61	-73.95	-69.38	-73.39	-73.72	-78.02
Small Antenna Straight $-90°$	-86.97	-88.07	-88.13	-88.78	-63.45	-67.50	-68.82	-74.70	-69.25	-72.91	-73.27	-78.43
Small Antenna Upright	-83.54	-88.73	-84.92	-84.14	-64.28	-72.78	-75.72	-69.12	-69.72	-79.53	-79.70	-74.40
Large Antenna Rotated & Horiz												
Small Antenna Straight	-88.93	-87.82	-88.72	-88.91	-82.23	-69.40	-74.34	-81.77	-85.83	-74.09	-79.06	-85.67
Small Antenna Straight $-90°$	-88.93	-87.80	-88.67	-88.90	-83.86	-69.34	-74.71	-81.39	-85.89	-73.87	-78.75	-85.73
Small Antenna Upright	-88.81	-86.41	-86.18	-88.46	-81.14	-71.04	-76.76	-81.17	-85.82	-76.26	-81.61	-84.49

Table 6.3: Data from power/distance experiment for the first batch of micro antennas in the partially shielded arrangement.

	Antenna A				Antenna C				Antenna I			
Distance (m):	0.5	1.0	1.5	2.0	0.5	1.0	1.5	2.0	0.5	1.0	1.5	2.0
Large Ant Straight & Horiz												
Small Ant Straight	-64.94	-68.82	-73.86	-66.58	-64.85	-69.06	-76.03	-67.61	-65.50	-68.92	-75.18	-67.06
Small Ant Straight $-90°$	-79.82	-71.44	-78.85	-70.31	-83.35	-72.58	-81.08	-71.48	-77.22	-71.14	-78.82	-70.37
Small Ant Upright	-68.98	-67.79	-76.91	-70.89	-68.53	-69.82	-77.77	-70.94	-69.52	-68.03	-77.16	-71.58
Large Antenna Straight & Vert												
Small Antenna Straight	-62.92	-64.15	-64.12	-82.96	-63.17	-64.75	-64.34	-83.47	-62.58	-64.84	-64.34	-80.96
Small Antenna Straight $-90°$	-66.38	-65.96	-65.97	-83.19	-66.28	-67.03	-65.08	-85.98	-66.11	-66.19	-65.61	-82.11
Small Antenna Upright	-67.08	-70.26	-70.33	-82.05	-66.78	-69.82	-69.98	-80.75	-66.81	-70.33	-69.92	-81.33
Large Antenna Rotated & Horiz												
Small Antenna Straight	-70.35	-69.07	-73.12	-70.75	-70.92	-71.91	-73.42	-72.24	-71.39	-71.69	-74.42	-71.64
Small Antenna Straight $-90°$	-67.11	-68.12	-71.88	-70.22	-67.25	-69.61	-73.02	-71.27	-67.57	-69.35	-72.18	-59.65
Small Antenna Upright	-71.10	-72.78	-77.98	-77.19	-71.56	-74.16	-79.45	-77.46	-71.42	-73.70	-78.22	-78.08

Table 6.4: Data from power/distance experiment for the second batch of micro antennas in the unshielded arrangement.

	Antenna A				Antenna C				Antenna I			
Distance (m):	0.5	1.0	1.5	2.0	0.5	1.0	1.5	2.0	0.5	1.0	1.5	2.0
Large Ant Straight & Horiz												
Small Ant Straight	-56.97	-59.90	-67.39	-68.26	-56.10	-58.78	-66.66	-67.82	-65.25	-59.24	-71.68	-66.30
Small Ant Straight $-90°$	-57.02	-61.53	-67.23	-67.48	-55.75	-58.77	-67.11	-67.99	-66.20	-61.68	-69.64	-66.57
Small Ant Upright	-57.41	-59.29	-67.62	-68.34	-56.18	-59.06	-67.77	-67.50	-65.74	-58.93	-67.85	-69.57
Large Antenna Straight & Vert												
Small Antenna Straight	-55.48	-61.91	-58.60	-71.69	-55.47	-62.05	-59.47	-71.61	-55.94	-58.95	-58.58	-69.15
Small Antenna Straight $-90°$	-55.11	-61.55	-59.25	-70.72	-53.89	-61.27	-59.37	-71.65	-55.65	-59.48	-58.88	-70.58
Small Antenna Upright	-56.48	-61.19	-58.77	-70.96	-56.13	-59.64	-58.81	-70.73	-55.69	-59.90	-59.00	-68.94
Large Antenna Rotated & Horiz												
Small Antenna Straight	-57.18	-59.60	-67.62	-62.09	-57.84	-59.59	-67.69	-62.98	-55.58	-59.61	-68.17	-64.41
Small Antenna Straight $-90°$	-57.02	-59.38	-67.64	-61.98	-52.51	-59.35	-67.90	-62.10	-55.37	-60.25	-68.93	-65.61
Small Antenna Upright	-57.10	-59.80	-67.85	-62.46	-57.49	-59.45	-67.35	-62.13	-56.17	-59.84	-68.26	-63.10

Table 6.5: Data from power/distance experiment for the second batch of micro antennas in the partially shielded arrangement.

	Antenna A				Antenna B				Antenna E			
Distance (m):	0.5	1.0	1.5	2.0	0.5	1.0	1.5	2.0	0.5	1.0	1.5	2.0
Large Ant Straight & Horiz												
Small Ant Straight	-63.48	-66.98	-65.90	-60.36	-67.08	-66.47	-66.06	-61.04	-63.60	-65.83	-66.11	-60.80
Small Ant Straight $-90°$	-63.66	-68.07	-70.55	-65.88	-53.64	-68.39	-70.69	-66.77	-63.36	-68.10	-69.94	-66.01
Small Ant Upright	-71.86	-66.25	-68.23	-65.64	-71.93	-65.14	-68.05	-65.59	-72.56	-65.25	-68.49	-65.91
Large Antenna Straight & Vert												
Small Antenna Straight	-58.71	-59.25	-59.67	-77.36	-57.90	-59.73	-59.79	-78.87	-58.81	-59.89	-60.91	-77.90
Small Antenna Straight $-90°$	-68.47	-62.86	-60.81	-84.76	-64.97	-62.77	-60.66	-89.53	-68.87	-63.45	-60.34	-88.59
Small Antenna Upright	-66.97	-68.41	-85.40	-66.32	-67.34	-68.92	-80.17	-66.06	-66.91	-68.59	-81.53	
Large Antenna Rotated & Horiz												
Small Antenna Straight	-62.56	-63.27	-64.94	-66.45	-59.41	-63.61	-63.55	-65.90	-61.90	-63.68	-64.94	-66.50
Small Antenna Straight $-90°$	-59.62	-60.36	-63.55	-64.15	-59.29	-61.10	-64.18	-64.51	-59.67	-60.60	-63.37	-63.96
Small Antenna Upright	-64.15	-64.78	-68.38	-71.75	-64.35	-64.78	-68.22	-71.31	-63.89	-64.88	-67.82	-71.60

Table 6.6: Data from power/distance experiment for the third batch of micro antennas in the unshielded arrangement.

	Antenna A				Antenna B				Antenna E			
Distance (m):	0.5	1.0	1.5	2.0	0.5	1.0	1.5	2.0	0.5	1.0	1.5	2.0
Large Ant Straight & Horiz												
Small Ant Straight	-60.74	-66.94	-62.98	-61.15	-67.27	-67.83	-76.45	-73.48	-58.31	-66.35	-61.80	-66.40
Small Ant Straight $-90°$	-48.59	-64.75	-70.93	-70.28	-74.06	-69.34	-78.83	-79.05	-56.46	-61.98	-70.75	-67.26
Small Ant Upright	-65.66	-70.82	-65.90	-65.63	-75.33	-72.65	-78.38	-77.86	-64.09	-69.62	-64.99	-63.29
Large Antenna Straight & Vert												
Small Antenna Straight	-60.71	-58.71	-61.39	-89.71	-69.34	-60.15	-67.63	-89.22	-75.25	-56.57	-59.55	-73.76
Small Antenna Straight $-90°$	-70.81	-63.31	-62.32	-92.29	-75.25	-64.16	-74.66	-93.45	-66.24	-61.54	-60.63	-73.76
Small Antenna Upright	-70.86	-66.06	-66.92	-77.33	-71.07	-74.17	-70.33	-91.72	-74.84	-64.93	-65.83	-92.33
Large Antenna Rotated & Horiz												
Small Antenna Straight	-64.25	-62.20	-61.50	-63.61	-65.52	-65.50	-81.54	-75.58	-62.26	-74.57	-77.70	-65.27
Small Antenna Straight $-90°$	-66.15	-59.19	-77.28	-61.83	-67.98	-57.29	-78.73	-75.67	-62.62	-72.48	-74.79	-64.49
Small Antenna Upright	-59.47	-66.09	-67.52	-69.88	-59.47	-75.93	-76.09	-84.14	-59.88	-81.65	-64.49	-67.20

Table 6.7: Data from power/distance experiment for the third batch of micro antennas in the partially shielded arrangement.

A comprehensive summary of the data acquired by testing the performance of the three batches of micro antenna is presented in, Table 6.2, Table 6.3, Table 6.4, Table 6.5, Table 6.6, and Table 6.7. For each of the three batches of micro antennas that were tested the data presented gives the measured values for both the unshielded and partially shielded configuration in each orientation of both the micro antenna and the large antenna. This data takes a single data point for each distance and orientation. There is scope for error within the measurement as more data points at each distance and orientation wasn't taken. However, the data dose provide a guideline on the profile of transmitted signal by the micro antenna.

To make better sense of the data recorded a statistical approximations was used across the entire set of results for the power/distance characterisation experiment. The performance of each sample of micro antennas was averaged across all orientations of the experiment's data to produce a result that is a sample equivalent micro antenna dataset.

	dBm at 0.25 m	dBm at 0.50 m	dBm at 0.75 m	dBm at 1.00 m	dBm at 1.50 m	dBm at 2.00 m
Batch #1	-76.41	-75.32	-79.63	-80.02		
Batch #2		-57.14		-60.00	-65.00	-67.14
Batch #3		-65.65		-66.47	-69.63	-75.02
$\sigma_{batch\#1}$	0.98	0.44	0.73	1.20		
$\sigma_{batch\#2}$		0.57		0.34	0.17	0.05
$\sigma_{batch\#3}$		0.98		4.21	2.21	1.76

Table 6.8: This dataset is the statistically approximated fabrication sample equivalent dataset for the micro antennas tested using the power/distance characterisation experiment.

Table 6.8 shows the sample equivalent micro antenna dataset used to quantify the relative performance between all three micro antenna designs. It is worth noting that only after the characterisation of the first batch of micro antennas was it decided the range of tested distances for the micro antenna should change from up to 1 m to a range up to 2 m. At 2 m it is a more realistic distance an implantable dosimeter would operate from when a medical physicist is interrogating the patient's dosimeter. As such the dataset

in Table 6.8 measures the performance of the first batch of micro antennas up to 1 m distance only. Note also the lower half of Table 6.8 includes the calculated standard deviation (σ) for each fabrication sample equivalent micro antenna, where σ are the included $\pm$ error bars in the illustration of the micro antennas' relative performance in Figure 6.12.

Figure 6.12 highlights the performance difference between all three micro antennas designed and fabricated. The data used to produced Figure 6.12 is take from the fabrication sample equivalent micro antenna dataset in Table 6.8. Notice that for the first batch of micro antennas the plot in Figure 6.12 is up to a range of 1 m only. The change to characterise the performance of the fabricated micro antennas up to 1 m came after the first batch of micro antennas was fabricated. The y-axis of the plot in Figure 6.12 increments on the negative scale so the strongest measured signal, in dBm, moves up the y-axis. The error bars on each data point are taken as the standard deviation from the average of three micro antennas in a fabrication's sample. The larger the standard deviation the greater the variance in the data of that batch of antennas. The noise floor of the testing environment produced a fixed amplitude static at -90 dBm across all distances.

From Figure 6.12 the equation for the line of best fit for the three batches is given as:

$$y = -2.592x - 51.304 \tag{6.1}$$

$$y = -2.192x - 59.878 \tag{6.2}$$

$$y = -1514x - 74.060 \tag{6.3}$$

These equations are given in order. Equation 6.1 is for the line of best fit for batch 2 of micro antennas, Equation 6.2 is for the line of best fit for third batch of micro antennas tested, and Equation 6.3 is for the line of best fit for the first batch of characterised micro antenna design. This is the expected order of performance based on the predicted outcome given

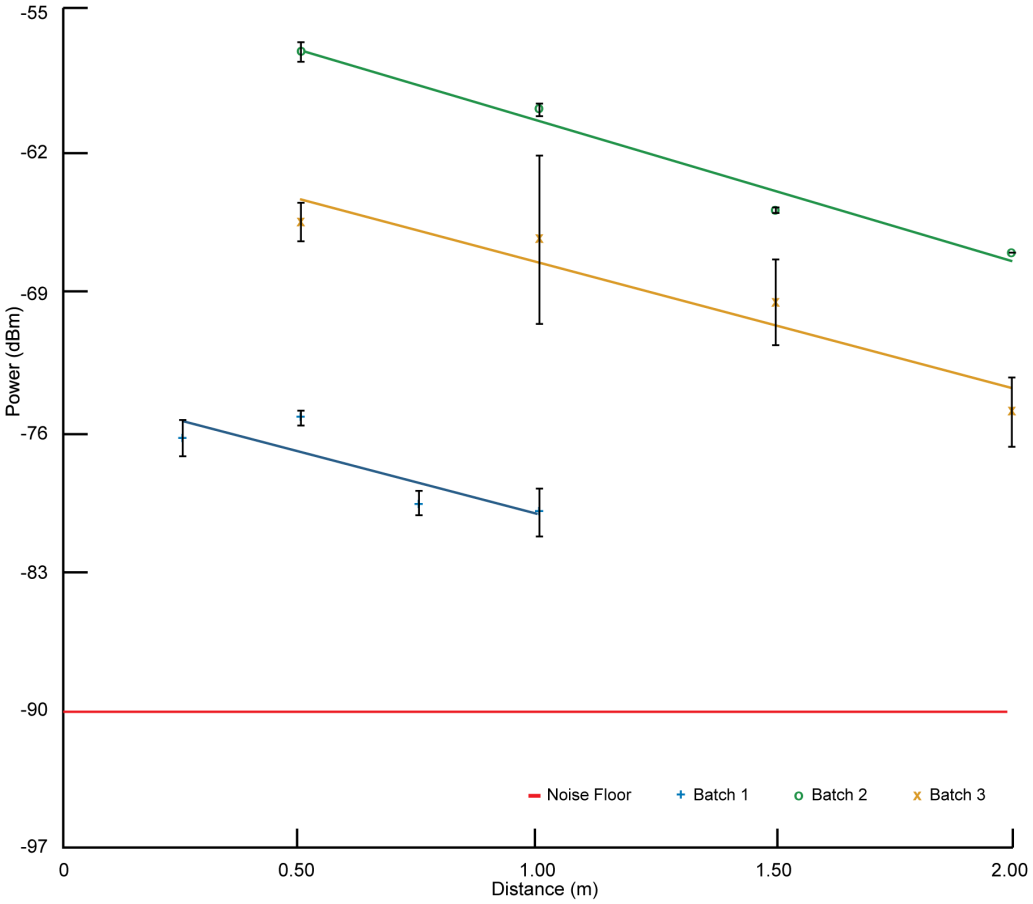

Figure 6.12: This plots illustrates the relative performance difference between all three fabricated micro antenna design types.

through the simulation work completed before the experiment was carried out. Setting $x = 1$ for each of the three equations an estimate for the dBm, y, can be found. A comparison between the three vales of y when $x = 1$ will give a rough guide as to the actual performance difference between the three mire antenna designs. For the second batch of micro antennas, with $x = 1$, $y = -53.90$ dBm, for the third batch of micro antennas, with $x = 1$, $y = -62.07$ dBm, and for the second batch of micro antennas, with $x = 1$, $y = -75.57$ dBm. From this data it is clear that the second batch of micro antennas has outperformed all other micro antenna designs.

6.7 Experiment Conclusion

This experiment was to measure the performance difference between three alternative micro antenna designs, and their suitability for wireless communication in medical electronic devices, specifically as an integrated micro antenna to be used with an implantable dosimeter for IVD. In this section the experimental conclusions are presented.

The broad aim of the experiment was to determine the performance difference between the single-loop and multi-loop design approach for the micro antenna. Rigours testing of all fabricated micro antennas was completed using a multiple stage dual experiment procedure. The results from testing two different types of micro antenna, two single-loop and one multi-loop, found the refined single-loop micro antenna from the second batch of fabricated micro antennas to be the best performing micro antenna from all three fabricated micro antenna designs.

The process of characterising the design of each micro antenna was accomplished by implementing an experiment that determined the performance profile of each micro antenna by meticulously recording the measured signal at fixed distances and with all possible micro antenna and receiver antenna orientations. Recording a performance profile over distance through all major antenna axes of orientation was an important experiment objective.

A spectrum analyser is a remarkably sensitive and expensive piece of equipment. It is designed for lab use, and can locally perform a variety

of sophisticated mathematical operations on received spectrum. It also has a plethora of I/O to enable data acquisition. However, for the sake of a bespoke solution in the application of a medical dosimetry, a custom analyser could be used in place of the E4991A from Agilent Technologies. In this study a custom analyser was not investigated. Further work would be needed to design and build a signal analyser for the use as a rudimentary signal analyser. Any such customer signal analyser would be built as a cost effective alternative to an expensive spectrum analyser.

From the function generator the signal driving all micro antennas under test was a 0 dBm high frequency signal at 400 MHz. The results from this experiment found the second batch of single-loop micro antennas to be the best performing micro antenna design. At the maximum tested distance of 2 m the estimated signal for the statistically calculated equivalent micro antenna was almost -67 dBm. At 0 dBm the signal's power is 1 mW, and at -60 dBm the signal's power is 1 nW. Therefore the best performing micro antenna design produced a signal at the furthest distance of 2 m at three orders of magnitude less than the signal driving the micro antenna. By any conventional antenna design this level of efficiency would be unacceptable. However the micro antenna application of implantable medical electronics means the experiment was only aiming to prove the micro antenna design could transmit a measurable signal, above the noise floor, at the maximum experimental range. The noise floor of the experimental environment was at -90 dBm where the power of the signal at this range is 1 pW. Thus, despite the seemingly poor performance of the micro antenna's design, the measured signal at the maximum 2 m distance was still three orders of magnitude greater than the noise floor. Therefore the design of the micro antenna from the second batch of fabricated micro antennas can perform as a transmitting antenna for the application of a new enhanced implantable wireless dosimeter for IVD.

For this experiment the MICS specification provided a rough guideline on a suitable performance requirement that should be used to characterise the design of the fabricated micro antennas. The MICS specification defines the 401 MHz to 406 MHz frequency range as the reserved range for medical

devices, and states the maximum transmit power should be low with an equivalent radiated power of ≤ 25 μW, and states the maximum bandwidth used at any one time should not exceed 100 kHz. This experiment did not directly implement the MICS specification with a high frequency signal at 400 MHz driving the micro antenna.

6.8 Further Work

Despite the promising findings of this early work into antenna design for an implantable dosimeter it is understood that the results of this study may have greater implications should the study be repeated to more strictly adhere to the MICS specification. Given the level of interest around wireless medical devices passively providing extensive biotelemetry on patient health the value of a functional micro antenna that can be directly integrated into the electronic circuit of any medical device is important.

In addition, to compliment the findings in this initial study, the experimental method should be revised to include an integrated circuit where an improved micro antenna is coupled directly to a high frequency oscillator with the necessary impedance matching network. In this way the measured signal from the micro antenna under test can more reliably be explained by the transmission from the micro antenna itself, instead of any signal potentially leaking from the experiment's apparatus.

As with any experiment where the technology being characterised is the result of a mathematical model abstracted into a physical prototype there is a latency between a change in the model and the implemented prototype due to the fabrication process. The smaller and more sophisticated the integrated circuit needed the more expensive the fabrication process becomes. As such a field of research like micro antenna design is an iterative process towards progress. In this sense the results presented here are promising, but only a step towards a more refined solution.

6.9 Summary

This chapter has presented an experiment to evaluate the performance difference between three custom designed micro antennas where the best performing micro antenna would be used as part of an integrated circuited that requires wireless communication.

This chapter has presented the experimental method where a sample of three micro antennas from each batch of fabricated micro antennas was characterised to determine their performance where the amplitude of a received signal transmitted by the micro antenna was measured as a function of distance.

This chapter has presented the results of the experiment that characterised the performance of the designed micro antennas including a strong consideration of the MICS specification as a baseline for necessary operating requirements. As such each of the micro antennas designed were tested up to a distance of 2 m and looking to record a received signal above the noise floor with the micro antenna being driven with a low power 0 dBm signal at 400 MHz produced by the function generator.

This chapter has presented the conclusions of the experiment stating the best performing micro antenna design can be recommended for use in an integrated circuit forming part of a new enhanced implantable dosimeter for IVD.

Chapter 7

Conclusion

This chapter summarises the main findings of the two studies carried out for this thesis, includes a general discussion to consider these results in the wider context of existing knowledge, and closes with an outline of further work currently underway to push this project forward.

7.1 Achievements

The objective of the project is to design and build a new type of dosimeter, an implantable wireless dosimeter to provide real-time measurement of the absorbed dose of ionising radiation. The dosimeter would be built from a single integrated circuit containing each of the four expected technology components necessary for a new enhanced dosimeter design, including; a silicon based dose measurement component, control electronics, an antenna for wireless communication, and a power source. This new enhanced dosimeter will act as an improved quality assurance technology for radiotherapy, providing confirmation of the absorbed dose of ionising radiation at the target volume of a patient receiving treatment. This thesis presents the results of work completed to address two of the four expected technology components of this new enhanced dosimeter, including; an experiment to assess the suitability of the floating gate metal oxide field effective transistor as a silicon based electronic component capable of measuring exposure to ionising radi-

ation, and an experiment to determine the best performing micro antenna design for an implantable medical electronic device.

7.1.1 Transistor Experiment

In the transistor experiment the electrical response to exposure of the floating gate metal oxide field effective transistor to a source of ionising radiation was recorded and analysed. It was found that the response of this type of transistor when exposed to ionising radiation is predictable, accurately measurable, and repeatable. The charge stored on the floating-gate of the device under test was programmable and it was found that the greater the density of stored charge on the transistor's float-gate the more sensitive the device was to radiation exposure. The source of ionising radiation used for this experiment produced γ radiation with energy typical of the electromagnetic waves used in radiotherapy. As such it is inferred the floating gate metal oxide field effective transistor is a suitable electronic component to measure the dosage of ionising radiation and could be used as part of a new enhanced implantable dosimeter for in-vivo dosimetry.

7.1.2 Micro Antenna Experiment

For the micro antenna experiment the performance difference between three alternative micro antenna designs was assessed to determine which micro antenna design is most suitable for the application of implantable medical electronics. The unique operating environment of medical electronics requires a low power solution to operate over a short distance and with low bandwidth. Therefore, in the assessment of the three different micro antenna designs, it was not the antenna's transmission efficiency being characterised but instead the clarity of the received signal through all test distances. This experiment found the refined single-loop micro antenna design from the second fabricated batch to be the best performing of the three micro antenna designs, and that this antenna could be used as part of a new enhanced implantable dosimeter for in-vivo dosimetry.

7.2 General Discussion

This section is a general discussion, it draws together the results from the two results chapters, and discusses the results in the wider context of existing knowledge.

The transistor and micro antenna work combine to form two of the four blocks necessary to build an implantable dosimeter. Simply including as little as a VCO, and thin film micro-batteries, would be enough to build a complete integrated dosimeter.

From the results presented in Chapter 5, and Chapter 6, both the micro antenna and FGMOSFET have been found to be suitable components for the application of in-vivo dosimetry. The completed transistor work is a compliment to the published work of Tarr et al. [91], and the micro antenna work is a compliment to the work of Kim et al. [130]. The suggested union of these two elements of research as part of an integrated implacable dosimeter are a compliment to the work of Shamim et al. [133].

7.3 Further Work

In April 2011 the success of a grant proposal was confirmed and the award of $£250,000$ form the Challenge Led Applied Systems Programme, funded by the Science and Technology Facilities Council, had been allocated to take this project onto the next stage. The grant includes funding for the design and fabrication of a custom floating-gate transistor optimised for the application of in-vivo dosimetry. This device has since been fabricated by the Tower-Jazz group of Tower Semiconductor Ltd., a specialist silicon foundry based in Migdal HaEmek, Israel. Application for this research grant was made in conjunction with the The Oxford Cancer Centre of Churchill Hospital, Oxford, and in collaboration with this specialist oncology clinic the new custom transistors will be characterised using an NHS radiotherapy linac. It is therefore an aspiration of this project to improve on the results of the transistor characterisation presented within this thesis as a stepping stone towards a complete integrated implantable dosimeter for in-vivo dosimetry.

7.3.1 Transistor Technology

The size of an optimised floating gate metal oxide field effective transistor is a critical design consideration in future iterations of transistor technology for in-vivo dosimetry. To ensure the best use of the available silicon in the proposed dosimeter a sub-millimetre transistor with a proportionately large floating-gate surface area will improve the resolution of the device as a dose measurement component. Any further testing of the performance of the floating-gate transistor as a dose measurement component should test the dosimeter up to a 100 Gy dose, thus ensuring the transistor is a robust and predictable device under the most aggressive of radiotherapy treatments. In addition, the floating-gate transistor should be characterised across the spectrum of ionising radiation practically used in radiotherapy, from 50 KeV to 25 MeV. However the future of radiotherapy may not be in X-ray/γ-ray based treatment, but instead with accelerated particles as the source of ionising radiation. It would therefore be prudent to explore the response of the floating-gate transistor under proton and heavier ion exposure.

7.3.2 Micro Antenna Technology

The next stage of research for the micro antenna is to integrate the micro antenna on the same piece of silicon as the control electronics where a high frequency carrier, meeting the MICS specification, could be produced. Only by repeating the power/distance experiment to characterise the performance of the micro antenna where, integrated on the same circuit, it is being driven directly by a high frequency carrier can it be confirmed that the measured received signal is being transmitted by the prototype wireless solution.

7.3.3 Control Electronics Technology

For the proposed dosimeter, a first step solution for the control electronics technology is to characterise the performance of a voltage-controlled oscillator. A voltage-controlled oscillator is a device that has a high frequency analogue output, and the oscillating frequency of the output relates to the

applied signal to its low frequency analogue input. In addition to this the voltage-controlled oscillator can be built as part of an integrated circuit. Therefore the voltage-controlled oscillator could potentially be designed such that it forms part of the integrated circuit for the proposed dosimeter. The high frequency output oscillation drives the carrier frequency feeding the micro antenna and the low frequency input signal is taken directly from the shifting V_{Th} bias of the floating-gate transistor. This simple three stage solution could implement a rudimentary dosimeter where the ionising radiation that causes a V_{Th} shift on the floating-gate transistor would alter the output frequency of the voltage-controlled oscillator, thus altering the transmitting frequency of the micro antenna.

Bibliography

[1] Health statistics quarterly. Technical Report 43, Office for National Statistics, September 2009.

[2] P. Boyle, P. Autier, H. Bartelink, J. Baselga, P. Boffetta, J. Burn, H. J. G. Burns, L. Christensen, L. Denis, M. Dicato, V. Diehl, R. Doll, S. Franceschi, C. R. Gillis, N. Gray, L. Griciute, A. Hackshaw, M. Kasler, M. Kogevinas, S. Kvinnsland, C. La Vecchia, F. Levi, J. G. McVie, P. Maisonneuve, J. M. Martin-Moreno, J. Newton Bishop, F. Oleari, P. Perrin, M. Quinn, M. Richards, U. Ringborg, C. Scully, E. Siracka, H. Storm, M. Tubiana, T. Tursz, U. Veronesi, N. Wald, W. Weber, D. G. Zaridze, W. Zatonski, and H. zur Hausen. European code against cancer and scientific justification: third version. *Annals of Oncology*, 14(7):973–1005, 2003.

[3] Healthy lives, healthy people: Our strategy for public health in england. Technical Report , Department of Health, November 2010.

[4] Bruce Alberts, Alexander Johnson, Julian Lewis, Martin Raff, Keith Roberts, and Peter Walter. *Molecular Biology of the Cell*. Garland Science, 5th edition, 2007.

[5] Charles Darwin. *On the Origin of Species by Means of Natural Selection Or The Preservation of Favoured Races in the Struggle for Life*. John Murray, 1st edition, 1859.

[6] R. A. Fisher and Henry Bennett. *The Genetical Theory of Natural Selection*. Oxford University Press, 3rd edition, 1999.

[7] Hermann Joseph Muller. The production of mutations by x-rays. *Proceedings of the National Academy of Sciences of the United States of America*, 14(9):714–726, September 1928.

[8] R. Calandrino, A. Del Maschio, G.M. Cattaneo, and I. Castiglioni. Imaging in radiotherapy. *Nuclear Instruments and Methods in Physics Research Section A: Accelerators, Spectrometers, Detectors and Associated Equipment*, 608(s1):11–14, 2009.

[9] J. R. Williams and D. I. Thwaites. *Radiotherapy Physics*. Oxford University Press, 1st edition, 1993.

[10] M. Kara Bucci, Alison Bevan, and Mack Roach. Advances in radiation therapy: Conventional to 3d, to imrt, to 4d, and beyond. *CA: A Cancer Journal for Clinicians*, 55(2):117–134, 2005.

[11] Ching-Chong Jack Yang, Adam Raben, and Don Carlson. Imrt: high-definition radiation therapy in a community hospital. *Medical Dosimetry*, 26(2):215–226, 2001.

[12] Laura A. Dawson and Michael B. Sharpe. Image-guided radiotherapy: rationale, benefits, and limitations. *The Lancet Oncology*, 7(10):848–858, 2006.

[13] Kenneth R. Hogstrom and Peter R. Almond. Review of electron beam therapy physics. *Physics in Medicine and Biology*, 51(13):455–489, 2006.

[14] Bertil Damato, Andrzej Kacperek, Mona Chopra, Ian R. Campbell, and R. Douglas Errington. Proton beam radiotherapy of choroidal melanoma: The liverpool-clatterbridge experience. *International Journal of Radiation Oncology Biology Physics*, 62(5):1405–1411, 2005.

[15] Koji Noda, Takuji Furukawa, Takashi Fujisawa, Yoshiyuki Iwata, Tatsuaki Kanai, Mitsutaka Kanazawa, Atsushi Kitagawa, Masataka Komori, Shinichi Minohara, Takeshi Murakami, Masayuki Muramatsu, Shinji Sato, Yuka Takei, Mutsumi Tashiro, Masami Torikoshi, Satoru

Yamada, and Ken Yusa. New accelerator facility for carbon-ion cancer-therapy. *Journal of Radiation Research*, 48(sA):43–54, 2007.

[16] Geoff Delaney, Susannah Jacob, Carolyn Featherstone, and Michael Barton. The role of radiotherapy in cancer treatment: estimating optimal utilization from a review of evidence-based clinical guidelines. *Cancer*, 104(6):1129–1137, September 2005.

[17] Sara C. Erridge, Carrie Featherstone, Ruth Chalmers, Jillian Campbell, Diane Stockton, and Roger Black. What will be the radiotherapy machine capacity required for optimal delivery of radiotherapy in scotland in 2015? *European Journal of Cancer*, 43(12):1802–1809, 2007.

[18] Radiotherapy: developing a world class service for england. Technical report, Department of Health, May 2007.

[19] Towards safer radiotherapy. Technical Report 81, The Royal College of Radiologists, July 2008.

[20] Jan Erik Frödin, Egon Jonsson, Torgil Möller, and Lars Werkö. Radiotherapy in sweden: A study of present use in relation to the literature and an estimate of future trends. *Acta Oncologica*, 35(8):967–979, 1996.

[21] Liam Donaldson. Reducing harm from radiotherapy. *British Medical Journal*, 334(7588):272, 2007.

[22] On the state of public health: Annual report of the chief medical officer 2006. Technical report, Department of Health, July 2007.

[23] Radiotherapy risk profile. Technical report, World Health Organization, 2008.

[24] Physical aspects of quality assurance in radiation therapy. Technical Report 13, American Association of Physicists in Medicine, 1984.

[25] A. Brahme, J. Chavaudra, T. Landberg, E. McCullough, F. Nusslin, J. E. Rawlinson, G. Svensson, and H. Svensson. Accuracy require-

ments and quality assurance of external beam therapy with photons and electrons. *Acta Oncologica*, 27(s1), 1988.

[26] *Quality Assurance in Radiotherapy.* World Health Organization, 1988.

[27] B. J. Mijnheer. Quality assurance in radiotherapy: Physical and tecenical aspects. *International Journal for Quality in Health Care*, 4(1):9–18, 1992.

[28] Anders Brahme. The need for accurate target and dose specifications in conventional and conformal radiation therapy: An introduction. *Acta Oncologica*, 36(8):789–792, 1997.

[29] P. Aaltonen, A. Brahme, I. Lax, S. Levernes, I. Naslund, J. B. Reitan, and I. Turesson. Specification of dose delivery in radiation therapy. recommendation by the nordic association of clinical physics (nacp). *Acta Oncologica*, 36(s10):1–32, 1998.

[30] *ICRP Publication 86: Prevention of Accidents to Patients Undergoing Radiation Therapy.* Elsevier, 2001.

[31] *Balancing Costs and Benefits of Checking in Radiotherapy.* IPEM, 2006.

[32] Robert Appleyard. A survey of in vivo diode dosimetry in the uk. *Journal of Radiotherapy in Practice*, 1(2):73–82, 1999.

[33] C. R. Edwards, E. Hamer, P. J. Mountford, and A. J. Moloney. An update survey of uk in vivo radiotherapy dosimetry practice. *British Institute of Radiology*, 80(960):1011–1014, 2007.

[34] Second report of the independent inquiry into the conduct of isocentric radiotherapy at the north staffordshire royal infirmary. Technical report, West Midlands Regional Health Authority, March 1994.

[35] Independent review of the circumstances surrounding a serious adverse incident that occurred in the cookridge hospital. Technical report, Redacted copy obtained under the Freedom of Information Act 2001.

[36] Unintended overexposure of patient lisa norris during radiotherapy treatment at the beatson oncology centre, glasgow in january 2006. Technical report, Scottish Executive, May 2007.

[37] M. V. Williams and A. McKenzie. Can we afford not to implement in vivo dosimetry? *British Institute of Radiology*, 81(969):681–684, July 2008.

[38] R. I. MacKay and P. C. Williams. The cost effectiveness of in vivo dosimetry is not proven. *British Journal of Radiology*, 82(976):265–266, 2009.

[39] Max Planck. On the law of distribution of energy in the normal spectrum. *Annalen der Physik*, 4:553–563, 1901.

[40] November 2011.

[41] J. F. R. Kerr, A. H. Wyllie, and A. R. Currie. Apoptosis: A basic biological phenomenon with wide-ranging implications in tissue kinetics. *British Journal of Cancer*, 26(4):239–257, August 1972.

[42] D. Schulte-Frohlinde. Early events in the radiation biology of e. coli. *International Journal of Radiation Applications and Instrumentation. Part C. Radiation Physics and Chemistry*, 34(1):173–183, 1989.

[43] Arthur Holly Compton. A quantum theory of the scattering of x-rays by light elements. *The Physical Review*, 21(5):483–502, May 1923.

[44] Keith J. Laidler and Kurt E. Shuler. Elementary reactions in the gas phase involving excited electronic states. *Chemical Reviews*, 48(2):153–224, April 1951.

[45] Robert L. Platzman. Superexcited states of molecules. *Radiation Research*, 17(3):419–425, September 1962.

[46] U. Fano. Platzman's analysis of the delivery of radiation energy to molecules. *Radiation Research*, 64(2):217–232, November 1975.

[47] Eric J. Hall. *Radiobiology for the Radiologist*. Lippincott Williams and Wilkins, 4th edition, 1994.

[48] Helen Wieseman and Barry Halliwell. Damage to dna by reactive oxygen and nitrogen species: role in inflammatory disease and progression to cancer. *Biochemical Journal*, 313(1):17–29, January 1996.

[49] George Gordon Steel. *Basic Clinical Radiobiology*. Hodder Arnold, 3rd edition, 2002.

[50] C. Potten and J. Wilson. *Apoptosis: The Life and Death of Cells*. Cambridge University Press, 2004.

[51] A. Brahme. Dosimetric precision requirements in radiation therapy. *Acta Oncologica*, 23(5):379–391, 1984.

[52] Marion Essers and Ben J. Mijnheer. In vivo dosimetry during external photon beam radiotherapy. *International Journal of Radiation Oncology Biology Physics*, 43(2):245–259, 1999.

[53] N. Weidner, R. J. Cote, S. Suster, and L. M. Weiss. *Modern Surgical Pathology*. Elsevier Health Sciences, 2nd edition, 2009.

[54] M. Joiner and A. van der Kogel. *Basic Clinical Radiobiology*. Hodder Education, 4th edition, 2009.

[55] Ben J. Mijnheer. State of the art of in vivo dosimetry. *Radiation Protection Dosimetry*, 131(1):117–122, 2008.

[56] U. Chica, G. Flórez, M. Anguiano, and A.M. Lallena. A simple analytical expression to calculate the backscatter factor for low energy x-ray beams. *Physica Medica*, 27(2):75–80, 2011.

[57] B. Sintay, T. Ramer, and D. Wiant. Su-e-t-185: Passing rates of 83 patient-specific imrt qa measurements with arccheck using various gamma criteria. *Medical Physics*, 38(6):3528–3529, 2011.

[58] O Circiumaru and T Zhu. Su-ff-t-283: In-vivo diode dosimetry for imrt fields. *Medical Physics*, 33(6):2111–2111, 2006.

[59] Huda Al-Mohammed, Fareed Mahyoub, and Belal Moftah. Comparative study on skin dose measurement using mosfet and tld for pediatric patients with acute lymphatic leukemia. *Medical Science Monitor*, 16(7):325–329, 2010.

[60] G. P. Beyer, G. G. Mann, J. A. Pursley, E. T. Espenhahn, C. Fraisse, D. J. Godfrey, M. Oldham, T. B. Carrea, N. Bolick, and C. W. Scarantino. An implantable mosfet dosimeter for the measurement of radiation dose in tissue during cancer therapy. *IEEE Sensors Journal*, 8(1):38–51, January 2008.

[61] Darren Southee, Gareth I. Hay, Peter S. A. Evans, and David J. Harrison. Development and characterisation of lithographically printed voltaic cells. In *Proceedings of 1st. Electronics System-Integration Technology Conference, Dresden, Germany, 5th-7th*, pages 1286–1291. IEEE, September 2006.

[62] Darren Southee, Gareth I. Hay, Peter S. A. Evans, and David J. Harrison. Lithographically printed voltaic cells - a feasibility study. *Circuit World*, 33(1):31–35, 2007.

[63] N. J. Dudney. Thin film micro-batteries. *The Electrochemical Society Interface*, 17(3):44–48, 2008.

[64] J. Greiner. *Microfabricated thin-film batteries: technology and potential applications*. PhD thesis, Massachusetts Institute of Technology, 2006.

[65] Jo Verhaevert, Frank Vanheel, and Patrick Van Torre. On the design of software and hardware for a wsn transmitter. In *Communications and Vehicular Technology, 16th Annual symposium of the IEEE Benelux Chapter, Proceedings*, pages 1–6, 2009.

[66] R. Eliakim, K. Yassin, I. Shlomi, A. Suissa, and G. M. Eisen. A novel diagnostic tool for detecting oesophageal pathology: the pillcam oe-

sophageal video capsule. *Alimentary pharmacology and Therapeutics*, 20(10):1083–1089, 2004.

[67] K. Motomura, Y. Komoike, Y. Hasegawa, T. Kasugai, H. Inaji, S. Noguchi, and H. Koyama. Intradermal radioisotope injection is superior to subdermal injection for the identification of the sentinel node in breast cancer patients. *Journal of Surgical Oncology*, 82(2):91–97, 2003.

[68] G. Gregoratos, M.D. Cheitlin, A. Conill, A. E. Epstein, C. Fellows, T. B. Ferguson Jr, R. A. Freedman, M. A. Hlatky, G. V. Naccarelli, and S. Saksena. Acc/aha guidelines for implantation of cardiac pacemakers and antiarrhythmia devices: a report of the american college of cardiology/american heart association task force on practice guidelines (committee on pacemaker implantation). *Journal of the American College of Cardiology*, 31(5):1175, 1998.

[69] Albert Paul Malvino. *Malvino Electronic Principles*. Glencoe / McGraw-Hill, 6th edition, 1999.

[70] Adel S. Sedra and Kenneth C. Smith. *Microelectronic Circuits*. Oxford University Press, 5th edition, 2004.

[71] Niels Bohr. On the constitution of atoms and molecules - part i. *Philosophical Magazine*, 26(151):1–25, 1913.

[72] Niels Bohr. On the constitution of atoms and molecules - part ii. *Philosophical Magazine*, 26(153):476–501, 1913.

[73] Niels Bohr. On the constitution of atoms and molecules - part iii. *Philosophical Magazine*, 26(155):857–75, 1913.

[74] Charles Kittel. *Introduction to Solid State Physics*. John Wiley & Sons, 8th edition, 2004.

[75] Muhammad H. Rashid. *Microelectronic Circuits: Analysis and Design*. PWS Publishing Company, 1st edition, 1998.

[76] H. Ahmed and P. J. Spreadbury. *Electronics for Engineers*. Cambridge University Press, 1st edition, 1973.

[77] Paul Horowitz and Winfield Hill. *The Art of Electronics*. Cambridge University Press, 2nd edition, 1989.

[78] Andrew Holmes-Siedle and Len Adams. *Handbook of Radiation Effects*. Oxford University Press, 2002.

[79] E. H. Nicollian and J. R. Brews. *MOS (metal oxide semiconductor) physics and technology*. Wiley, 1982.

[80] C. R. Wronski, S. Lee, M. Hicks, and Satyendra Kumar. Internal photoemission of holes and the mobility gap of hydrogenated amorphous silicon. *Physical Review Letters*, 63(13):1420–1423, 1989.

[81] R. H. Fowler and L. Nordheim. Electron emission in intense electric fields. *Proceedings of the Royal Society of London. Series A, Containing Papers of a Mathematical and Physical Character*, 119(781):173–181, May 1928.

[82] D. Kahng and S. M. Sze. A floating gate and its application to memory devices. *Bell System Technical Journal*, 46(6):1288–1295, May 1967.

[83] A. Thomsen and M. A. Brooke. A floating-gate mosfet with tunneling injector fabricated using a standard double-polysilicon cmos process. *Electron Device Letters, IEEE*, 12(3):111–113, March 1991.

[84] C. Claeys and E. Simoen. *Radiation Effects in Advanced Semiconductor Materials and Devices*. Springer, 1st edition, 2002.

[85] J. R. Srour, C. J. Marshall, and P. W. Marshall. Review of displacement damage effects in silicon devices. *IEEE Transactions on Nuclear Science*, 50(3):653–670, 2003.

[86] W. Bludau, A. Onton, and W. Heinke. Temperature dependence of the band gap of silicon. *Journal of Applied Physics*, 45(4):1846–1848, 1974.

[87] T.H. DiStefano and D.E. Eastman. The band edge of amorphous sio2 by photoinjection and photoconductivity measurements. *Solid State Communications*, 9(24):2259–2261, 1971.

[88] T. R. Oldham, F. B. McLean, H. E. Boesch Jr, and J. M. McGarrity. An overview of radiation-induced interface traps in mos structures. *Semiconductor Science and Technology*, 4(12):986–999, 1989.

[89] Albert Einstein. Ist die trägheit eines körpers von seinem energieinhalt abhängig? *Annalen der Physik*, 323(13):639–641, 1905.

[90] V. Privitera, S. Coffa, F. Priolo, and E. Rimini. Migration and interaction of point defects at room temperature in crystalline silicon. *La Rivista del Nuovo Cimento*, 21(8):1–52, August 1998.

[91] N. G. Tarr, G. F. Mackay, K. Shortt, and I. Thomson. A floating gate mosfet dosimeter requiring no external bias supply. *IEEE Transactions on Nuclear Science*, 45(3):1470–1474, June 1998.

[92] John David Jackson. *Classical electrodynamics*. John Wiley & Sons, 3rd edition, 1998.

[93] W. N. Cottingham and D. A. Greenwood. *Electricity and Magnetism*. Cambridge University Press, 1st edition, 1991.

[94] Demetrius T. Paris and F. Kenneth Hurd. *Basic Electromagnetic Theory*. McGraw Hill, 1st edition, 1969.

[95] Daniel Fleisch. *A Student's Guide to Maxwell's Equations*. Cambridge University Press, 1st edition, 2008.

[96] James Clerk Maxwell. XXV. On physical lines of force. *Philosophical Magazine*, 21(139):161–175, 1861.

[97] James Clerk Maxwell. XLIV. On physical lines of force. *Philosophical Magazine*, 21(140):281–291, 1861.

[98] James Clerk Maxwell. LI. On physical lines of force. *Philosophical Magazine*, 21(141):338–348, 1861.

[99] James Clerk Maxwell. III. On physical lines of force. *Philosophical Magazine*, 23(151):12–24, 1862.

[100] James Clerk Maxwell. XIV. On physical lines of force. *Philosophical Magazine*, 23(152):85–95, 1862.

[101] James Clerk Maxwell. A dynamical theory of the electromagnetic field. *Philosophical Transactions of the Royal Society of London*, 155:459–512, 1865.

[102] Glenn S. Smith. Radiation efficiency of electrically small multiturn loop antennas. *IEEE Transactions on Antennas and Propagation*, 20(5):656 – 657, 1972.

[103] Kyohei Fujimoto and J. R. James. *Mobile Antenna Systems Handbook*. Artech House Publishers, 2nd edition, 2001.

[104] John Henry Poynting. On the transfer of energy in the electromagnetic field. *Philosophical Transactions of the Royal Society of London*, 175:343–361, 1884.

[105] Bhag Singh Guru and Hüseyin R. Hiziroglu. *Electromagnetic Field Theory Fundamentals*. Cambridge University Press, 2nd edition, 2009.

[106] W. L. Stutzman and G. A. Thiele. *Antenna Theory and Design*. Wiley, 3rd edition, 2012.

[107] C. P. Yue and S. S. Wong. Design strategy of on-chip inductors for highly integrated rf systems. In *Design Automation Conference, 1999. Proceedings. 36th*, pages 982–987, 1999.

[108] R. Edgecock, J. Matheson, M. Weber, Giulio E. Villani, R. Bose, A. Khan, D. R. Smith, I. Adil-Smith, and A. Gabrielli. Evaluation of commercial programmable floating gate devices as radiation dosimeters. *Journal of Instrumentation*, 4(2):1–10, February 2009.

[109] W. P. Levin, H. Kooy, J. S. Loeffler, and T. F. DeLaney. Proton beam therapy. *British Journal of Cancer*, 93(8):849–854, 2005.

[110] R. Pazdur, L. R. Coia, W. J. Hoskins, and L. D. Wagman. *Cancer management: a multidisciplinary approach*. P. R. R. Inc., 8th edition, 2004.

[111] M. Stanley Livingston and H. A. Bethe. Nuclear physics c. nuclear dynamics, experimental. *Reviews of Modern Physics*, 9(3):245–390, 1937.

[112] Peter Alexander. Radiosensitivity of cells. *IAEA Bulletin*, 2(3):21–24, 1960.

[113] J. Bergonié and L. Tribondeau. Interpretation of some results of radiotherapy and an attempt at determining a logical technique of treatment / de quelques resultats de la radiotherapie et essai de fixation d'une technique rationnelle. *Comptes-Rendus des Séances de l'Académie des Sciences*, 143:983–985, 1906.

[114] M. B. Hollander. Grenz rays. *Journal of Investigative Dermatology*, 21(1):15–26, 1953.

[115] G. Cellere, P. Pellati, A. Chimenton, J. Wyss, A. Modelli, L. Larcher, and A. Paccagnella. Radiation effects on floating-gate memory cells. *IEEE Transactions on Nuclear Science*, 48(6):2222–2228, December 2001.

[116] M. N. Martin, D. R. Roth, A. Garrison-Darrin, P. J. McNulty, and A. G. Andreou. FGMOS dosimetry: design and implementation. *IEEE Transactions on Nuclear Science*, 48(6):2050–2055, December 2001.

[117] A. Holmes-Siedle, L. Adams, and G. Ensell. Mos dosimeters - improvement of responsivity. In *First European Conference on Radiation and its Effects on Devices and Systems*, pages 65–69, September 1991.

[118] A. Kelleher, M. O'Sullivan, J. Ryan, B. O'Neill, and W. Lane. Development of the radiation sensitivity of pmos dosimeters. *IEEE Transactions on Nuclear Science*, 39(3):342–346, 1992.

[119] G. Sarrabayrouse. Mos radiation dosimeter: sensitivity and stability. In *First European Conference on Radiation and its Effects on Devices and Systems*, pages 57–59, 1991.

[120] Giulio Villani, Rajiv Bose, and Alessandro Gabrielli. Evaluation of on-chip micro antennas for in vivo dosimetry application. *Radiation Measurements*, 46(12):1963–1966, 2011.

[121] C. W. Scarantino Scarantino, B. Prestidge, M. Anscher, C. Ferree, R. Black, and G. P. Beyer. True in-vivo dosimetry in breast and prostate cancer patients: Variance between predicted and measured dose. *International Journal of Radiation Oncology Biology Physics*, 66(3):104–105, November 2006.

[122] D. Halperin, T. Kohno, T. S. Heydt-Benjamin, K. Fu, and W. H. Maisel. Security and privacy for implantable medical devices. *IEEE Pervasive Computing*, 7(1):30–39, 2008.

[123] Peter Bouxsein Kathi E. Hanna, Frederick J. Manning and Andrew Pope. *Innovation and Invention in Medical Devices: Workshop Summary*. The National Academies Press, 2001.

[124] T. F. Saad, D. M. Hentschel, B. Koplan, H. Wasse, A. Asif, D. V. Patel, L. Salman, R. Carrillo, and J. Hoggard. Cardiovascular implantable electronic device leads in ckd and esrd patients: Review and recommendations for practice. In *Seminars in Dialysis*. Wiley Online Library, 2012.

[125] A. B. Rosenfeld, D. Cutajar, M. L. F. Lerch, G. Takacs, I. M. Cornelius, M. Yudelev, and M. Zaider. Miniature semiconductor detectors for in vivo dosimetry. *Radiation Protection Dosimetry*, 120(1-4):48–55, September 2006.

[126] C. W. Scarantino, D. M. Ruslander, C. J. Rini, G. G. Mann, H. T. Nagle, and R. D. Black. An implantable radiation dosimeter for use in external beam radiation therapy. *Medical Physics*, 31(9):2658–2671, September 2004.

[127] Using mobile phones in nhs hospitals. Technical report, Department of Health, January 2009.

[128] Mics band plan. Technical Report 95, FCC Rules and Regulations, January 2003.

[129] M. R. Yuce, S. W. P. Ng, N. L. Myo, C. K. Lee, J. Y. Khan, and Wentai Liu. A mics band wireless body sensor network. In *Wireless Communications and Networking Conference, 2007.WCNC 2007. IEEE*, pages 2473 –2478, March 2007.

[130] Jong-Wan Kim, Hidekuni Takao, Kazuaki Sawada, and Makoto Ishida. Integrated inductors for rf transmitters in cmos/mems smart microsensor systems. *Sensors*, 7(8):1387–1398, 2007.

[131] Peter D. Bradley. An ultra low power, high performance medical implant communication system (mics) transceiver for implantable devices. In *Biomedical Circuits and Systems Conference, 2006. BioCAS 2006. IEEE*, pages 158–161, 2006.

[132] A. Dollfus. Compte rendus acad. *Sciences Paris*, 227:331–333, 1948.

[133] A. Shamim, M. Arsalan, L. Roy, M. Shams, and G. Tarr. Wireless dosimeter: System-on-chip versus system-in-package for biomedical and space applications. *IEEE Transactions on Circuits and Systems II: Express Briefs*, 55(7):643–647, 2008.